UNIVERSITY OF
BIRMINGHAM

University of Birmingham Research Archive

e-theses repository

This unpublished thesis/dissertation is copyright of the author and/or third parties. The intellectual property rights of the author or third parties in respect of this work are as defined by The Copyright Designs and Patents Act 1988 or as modified by any successor legislation.

Any use made of information contained in this thesis/dissertation must be in accordance with that legislation and must be properly acknowledged. Further distribution or reproduction in any format is prohibited without the permission of the copyright holder.

Pages 138 to end (Chapter 4.2 to end)

Effects of Oxide film, Fe-rich phase, Porosity and their Interactions on Tensile Properties of Cast Al-Si-Mg Alloys

Kittiphan Bangyikhan

A thesis submitted to the Faculty of Engineering of
The University of Birmingham
for the degree of
Doctor of Philosophy

School of Metallurgy and Materials
Faculty of Engineering
University of Birmingham
Birmingham B15 2TT
United Kingdom
June 2005

4.2 Interactions between oxide film and shrinkage porosity in a low and high Fe content cast Al-Si-Mg alloys.

The results of this experiment were used to investigate the effect on tensile properties produced by oxide films and shrinkage porosity, and demonstrate the interrelationships between these microstructural defects in cast Al-Si-Mg alloys. The alloy used in the experiment was varied to obtain 2 types, a low Fe content (0.1 wt% Fe) and a high Fe content (1.1 wt% Fe). However the Mg content was changed during the preparation of the high Fe content alloys, and the experiment, therefore, became that of two groups of castings (Al-7Si-0.3Mg-0.1Fe alloy and Al-7Si-0.2Mg-1.1Fe alloy) and their results are as follows;

4.2.1 Interactions between oxide film and shrinkage porosity in cast Al-7Si-0.3Mg-0.1Fe alloy

4.2.1.1 Tensile properties

Tables 4.13 and 4.14 show the ultimate tensile strength (UTS) and elongation values for all test bars obtained with the 4 combinations of defects in the castings. As expected, the high oxide film and high shrinkage castings had the worst UTS and elongation, (with a mean UTS of 285 MPa and a mean elongation of 2.82 %), while the low oxide film and high shrinkage castings (surprisingly) had the best UTS and elongation, (with a mean UTS of 298 MPa and a mean elongation of 5.06 %). The results also showed that increasing the amount of defects in the castings influenced the tensile properties by decreasing the UTS and elongation. For example, the increase in oxide film content in the high shrinkage castings resulted in a reduction in a mean UTS and mean elongation by 13 MPa and 2.2 % respectively. Increasing shrinkage porosity at this experimental level appeared to have only a slight effect on the tensile properties, for example, in the low oxide film castings the increase in shrinkage resulted in a reduction in the UTS and elongation by only about 2 MPa and 0.4 % respectively.

Table 4.13 Ultimate Tensile Strength (UTS) values of cast Al-7Si-0.3Mg-0.1Fe alloy for 4 experimental combinations.

Test bar No.	Ultimate Tensile Strength (MPa)			
	Low oxide film and low shrinkage	Low oxide film and high shrinkage	High oxide film and low shrinkage	High oxide film and high shrinkage
1	295.11	295.91	295.64	292.00
2	297.20	283.47	281.75	301.06
3	300.68	304.62	250.67	244.90
4	298.59	298.22	294.74	279.03
5	293.72	292.53	287.70	288.45
6	295.81	307.46	287.52	276.18
7	286.06	289.33	299.07	285.78
8	299.99	306.04	290.59	272.63
9	295.11	301.77	295.96	287.20
10	293.02	302.66	281.62	293.24
11	298.07	299.82	292.87	284.36
12	302.20	297.51	291.06	261.25
13	305.33	288.27	285.61	292.13
14	295.10	293.24	292.87	292.49
15	290.56	298.93	295.05	297.85
16	305.05	302.66	289.24	286.41
17	296.85	301.95	295.05	285.33
18	292.42	293.42	286.34	300.71
19	301.23	300.35	287.79	285.16
20	301.93	291.13	296.50	292.57
21	290.84	301.16	296.86	283.92
22	300.08	299.72	304.85	277.42
23	272.51	298.29	291.60	287.52
24	301.74	305.03	297.95	283.19
25	289.53	302.50	295.96	278.86
26	293.43	297.85	287.43	304.95
27		302.08	292.15	271.66
28		275.32	297.05	
29			287.97	
Mean UTS (MPa)	295.85	297.54	290.67	284.68

Table 4.14 Elongation values cast Al-7Si-0.3Mg-0.1Fe alloy for 4 experimental combinations.

Test bar No.	Elongation (%)			
	Low oxide film and low shrinkage	Low oxide film and high shrinkage	High oxide film and low shrinkage	High oxide film and high shrinkage
1	3.59	2.89	5.20	3.00
2	6.05	1.92	2.13	3.78
3	6.23	7.39	1.96	1.08
4	4.03	6.50	5.41	2.34
5	3.42	3.01	4.26	3.09
6	4.57	7.00	3.76	1.40
7	2.77	3.11	4.39	2.57
8	7.05	5.83	4.38	2.75
9	3.75	5.93	3.99	3.03
10	3.99	6.31	2.74	4.19
11	4.58	5.46	3.19	2.52
12	4.42	5.08	5.32	1.12
13	6.01	3.77	3.98	4.31
14	4.41	4.45	3.98	4.45
15	4.74	4.68	4.60	2.75
16	6.99	7.15	3.10	3.05
17	4.98	6.63	4.09	2.31
18	5.58	5.04	3.33	3.51
19	5.48	5.36	3.47	3.15
20	4.58	5.05	4.13	2.53
21	4.15	5.44	4.51	2.05
22	5.86	6.04	4.96	1.81
23	2.04	6.29	4.35	3.61
24	5.16	5.79	4.76	3.71
25	4.56	6.47	3.77	2.03
26	4.03	4.38	3.91	4.54
27		4.33	4.88	1.34
28		1.76	3.60	
29			3.41	
Mean Elongation (MPa)	4.73	5.06	3.98	2.82

4.2.1.2 Pareto diagram of tensile properties

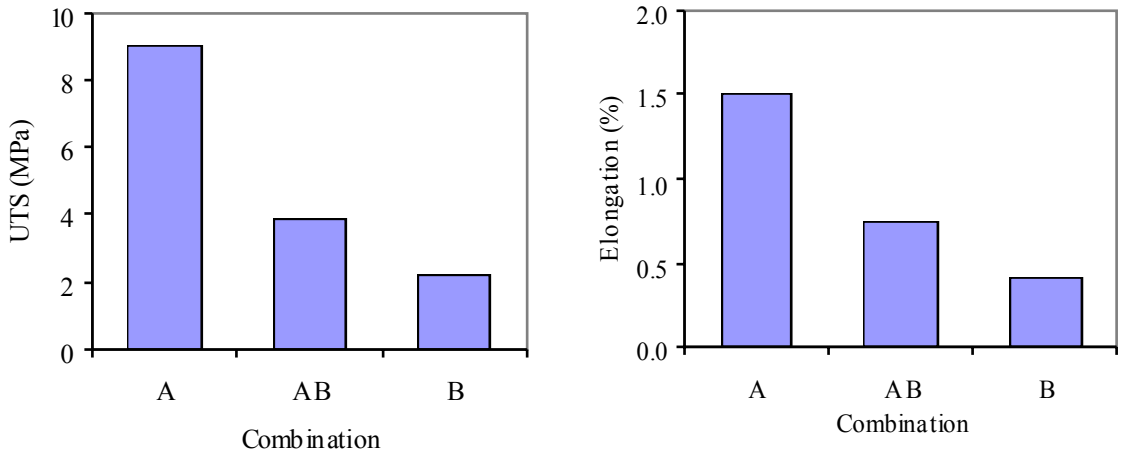
The effects of oxide films and shrinkage porosity on the tensile properties were estimated using Yates' algorithm. Tables 4.15 and 4.16 show the calculations of the relative effects on the UTS and the elongation produced by the two defects and their interactions. Figures 4.64a and 4.64b show the Pareto diagrams obtained from the results in Tables 4.15 and 4.16 respectively. These show that there was an effect produced by the oxide film defect (column A) on UTS of about 9 MPa and on elongation of about 1.5%. There was no significant effect of shrinkage porosity on UTS (column B) and therefore no evidence for an interaction between oxide films and shrinkage porosity (column AB) in this experiment. This suggested that the mould rotation method that was applied to minimize solidification shrinkage in the low shrinkage castings produced little effect on shrinkage porosity, when compared to the high shrinkage castings.

Table 4.15 The effect of oxide film, shrinkage and their interactions to ultimate tensile strength (UTS) using Yate's algorithm.

	UTS (MPa)	1	2	estimate of effect
(1)	295.85	586.52	1168.74	584.37
effect of oxide film: A	290.67	582.22	-18.04	-9.02
effect of shrinkage: B	297.54	-5.18	-4.30	-2.15
AB	284.68	-12.86	-7.68	-3.84

Table 4.16 The effect of oxide film, shrinkage and their interactions to Elongation using Yate's algorithm.

	Elongation (%)	1	2	estimate of effect
(1)	4.73	8.71	16.59	8.30
effect of oxide film: A	3.98	7.88	-2.99	-1.50
effect of shrinkage: B	5.06	-0.75	-0.83	-0.42
AB	2.82	-2.24	-1.49	-0.75



(a) (b)

Figure 4.64 Pareto diagrams showing the effects of the two defects and their inter-relationship on (a) the UTS (b) the percent elongation value of the castings (A = effect of oxide film, B = effect of Shrinkage)

4.2.1.3 Examination of fracture surfaces

The fracture surfaces of all test bars obtained from each experimental combination were examined by visual inspection. This showed that no large double oxide film defect was observed. The low UTS test bars were further examined by digital camera and scanning electron microscopy. The presence of double oxide film defects was observed but they were smaller in size compared to that found in the previous experiment (i.e. Figures 4.6, 4.10, 4.13 and 4.16). Figure 4.65 shows macrographs of the fracture surfaces of test bar 3 from the high oxide film and low shrinkage castings, (UTS of 251 MPa). Figures 4.66a to 4.66d show higher magnification SEM images obtained from these fracture surfaces. The associated EDX analysis results have been shown in Figures 4.67a to 4.67d. These showed that the test bar contained double oxide film defects of about 1 mm in length, which were symmetrical on both sides of the fracture surfaces, and this defect might have resulted in a reduction in tensile properties. Figure 4.68 shows the fracture surfaces of another test bar with low UTS (of about 245 MPa) obtained from test bar 3 of the high

oxide film and high shrinkage castings. As expected, the decrease in the tensile properties was caused by the presence of double oxide film defects since the high magnification SEM images and their EDX analysis results, shown in Figures 4.69a to 4.69d and Figures 4.70a to 4.70d respectively, showed oxide films on both sides of fracture surfaces. The SEM images of oxide films and the small oxygen peaks from the EDX analysis results suggested that the oxide films observed in this experiment were young oxide films, which might newly form during mould filling.

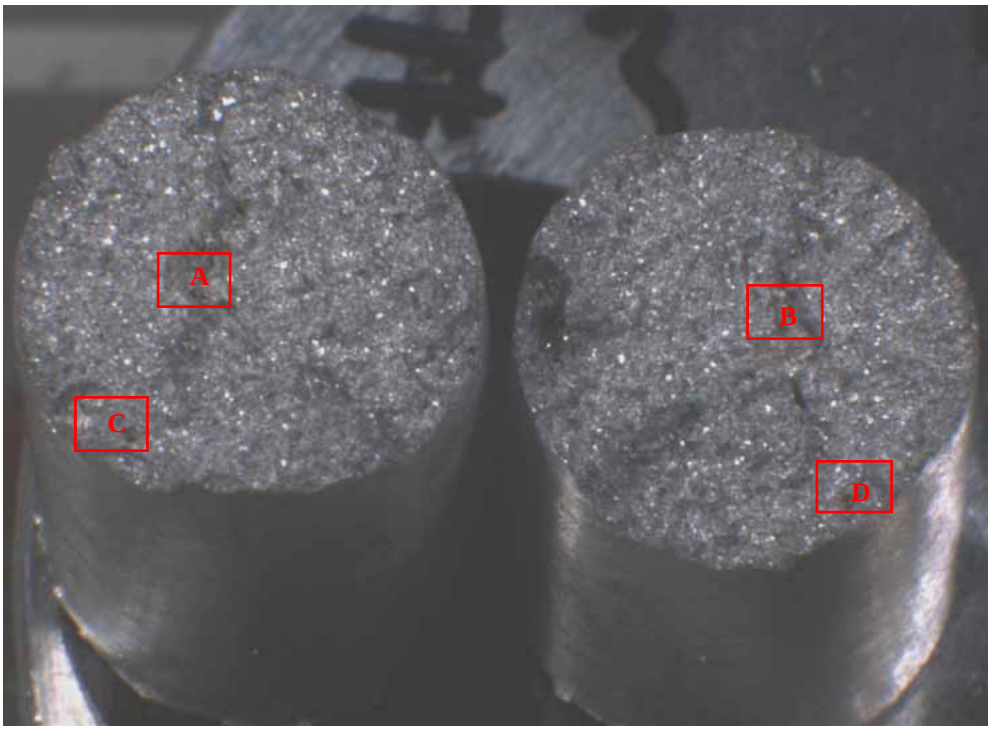
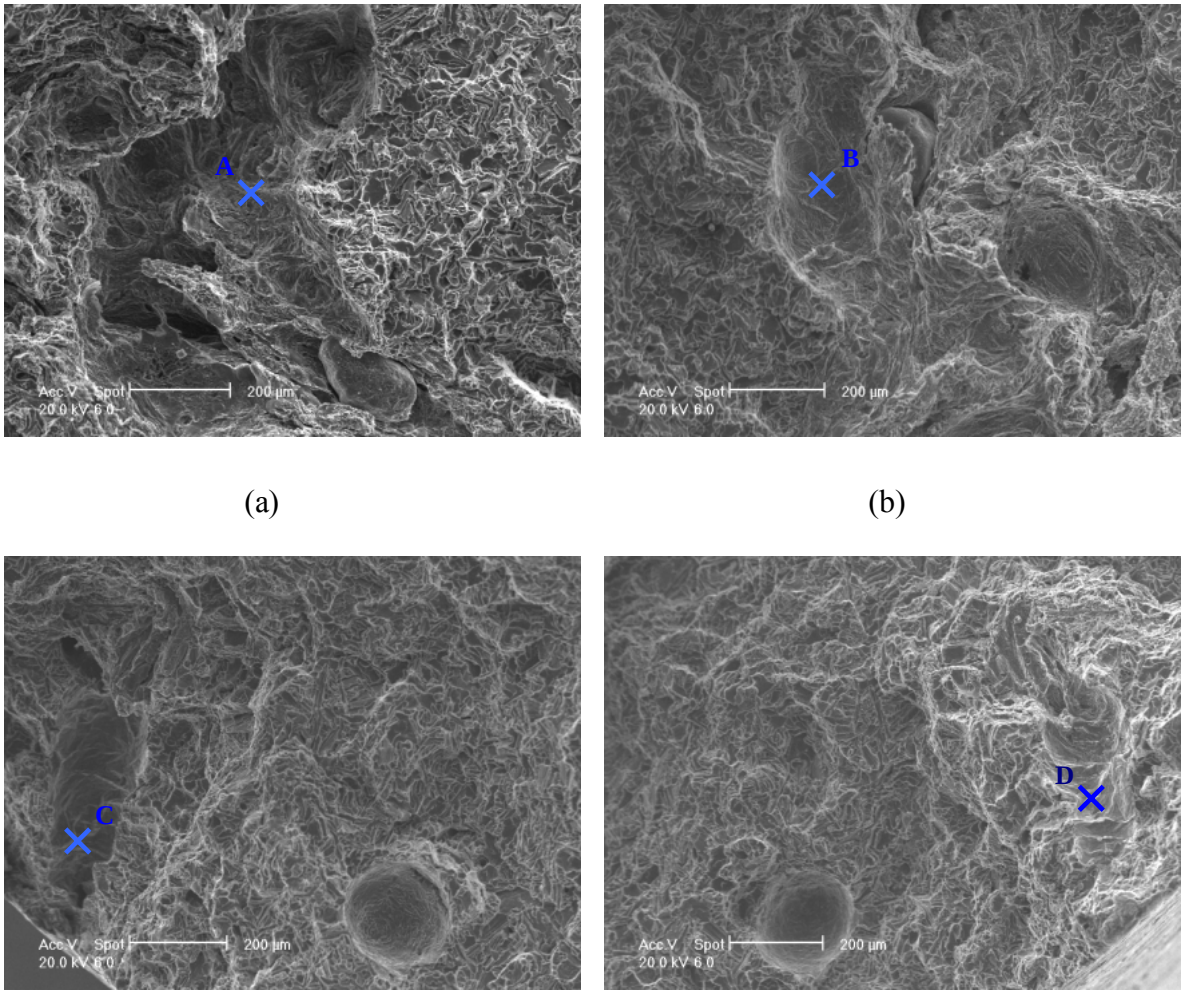


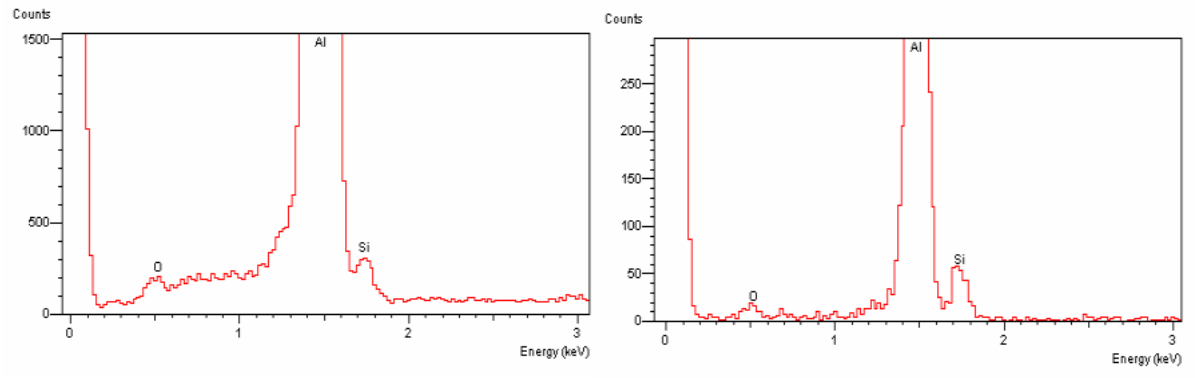
Figure 4.65 Photograph showing the fracture surfaces of test bar 3 obtained from the high oxide film and low shrinkage casting.



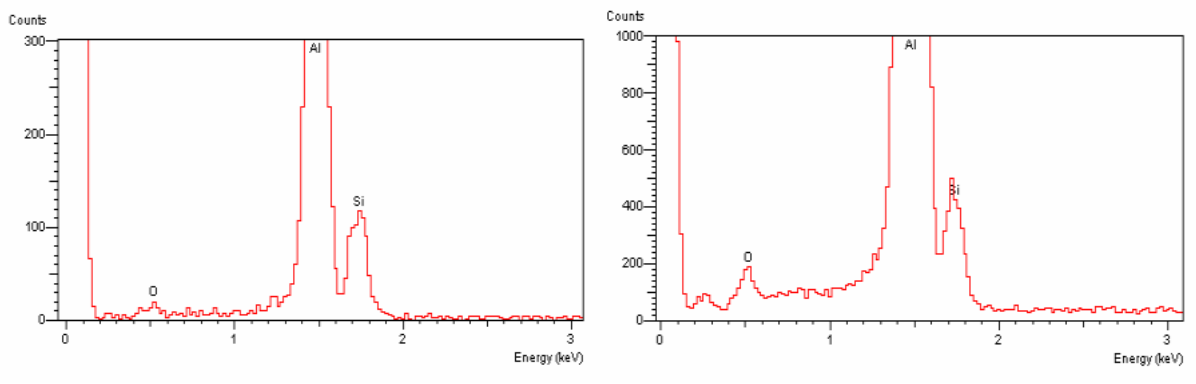
(a) (b)

(c) (d)

Figure 4.66 The scanning electron micrographs showing the close-up images of oxide films on the fracture surfaces from areas A to D in Figure 4.65.



(a) (b)



(c) (d)

Figure 4.67 The EDX analysis results obtained from points A to d in figures 4.66a to 4.66d.

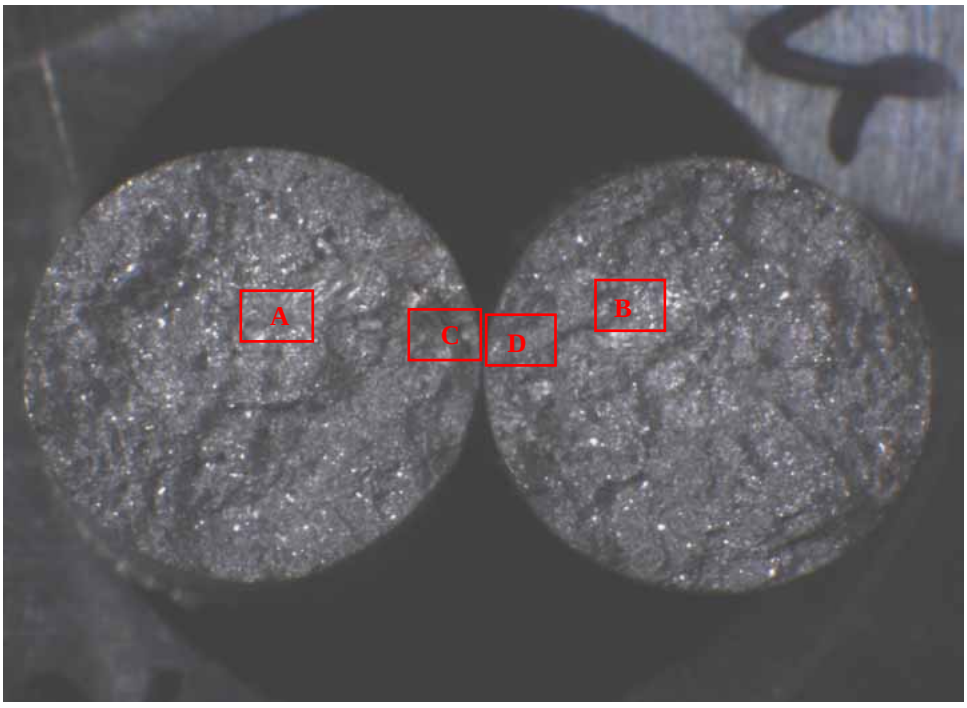
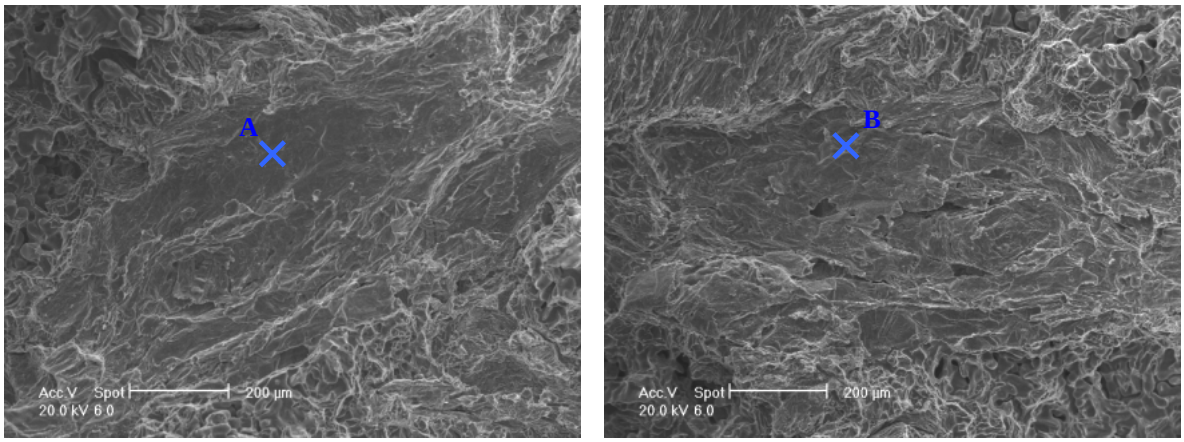
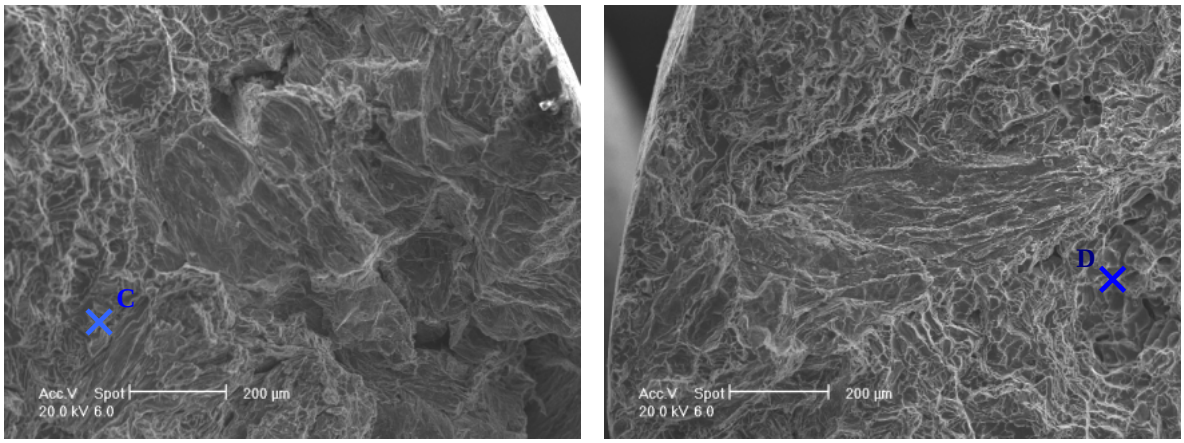


Figure 4.68 Photograph showing the fracture surfaces of test bar 3 obtained from the high oxide film and high shrinkage casting.

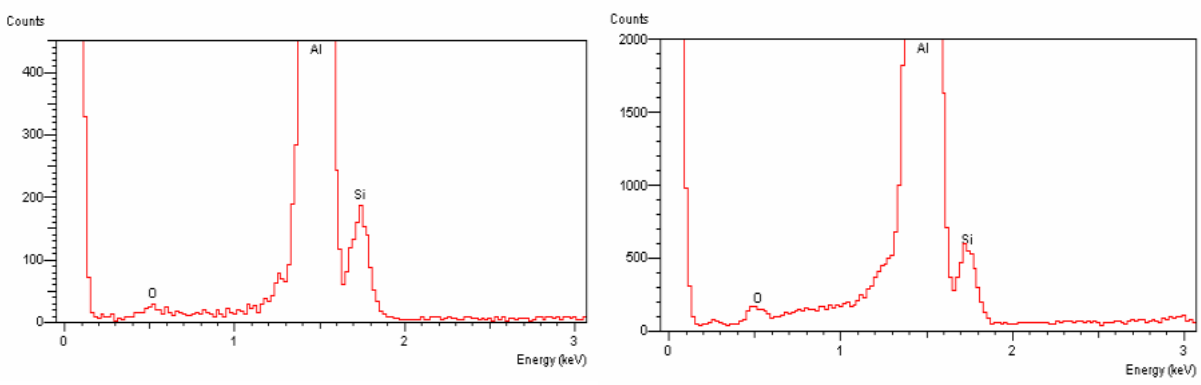


(a) (b)

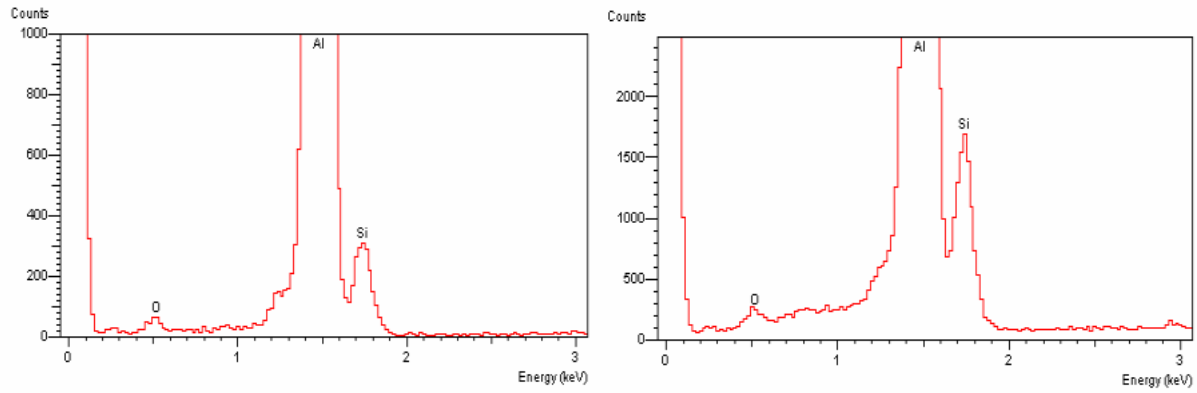


(c) (d)

Figure 4.69 The scanning electron micrographs showing the close-up images of oxide films on the fracture surfaces from areas A to D in Figure 4.68.



(a) (b)



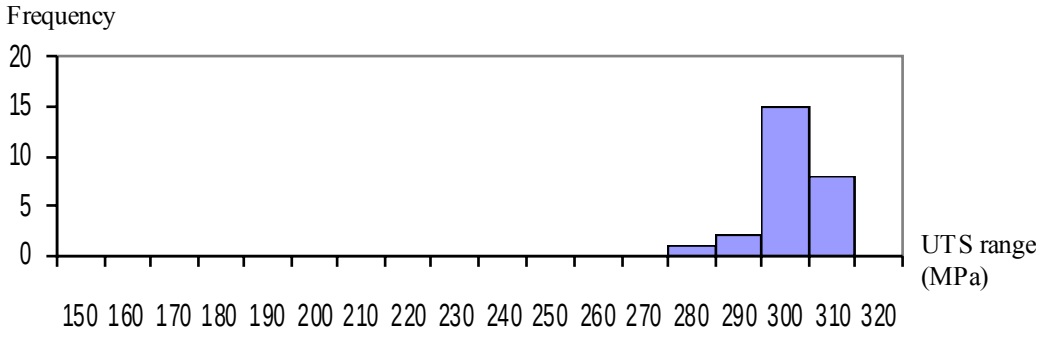
(c) (d)

Figure 4.70 The EDX analysis results obtained from points A to D in figures 4.69a and 4.69d.

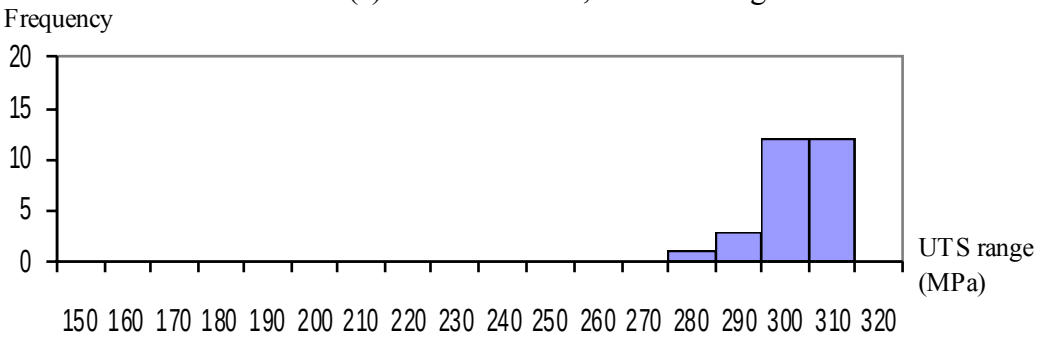
4.2.1.4 Weibull analysis

Figures 4.71 and 4.72 respectively show the distribution histograms of the UTS and elongation data obtained from the 4 combinations of castings. The distribution of tensile properties in the experiment was characterized by a non-normal distribution. Therefore, the Weibull distribution model was used for describing the tensile property data.

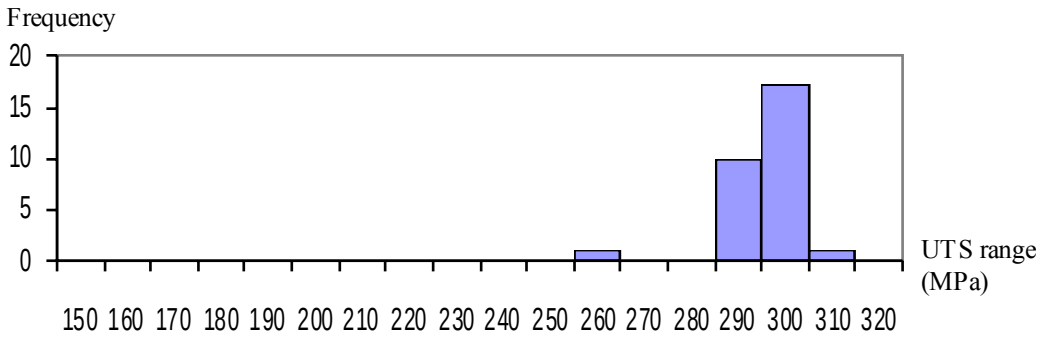
Figures 4.73a and 4.73b show graphs of probability of fracture versus UTS, and Weibull plots obtained from the UTS data respectively. The graphs of probability of fracture versus elongation and Weibull plots obtained from the elongation data have been shown in Figures 4.74a and 4.74b respectively. The Weibull modulus and the R values obtained from the UTS and elongation data, for all experimental combinations, have been shown in Table 4.17. The Weibull plots showed that the low oxide film and low shrinkage castings had the highest UTS and elongation Weibull modulus of about 52 and 4.5 respectively. The results again demonstrated that oxide film defects produced a scatter of tensile properties by decreasing the Weibull modulus, particularly the UTS Weibull modulus. For example, in the high shrinkage castings the increase in oxide film content resulted in a reduction in the UTS Weibull modulus of about 23. The shrinkage porosity for this experimental level appeared to produce no significant effect on the distribution of tensile properties, for example, in the low oxide film castings, increasing shrinkage porosity resulted in a decrease in UTS Weibull modulus by only 2.



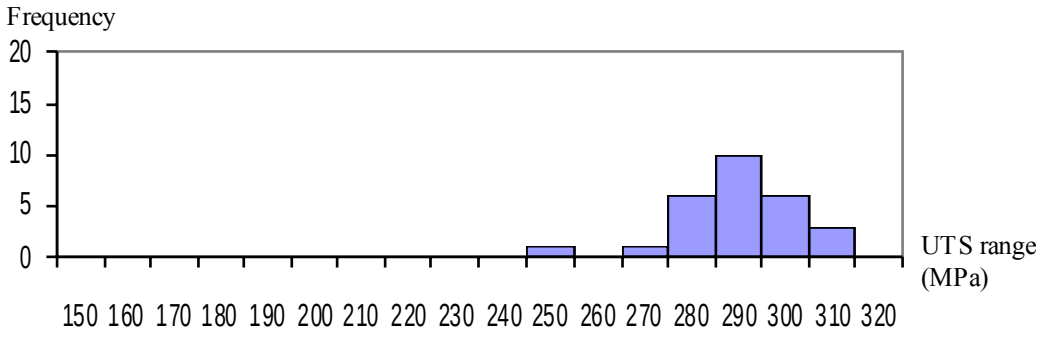
(a) low oxide film, low shrinkage



(b) low oxide film, high shrinkage

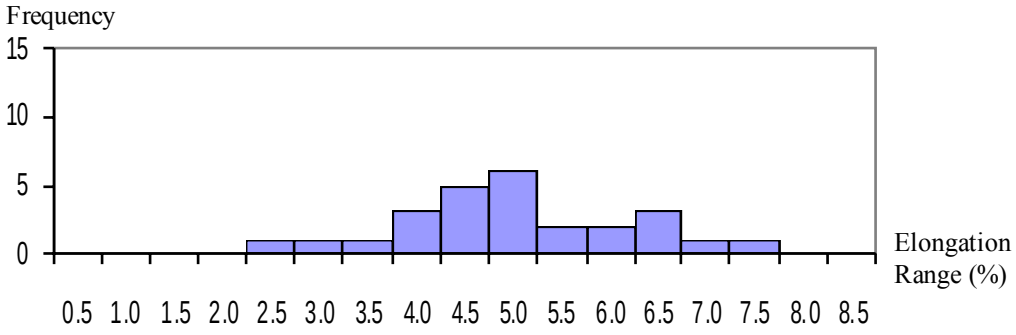


(c) high oxide film, low shrinkage

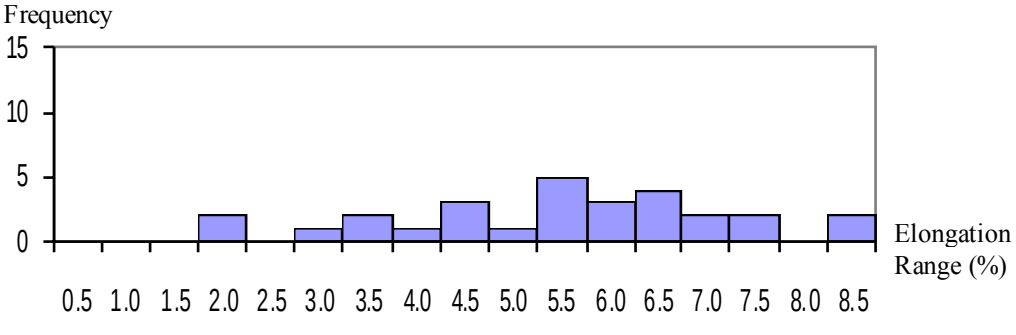


(d) high oxide film, high shrinkage

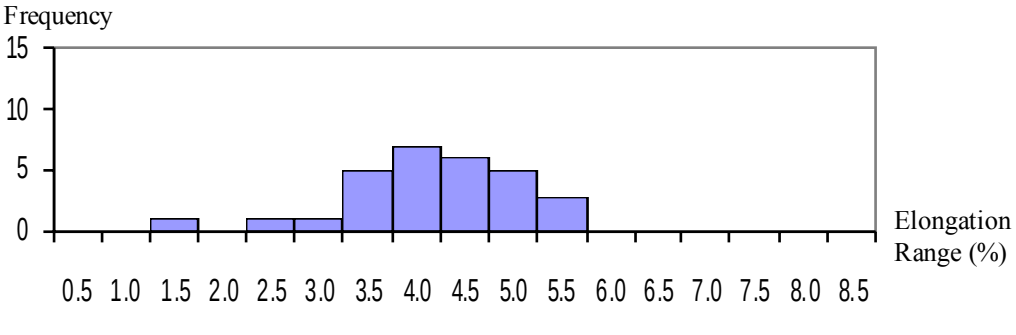
Figure 4.71 Frequency plots of ultimate tensile strength (UTS).



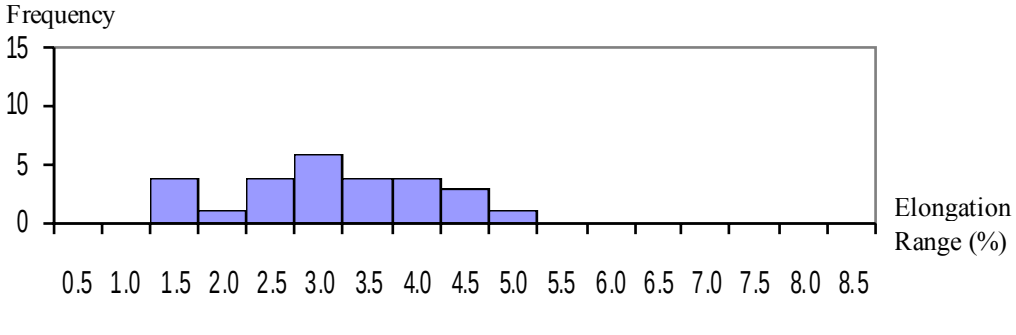
(a) low oxide film, low shrinkage



(b) low oxide film, high shrinkage

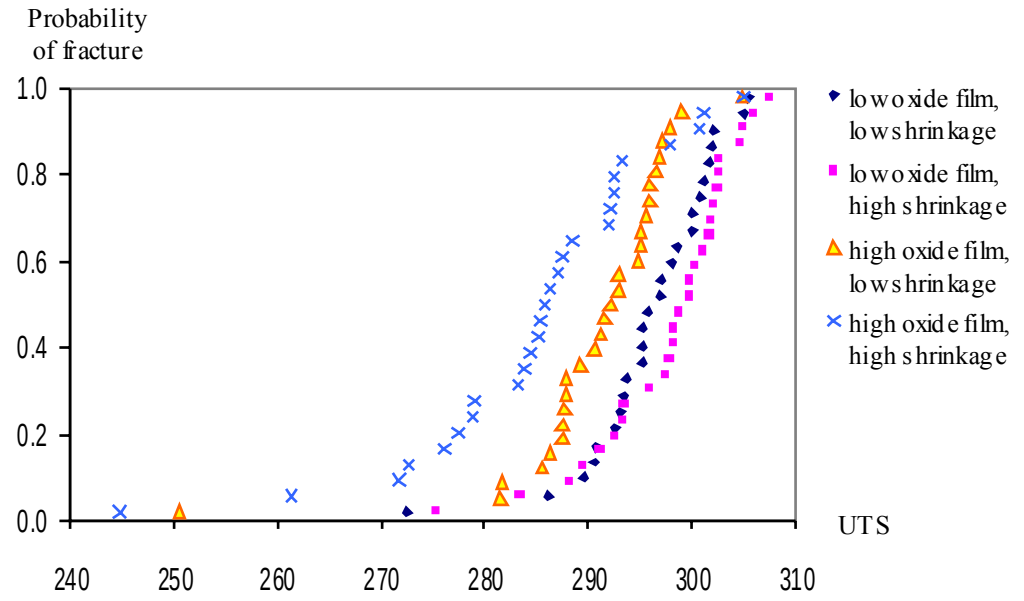


(c) high oxide film, low shrinkage

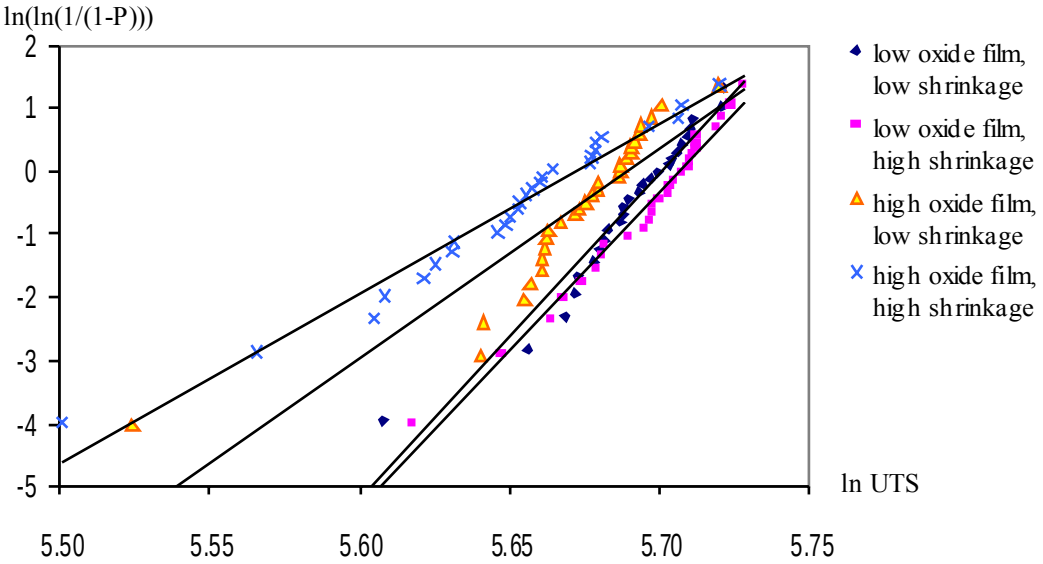


(d) high oxide film, high shrinkage

Figure 4.72 Frequency plots of percent elongation.

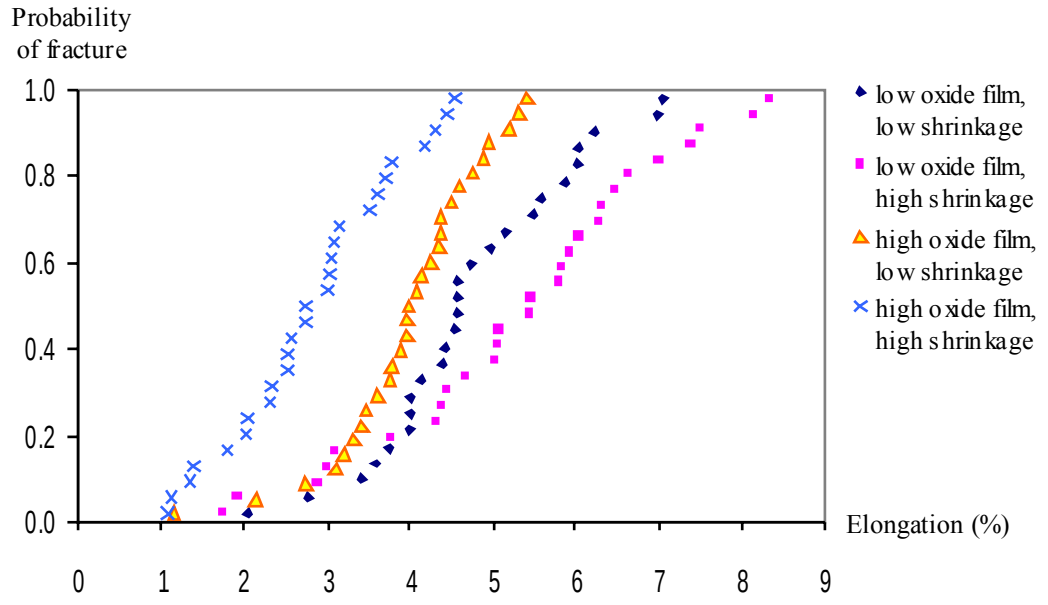


(a)

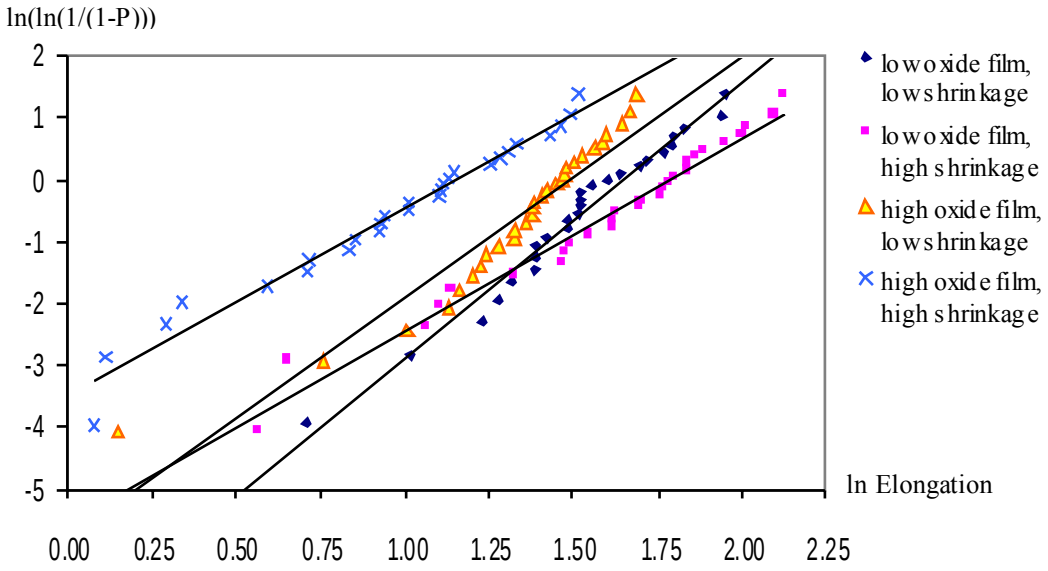


(b)

Figure 4.73 The graphs showing (a) cumulative plots (b) Weibull plots of ultimate tensile strength (UTS) data.



(a)



(b)

Figure 4.74 The graphs showing (a) cumulative plots (b) Weibull plots of percent elongation data.

Table 4.17 Weibull modulus values obtained from the Weibull plots of ultimate tensile strength (UTS) (Figure 4.73b) and percent elongation (Figure 4.74b).

Combination	UTS Weibull modulus	R	Elongation Weibull modulus	R
low oxide film, low shrinkage	52.0	0.97	4.46	0.99
low oxide film, high shrinkage	50.5	0.99	3.12	0.99
high oxide film, low shrinkage	33.4	0.90	3.89	0.95
high oxide film, high shrinkage	27.1	0.98	3.04	0.98

The Weibull plots and the R values showed that the tensile properties of castings in this experiment had a Weibullian distribution as the fitted line matched the data well (the closer to 1 for the R value, the better fit of the line). However the presence of oxide films tended to change the distribution manner by reducing the R value, for example, in the low shrinkage casting the R value decreased from 0.97 to 0.90. It can be seen in the Weibull plot (Figure 4.73b) that the set of UTS data obtained from the high oxide film and low shrinkage castings did not plot as a good fit to the data because of the lowest UTS data point. SEM examination (see Figure 4.66) showed that the failure of this test bar was caused by double oxide film defects. This suggested that the difference in failure mechanism influenced the distribution of tensile properties so as not to be plotted as a linear line by a single-defect Weibull distribution. As in the previous experiment, the Weibull distribution can be divided with two trend-lines for the different failure mechanisms (as shown in Figures 4.33a and 4.33b). Figure 4.75 shows the Weibull distribution of the UTS data obtained from the high oxide film and low shrinkage castings plotted as two separated groups. It can be seen that a better linear fit was obtained (with R values of 0.98) when the lowest UTS test bar, which failed by double oxide film defects, was not considered. The Weibull plot also showed that the new Weibull modulus obtained was at the same level of the low oxide film casting (of about 52). The presence of double oxide film defects in the casting therefore affects the reliability and the distribution of tensile properties.

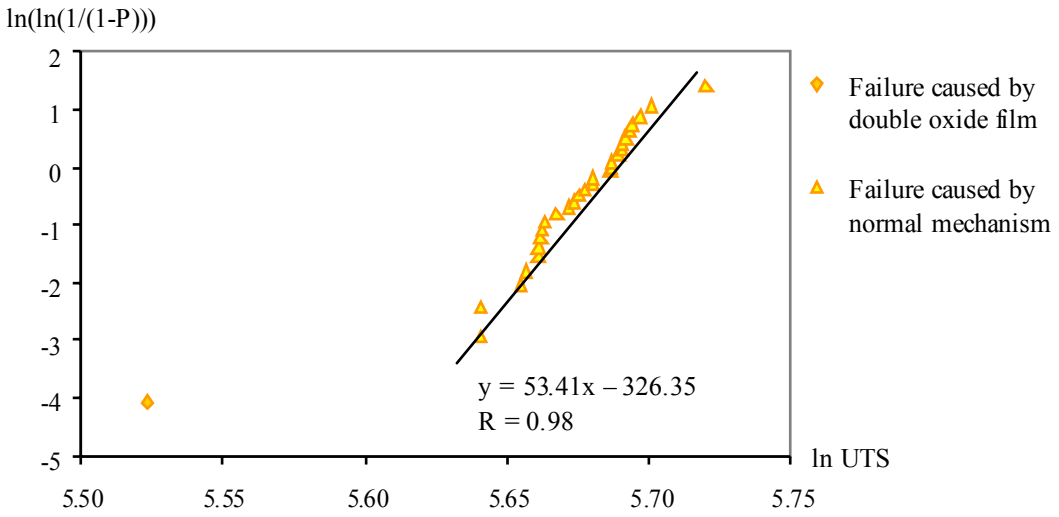


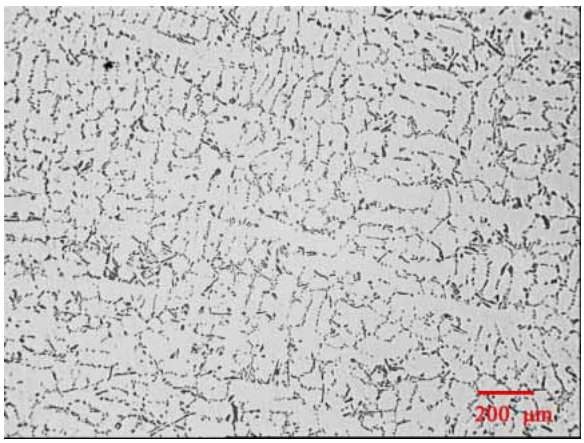
Figure 4.75 The graph showing the new Weibull plots of the UTS data of the high oxide film and low shrinkage castings considering two different failure mechanisms

4.2.1.5 Casting microstructures

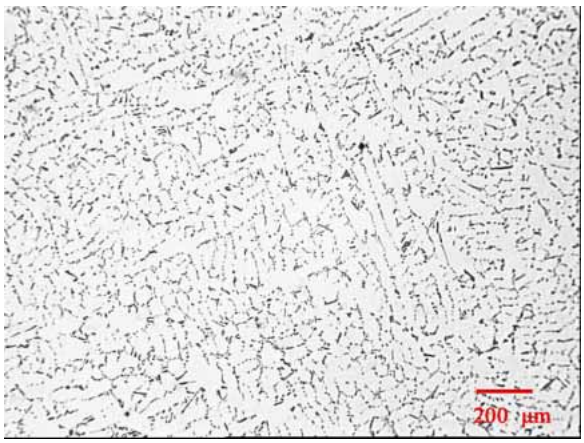
Figures 4.76a to 4.76d show microstructures of the 4 types of castings obtained from the cross sections of heat-treated test bars. The images showed that the main defect observed was microporosity, which was located in the interdendritic region as was observed in the low hydrogen content castings (0.1 ml/100g metal) of the previous experiment (see Figures 4.43a to 4.43d). Figure 4.77 shows higher magnification image of microporosity obtained from the high oxide film and high shrinkage castings. The irregular shape of the pores suggested that it was shrinkage porosity. This showed that there were some shrinkage porosity introduced in this experiment. However, the shrinkage porosity formed in the high shrinkage castings was not as much as expected.

The micrographs also showed an interaction between shrinkage porosity and oxide films since the shrinkage porosity contained oxide film in the interior surface. Figure 4.78 shows an SEM image of shrinkage porosity obtained from the high oxide film and high shrinkage

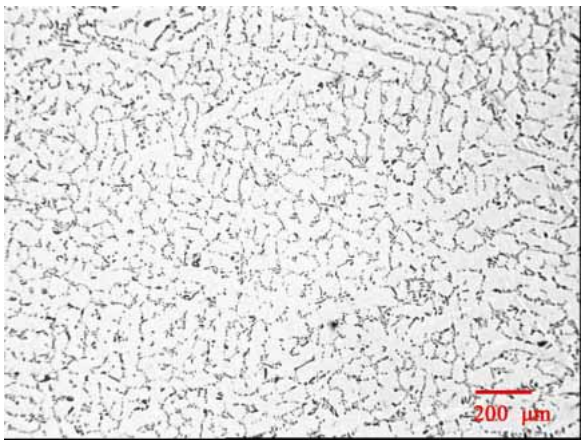
casting and the EDX analysis result has been shown in Figure 4.79. The presence of oxygen at the internal surface of pore, therefore, suggested that oxide films might associate with the formation of shrinkage porosity in the castings.



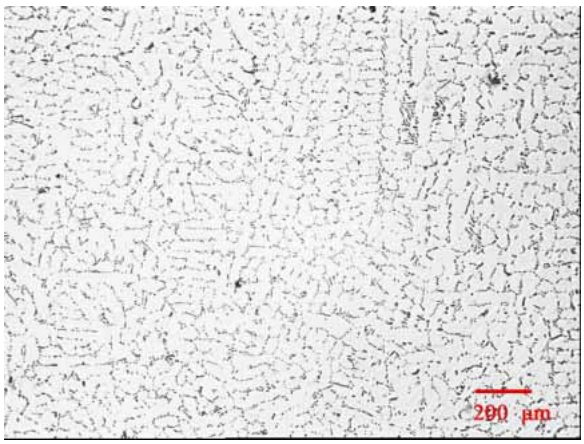
(a) low oxide film, low shrinkage



(b) low oxide film, high shrinkage



(c) high oxide film, low shrinkage



(d) high oxide film, high shrinkage

Figure 4.76 Optical micrograph showing microstructures of the castings for 4 experimental combinations.

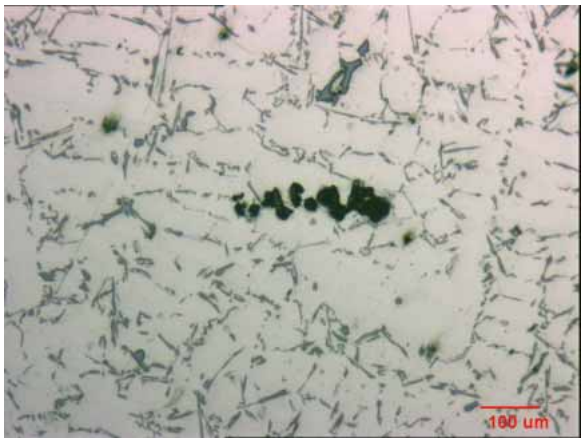


Figure 4.77 Optical micrograph showing shrinkage porosity in the high oxide film and high shrinkage casting.

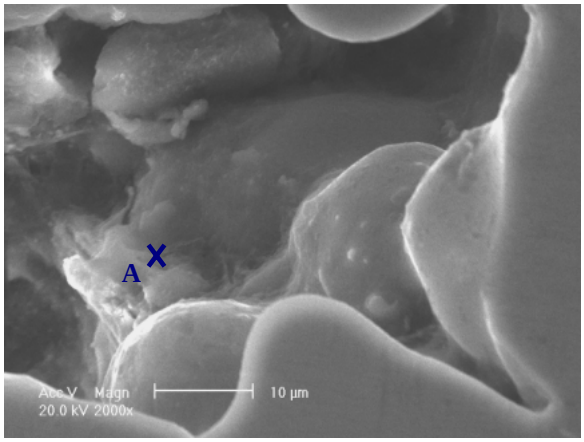


Figure 4.78 The scanning electron micrograph obtained from the high oxide film and high shrinkage casting showing oxide film at the surface of microporosity.

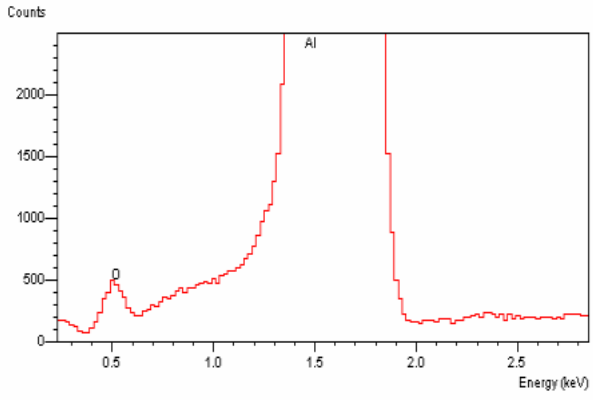


Figure 4.79 The EDX analysis results obtained from point A in figure 4.78.

4.2.1.6 Image analysis

The micrographs obtained from the runner bars of each experimental combination were subjected to image analysis. Table 4.18 shows the results of porosity area, number of pores per cm^2 and mean pore size obtained by image analysis. As might be expected the combination of low oxide film and low shrinkage had the lowest values (0.38 % porosity area, 1554 pores/cm^2 and 245 μm^2 respectively). The porosity values obtained were at the same level as the results of the low hydrogen (0.1 ml/100g metal) and low oxide film casting in the previous experiment (see Table 4.9). The results showed that increasing oxide film content influenced the presence of porosity in the casting, particularly the number of pores. For example, in the low shrinkage castings the increase in oxide film content resulted in an increase in number of pores by 10% (from 1554 to 1724 pores/cm^2), while increasing the amount of shrinkage in this experiment appeared to have no significant effect on the presence of porosity.

Table 4.18 Image analysis results obtained from 4 experimental combinations.

Combination	Porosity area (%)	Number of pore per cm^2	Mean pore size (μm^2)
low oxide film, low shrinkage	0.38	1554	245
low oxide film, high shrinkage	0.49	1565	313
high oxide film, low shrinkage	0.55	1724	319
high oxide film, high shrinkage	0.49	1698	289

Tables 4.19, 4.20 and 4.21 show the Yate's algorithm calculation obtained from the porosity area, number of pores per cm^2, and pore size results respectively. Pareto diagrams illustrating the relative effects of oxide films, shrinkage and their interactions have been shown in Figures 4.80a, 4.80b and 4.80c respectively. These show that oxide film (column A) had some effect on the formation of porosity, particularly the number of pores. The increase in oxide film content resulted in an increase in the numbers of pores of about 10% or 150 pores/cm^2 in the castings. The Pareto diagrams also suggested that

the interaction between oxide film and shrinkage had an effect on the size of pores by increasing pore size by about 20% or 50 μm^2.

Table 4.19 The effect of oxide film, shrinkage and their interactions on porosity area using Yate's algorithm.

	total	1	2	estimate of effect
(1)	0.38	0.93	1.91	0.96
Effect of oxide film: A	0.55	0.98	0.17	0.09
Effect of shrinkage: B	0.49	0.17	0.05	0.03
AB	0.49	0.00	-0.17	-0.09

Table 4.20 The effect of oxide film, shrinkage and their interactions on number of pores per cm^2 using Yate's algorithm.

	total	1	2	estimate of effect
(1)	1554	3278	6541	3270.50
Effect of oxide film: A	1724	3263	303	151.50
Effect of shrinkage: B	1565	170	-15	-7.50
AB	1698	133	-37	-18.50

Table 4.21 The effect of Oxide film, Shrinkage and their interactions on pore size using Yate's algorithm.

	total	1	2	estimate of effect
(1)	245	564	1166	583.00
Effect of oxide film: A	319	602	50	25.00
Effect of shrinkage: B	313	74	38	19.00
AB	289	-24	-98	-49.00

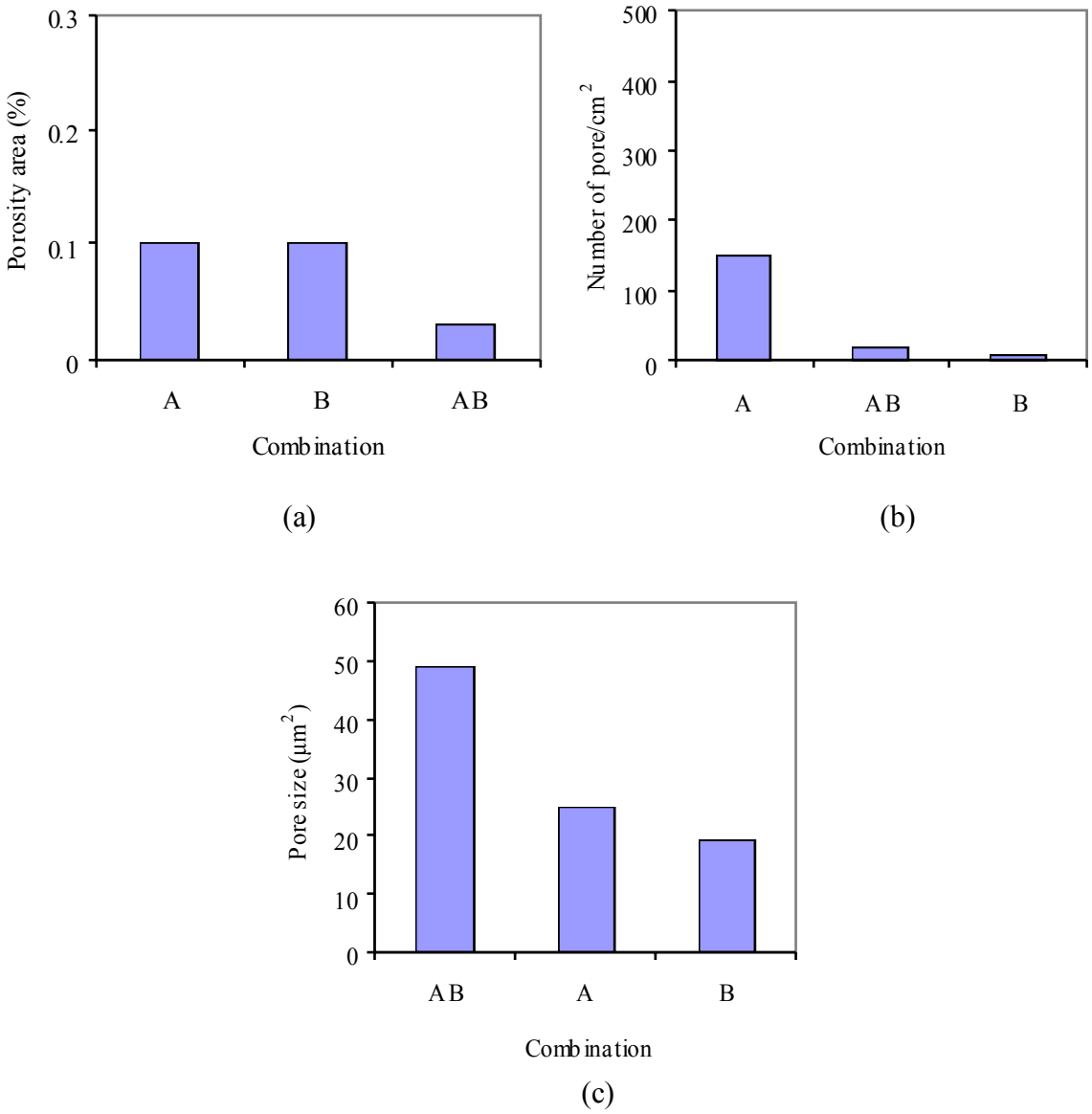


Figure 4.80 Pareto diagrams showing the effects of two defects and their interrelationships on (a) the porosity area (b) the number of pore per cm^2 and (c) the pore size (A = effect of oxide film, B = effect of shrinkage).

4.2.2 Interactions between oxide film and shrinkage porosity in cast Al-7Si-0.2Mg-1.1Fe alloy

4.2.2.1 Tensile properties

Tables 4.22 and 4.23 show the UTS and elongation values obtained from the 4 types of castings. The results demonstrated that the high oxide film and high shrinkage castings had the lowest UTS (of 229 MPa), while the best UTS was obtained from the low oxide film and high shrinkage combination (of 236 MPa). It can be seen that the mean elongation of all castings in this experiment was about 0.5%. As shown in the previous experiment (section 4.1), the Fe-rich phase had the greatest effect on tensile properties, therefore the UTS and elongation values obtained from this experiment (1.1 wt% Fe) were very low compared to the low Fe content castings, 0.1 wt% Fe, (see Tables 4.1, 4.2, 4.13 and 4.14). The increase in oxide film defects resulted in a slight reduction in the tensile properties, particularly the UTS, while the shrinkage porosity introduced in this experiment had a negligible effect on both UTS and elongation.

4.2.2.2 Pareto diagram of tensile properties

Figures 4.81a and 4.81b respectively show the relative effects of the oxide film and shrinkage porosity defects on the UTS and elongation and their interrelationships obtained from the results of the calculation using Yates' algorithm, (shown in Tables 4.24 and 4.25). The oxide film defects had a small effect on the tensile properties (column A) by decreasing the UTS by about 6 MPa or 3% of the mean UTS values, which was the same level as in the previous experiment examining the interactions between oxide film and shrinkage porosity in cast Al-7Si-0.3Mg-0.1Fe alloy (section 4.2.1). The Pareto diagrams also showed that there was no noticeable effect produced by shrinkage (column B) or interaction between oxide films and shrinkage (column AB) in this experiment.

Table 4.22 Ultimate Tensile Strength (UTS) values of Al-7Si-0.2Mg-1.1Fe alloy for 4 experimental combinations.

Test bar No.	Ultimate Tensile Strength (MPa)			
	Low oxide film and low shrinkage	Low oxide film and high shrinkage	High oxide film and low shrinkage	High oxide film and high shrinkage
1	253.61	257.12	249.59	228.12
2	251.45	242.41	232.58	241.35
3	234.85	253.40	239.74	252.08
4	248.56	248.61	225.42	144.45
5	244.59	241.35	230.97	198.45
6	222.59	243.65	235.45	237.78
7	254.51	211.76	176.45	231.70
8	228.36	219.38	208.77	222.94
9	258.84	237.99	239.38	233.49
10	188.68	259.72	230.60	254.58
11	207.80	241.34	233.64	227.41
12	193.37	233.04	245.66	238.67
13	222.59	261.97	251.40	233.13
14	235.39	220.72	196.30	228.48
15	245.68	218.91	259.23	205.45
16	255.05	241.35	216.11	252.37
17	247.84	211.39	226.42	233.71
18	248.16	240.80	264.45	207.58
19	242.78	171.24	245.08	233.53
20	244.21	241.35	168.30	238.50
21	220.62	251.40	237.97	209.00
22	253.51	247.09	225.89	211.49
23	240.64	236.69	215.05	242.95
24	236.39	234.26	250.06	231.40
25	240.99	231.43	234.26	246.40
26	231.47	242.06	236.62	232.24
27	229.89	233.73	239.64	248.65
28	195.54		198.58	228.75
29			240.63	229.36
30				244.27
Mean UTS (MPa)	234.93	236.08	229.46	228.94

Table 4.23 Elongation values of Al-7Si-0.2Mg-1.1Fe alloy for 4 experimental combinations.

Test bar No.	Elongation (%)			
	Low oxide film and low shrinkage	Low oxide film and high shrinkage	High oxide film and low shrinkage	High oxide film and high shrinkage
1	0.68	0.72	0.82	0.52
2	0.62	0.54	0.54	0.60
3	0.56	0.62	0.66	0.68
4	0.76	0.31	0.37	0.10
5	0.56	0.52	0.41	0.24
6	0.36	0.48	0.64	0.60
7	0.80	0.28	0.16	0.62
8	0.52	0.37	0.24	0.64
9	0.82	0.50	0.88	0.49
10	0.25	0.66	0.64	0.88
11	0.33	0.50	0.52	0.49
12	0.31	0.52	0.60	0.66
13	0.35	0.70	0.60	0.60
14	0.48	0.33	0.24	0.60
15	0.56	0.32	1.12	0.40
16	0.72	0.64	0.33	0.62
17	0.66	0.39	0.34	0.70
18	0.78	0.52	0.88	0.40
19	0.56	0.11	0.52	0.60
20	0.64	0.64	0.12	0.58
21	0.39	0.61	0.48	0.38
22	0.94	0.82	0.41	0.42
23	0.52	0.39	0.42	0.66
24	0.54	0.41	0.68	0.46
25	0.48	0.41	0.46	0.60
26	0.54	0.47	0.48	0.60
27	0.56	0.46	0.37	0.50
28	0.30		0.21	0.33
29			0.84	0.50
30				0.64
Mean Elongation (%)	0.54	0.49	0.52	0.54

Table 4.24 The effect of oxide film, shrinkage and their interactions to ultimate tensile strength (UTS) using Yate's algorithm.

	total	1	2	estimate of effect
(1)	234.93	464.39	929.41	464.71
effect of oxide film: A	229.46	465.02	-12.61	-6.31
effect of shrinkage: B	236.08	-5.47	0.63	0.31
AB	228.94	-7.14	-1.67	-0.84

Table 4.25 The effect of oxide film, shrinkage and their interactions to elongation using Yate's algorithm.

	total	1	2	estimate of effect
(1)	0.54	1.06	2.09	1.05
effect of oxide film: A	0.52	1.03	0.03	0.02
effect of shrinkage: B	0.49	-0.02	-0.03	-0.02
AB	0.54	0.05	0.07	0.04

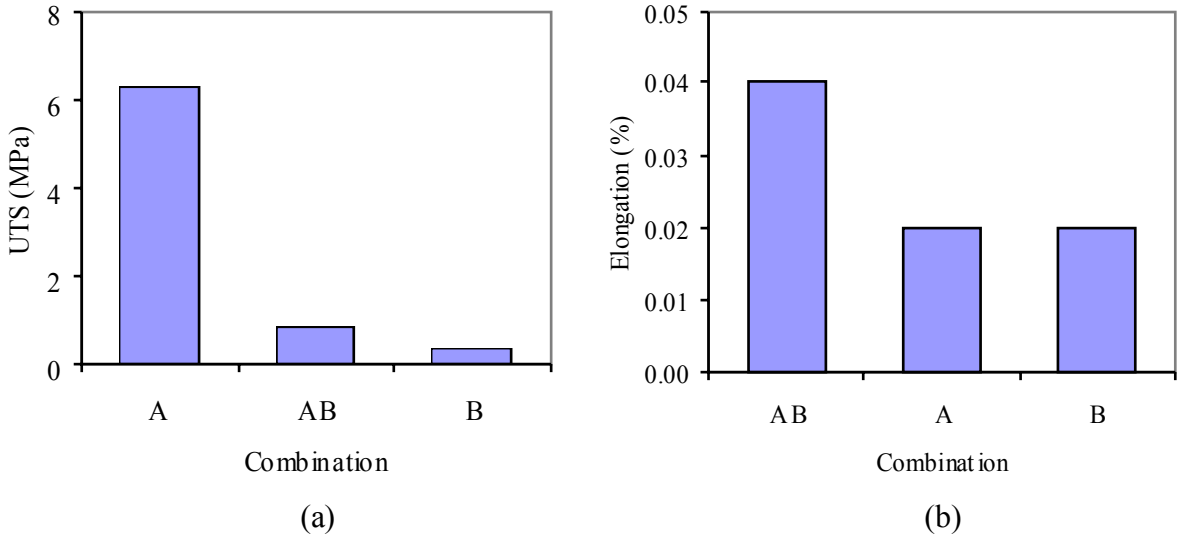
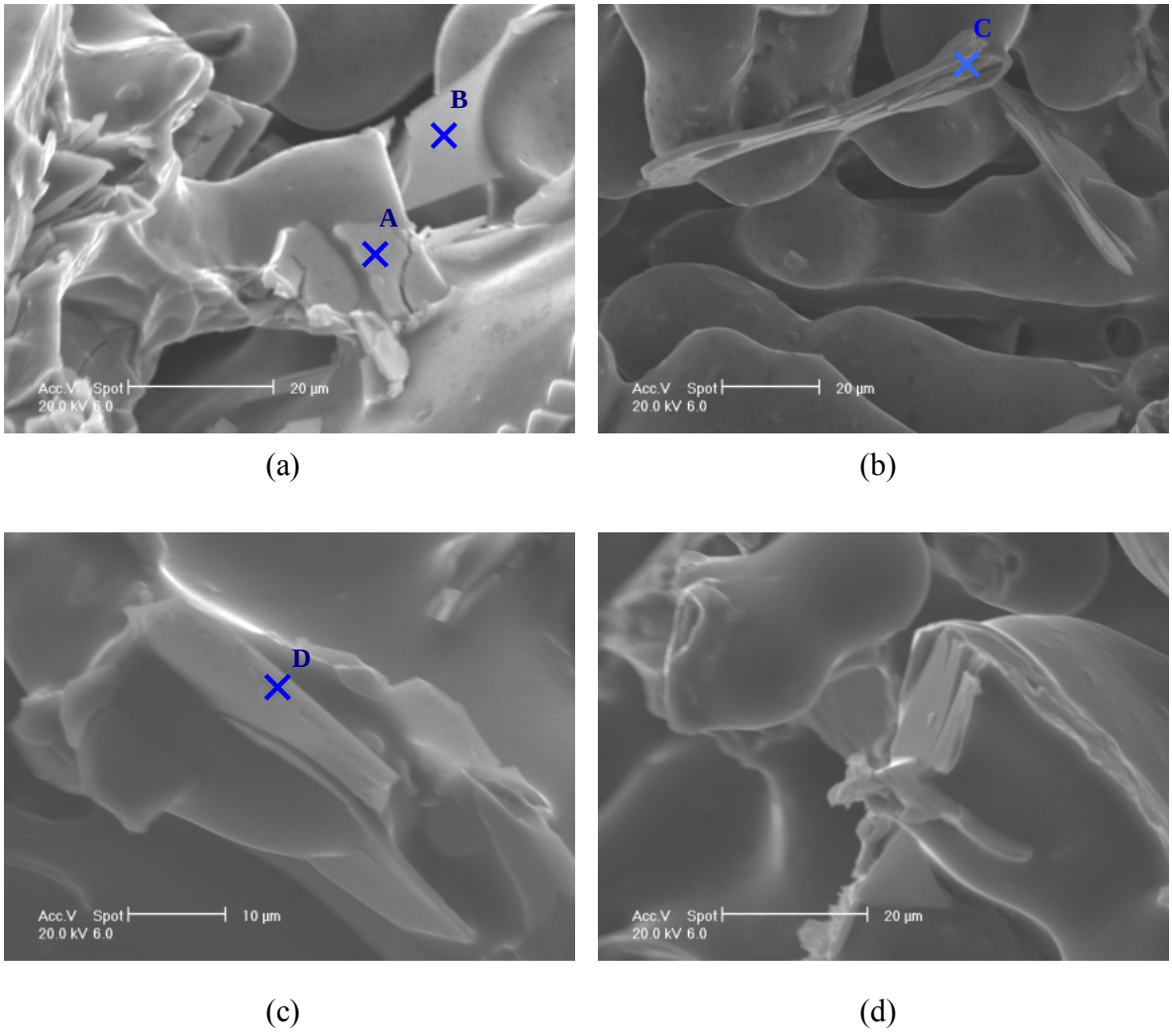


Figure 4.81 Pareto diagrams showing the effects of two defects and their inter-relationship on (a) the UTS (b) the percent elongation value of the castings (A = effect of oxide film, B = effect of Shrinkage).

4.2.2.3 Examination of fracture surfaces

The fracture surfaces of test bars were examined by scanning electron microscopy. Figures 4.82a to 4.82d show SEM images of fracture surfaces and the associated EDX analysis results have been shown in Figures 4.83a to 4.83d. The images revealed that the most frequent microstructural defect observed was β-Al_5FeSi phase, with a platelet-like morphology. The Fe-rich phase was brittle and appeared to be the initiator of fracture in the castings since cracks in the Fe-rich phases were found on the fracture surface of all test bars. Therefore, the presence of Fe-rich phase, particularly the β-Al_5FeSi platelet, was a major cause in the reduction in tensile properties of the casting.



(a) (b)

(c) (d)

Figure 4.82 The scanning electron micrographs obtained from the fracture surfaces of the test bars showing the brittle platelet morphology of Fe-rich phase.

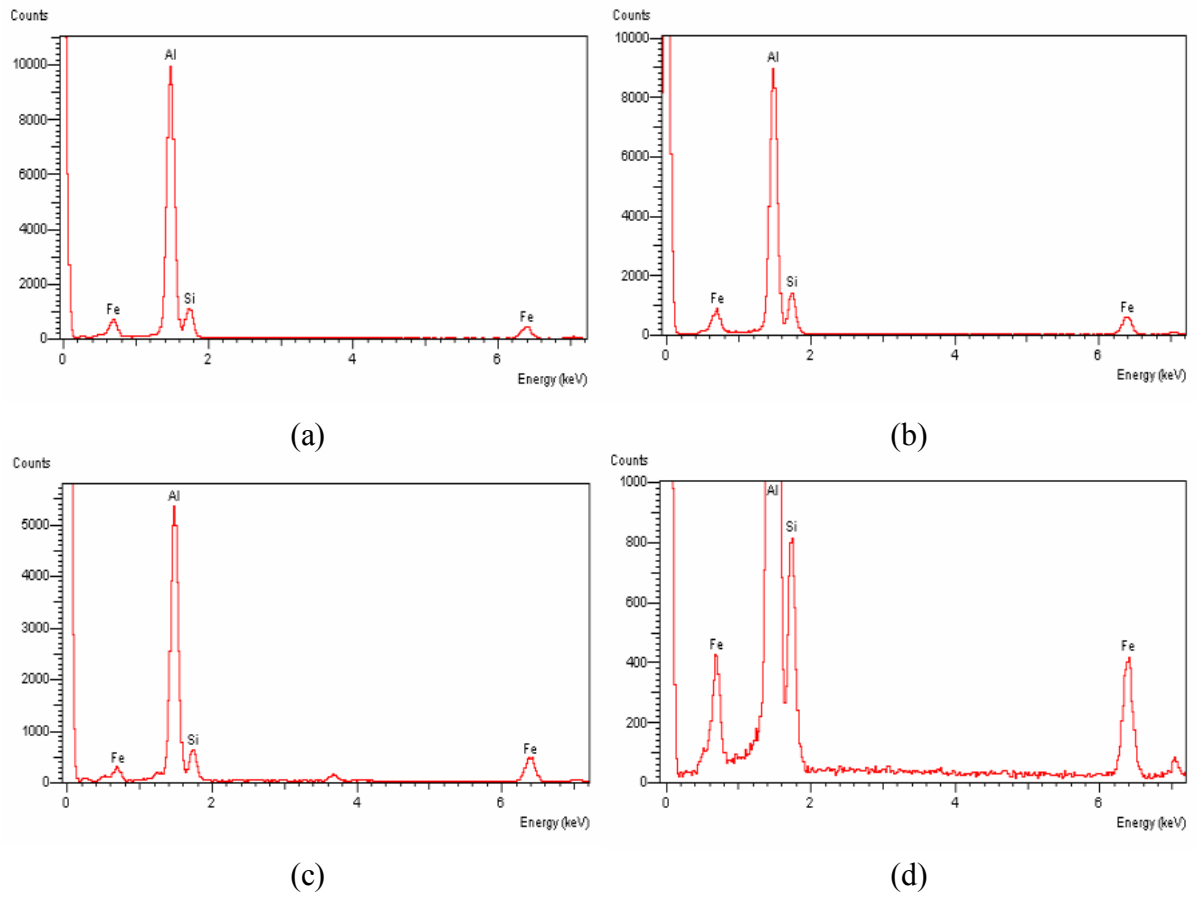


Figure 4.83 The EDX analysis results obtained from points A to D in figures 4.82a to 4.82c.

The fracture surfaces of the lowest UTS test bar (test bar 4, 145 MPa) of the high oxide film and high shrinkage castings have been shown in Figure 4.84. It can be seen that both sides of the fracture surfaces contained large oxide films. Figures 4.85a to 4.85d show higher magnification SEM images of the fracture surfaces and their EDX analysis results have been shown in Figures 4.86a to 4.86d. These show the double nature of the oxide film defect, with no bond between the surfaces, and that it was the type of defect that could be opened by the fracture. The large double oxide films influenced the tensile properties of the casting, significantly decreasing the UTS by about 85 MPa from the mean UTS of about 230 MPa.

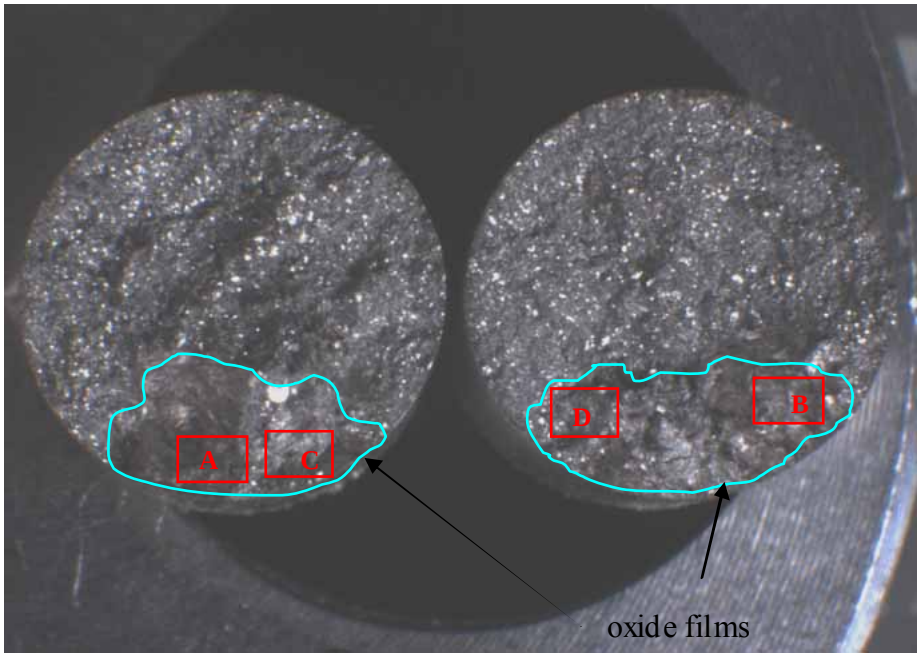
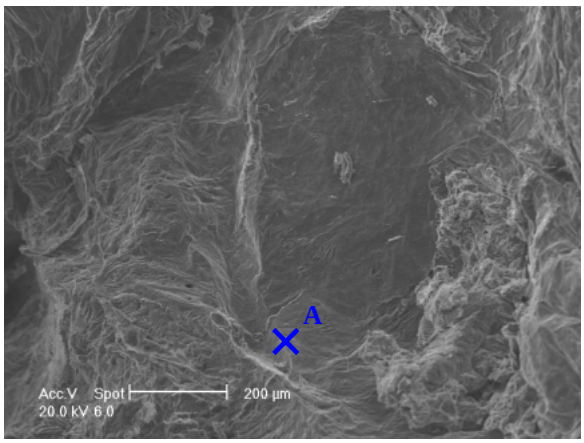
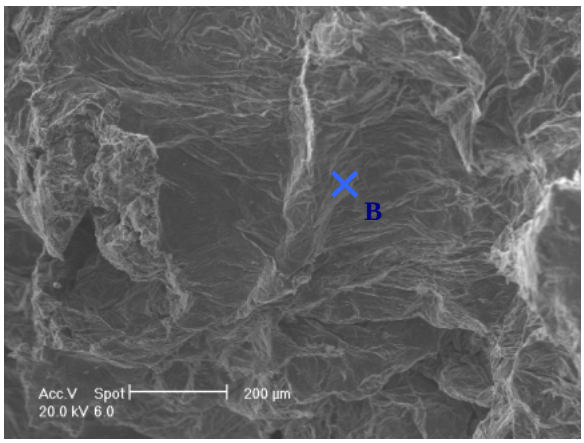


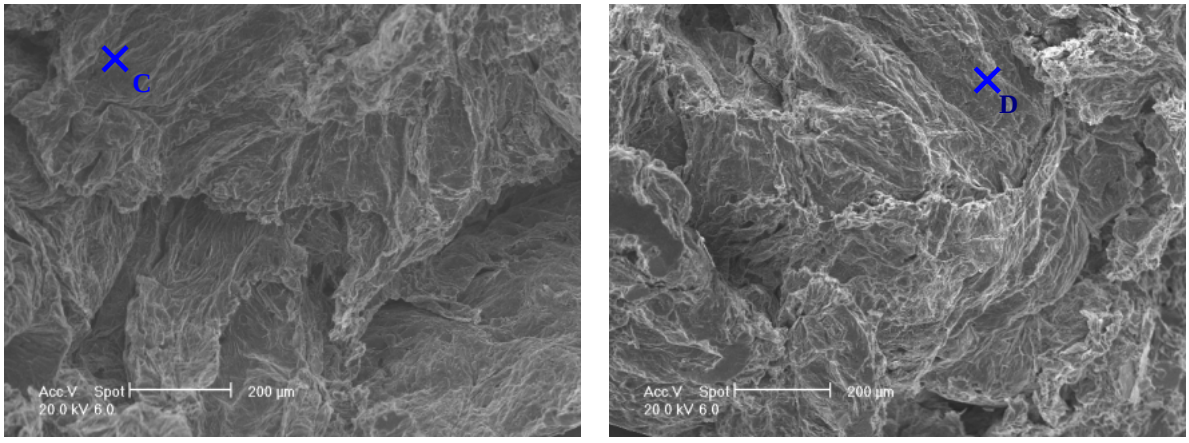
Figure 4.84 Photograph showing the large double oxide film defect on the fracture surfaces of test bar 4 obtained from the high oxide film and high shrinkage casting.



(a)

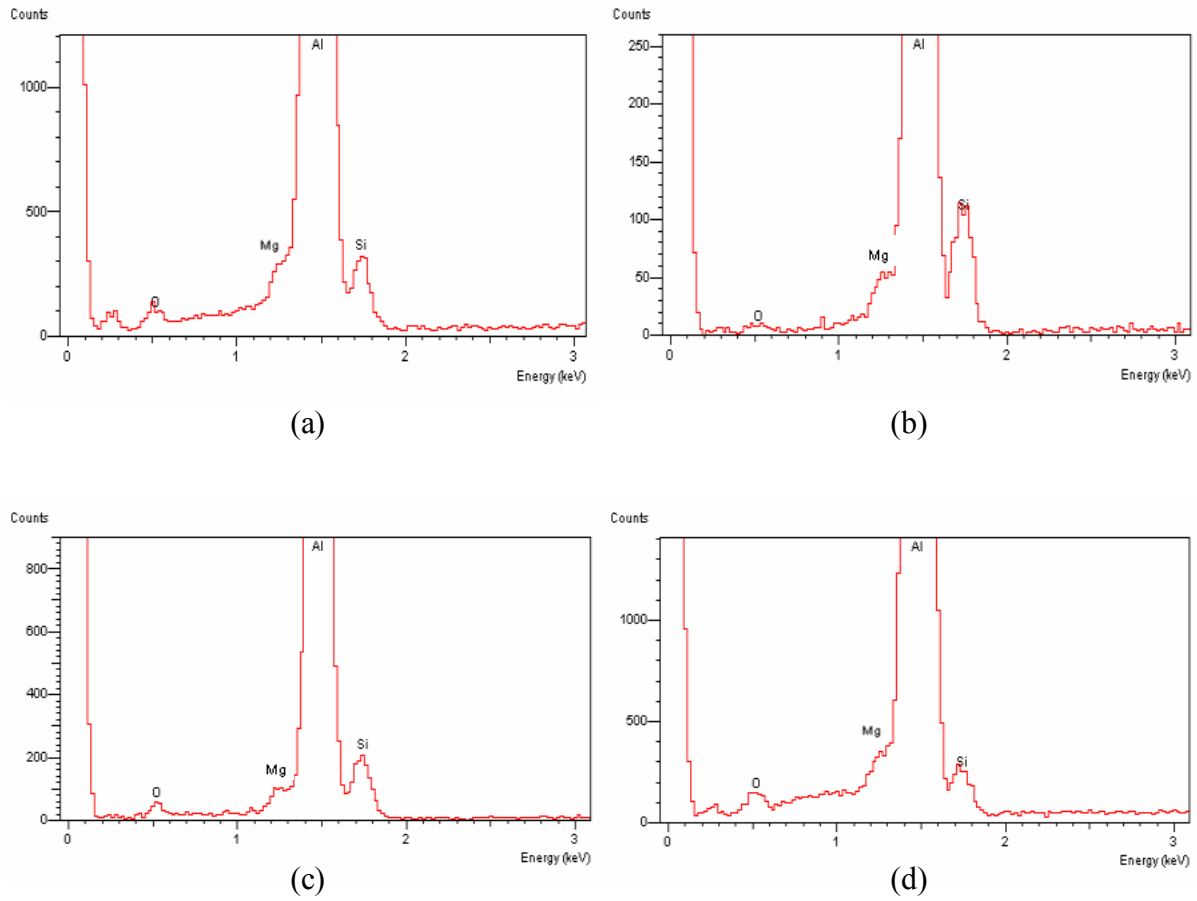


(b)



(c) (d)

Figure 4.85 The scanning electron micrographs showing the close-up images of oxide films on the fracture surfaces from areas A to D in Figure 4.84.

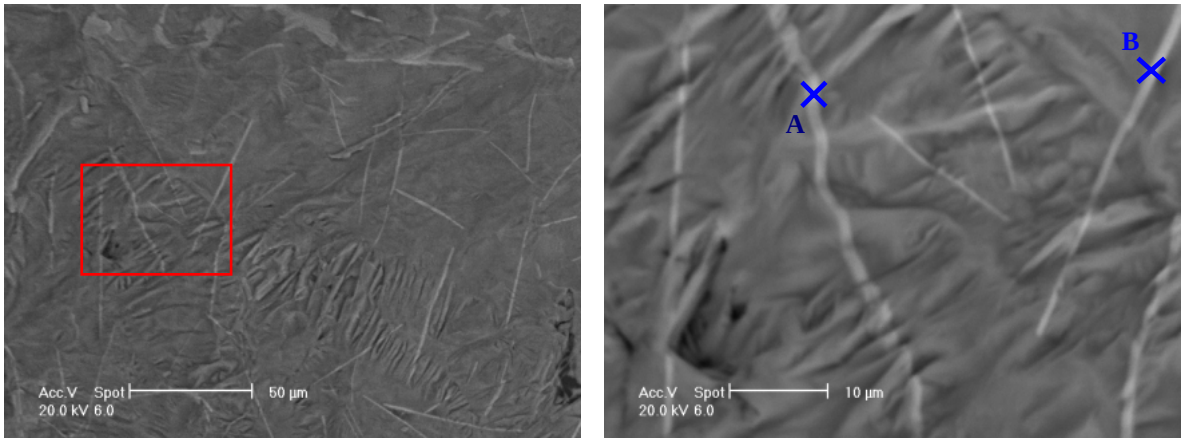


(a) (b)

(c) (d)

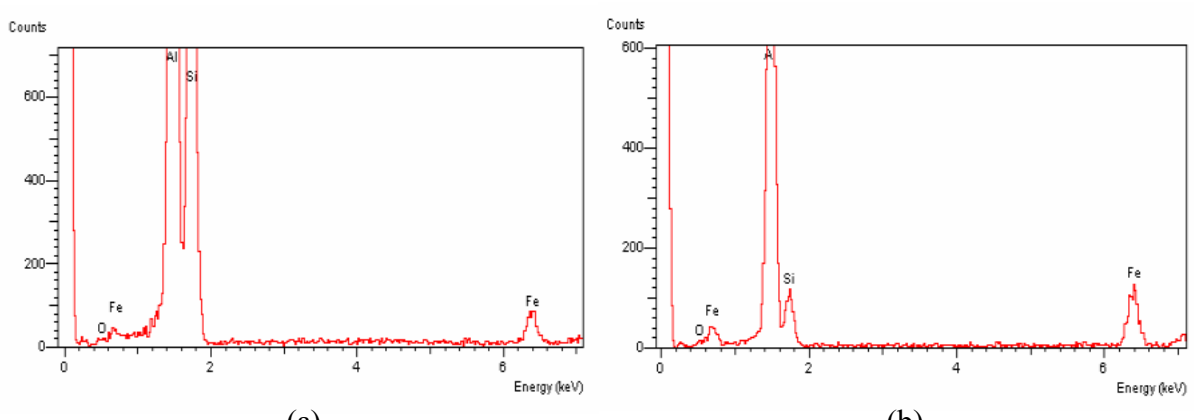
Figure 4.86 The EDX analysis results obtained from points A to D in figures 4.85a to 4.85d.

The SEM images also suggested an interaction between Fe-rich phases and oxide films, in that the oxide film was a nucleation site for the Fe-rich phase. Figure 4.87a and 4.87b show the back-scattered image of wrinkled oxide film on the fracture surface of test bar 4 obtained from the high oxide film and high shrinkage casting. It suggests the nucleation of β-Al_5FeSi phase onto the wetted underside of the oxide film, which could be observed through the thin film as a light needle-like morphology. Figures 4.88a and 4.88b show associated EDX analysis results revealing the presence of O and Fe. Figures 4.89a to 4.89d show more evidence of the nucleation of β-Al_5FeSi phase on the underside of an oxide film, obtained from test bar 5 from a high oxide film and high shrinkage casting. The EDX analysis of the Fe-rich phase has been shown in Figure 4.90, again revealed the presence of oxygen.



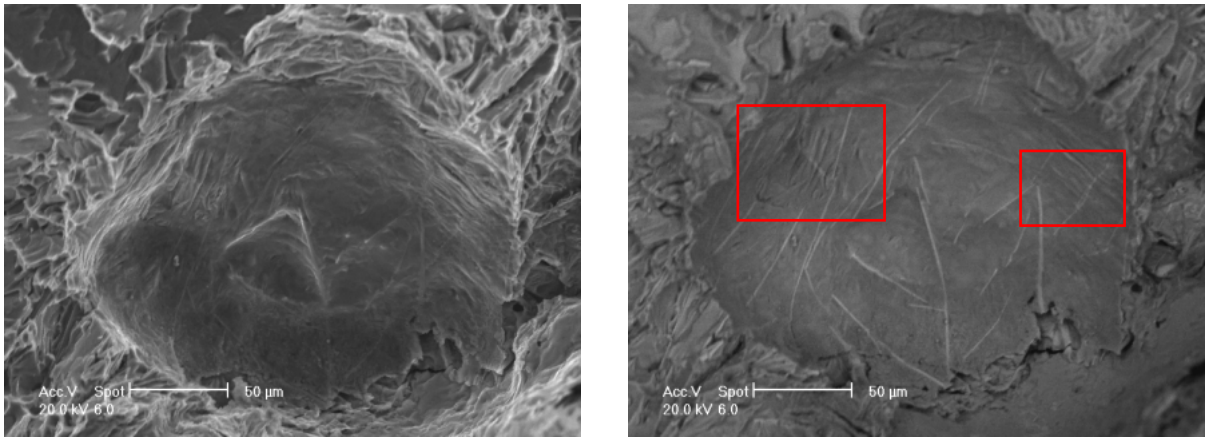
(a) (b)

Figure 4.87 The scanning electron micrographs obtain from test bar 4 of the high oxide film and high shrinkage casting (a) showing the back-scattered image of oxide film on the fracture surface, and (b) higher magnification image obtained from Figure 4.84a showing the Fe-rich phases nucleated underneath oxide film.

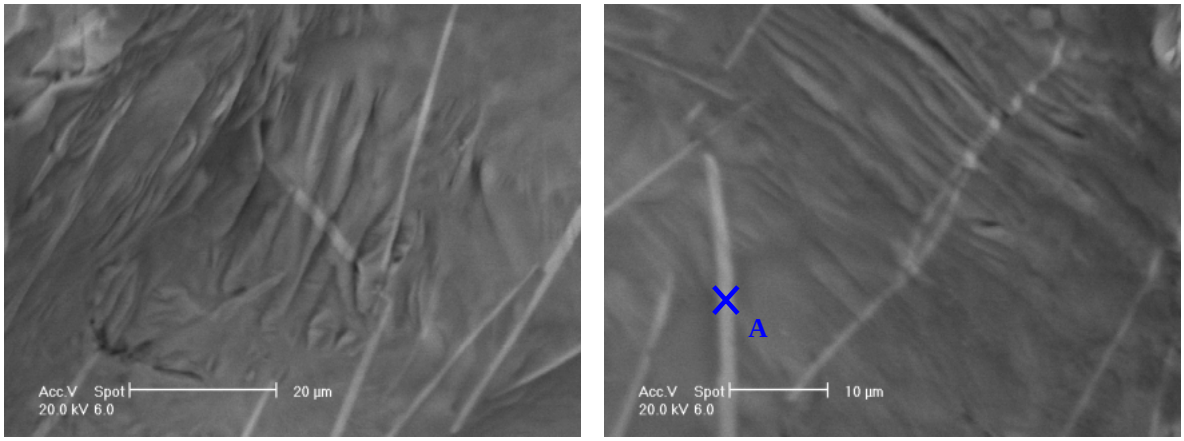


(a) (b)

Figure 4.88 The EDX analysis results obtained from points A and B in figures 4.87b.



(a) (b)



(c) (d)

Figure 4.89 The scanning electron micrographs obtain from test bar 5 of the high oxide film and high shrinkage casting showing (a) oxide film on the fracture surface, (b) the back-scattered image of Figure 4.89a, (c) and (d) the close-up observation of the Fe-rich phases nucleated on oxide film obtained from Figure 4.89b.

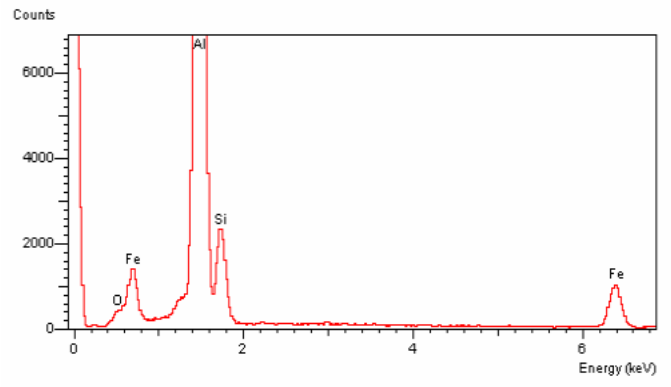


Figure 4.90 The EDX analysis result obtained from point A in figure 4.89d.

Figure 4.91 shows the SEM image of fracture surface obtained from the high oxide film and low shrinkage casting and the EDX analysis results have been shown in Figures 4.92a to 4.92c. These suggest the interaction between Fe-rich phase and porosity that the large β-phase platelets, which located in the interdendritic region, caused the presence of microporosity between them. The EDX analysis results also show that some Fe-rich phase associated with oxide films.

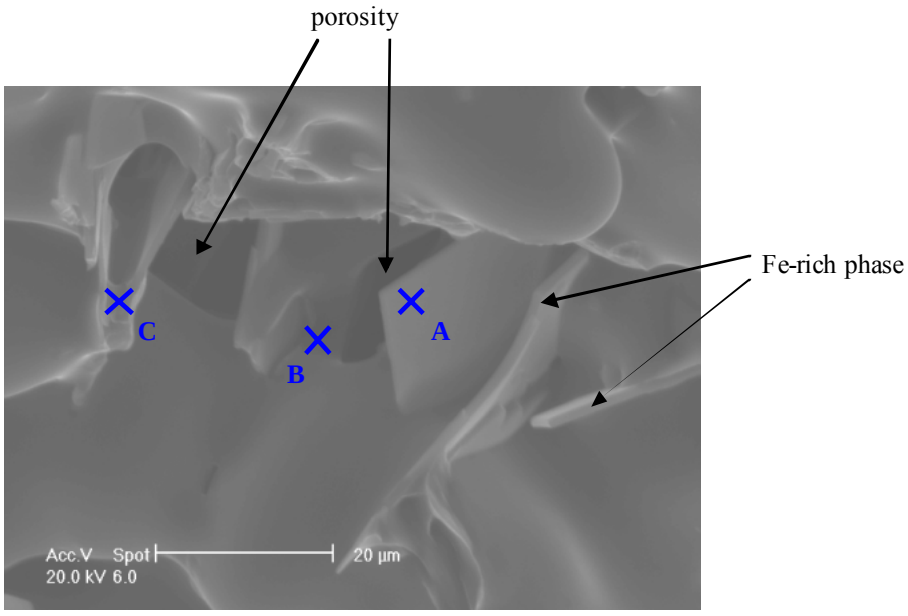
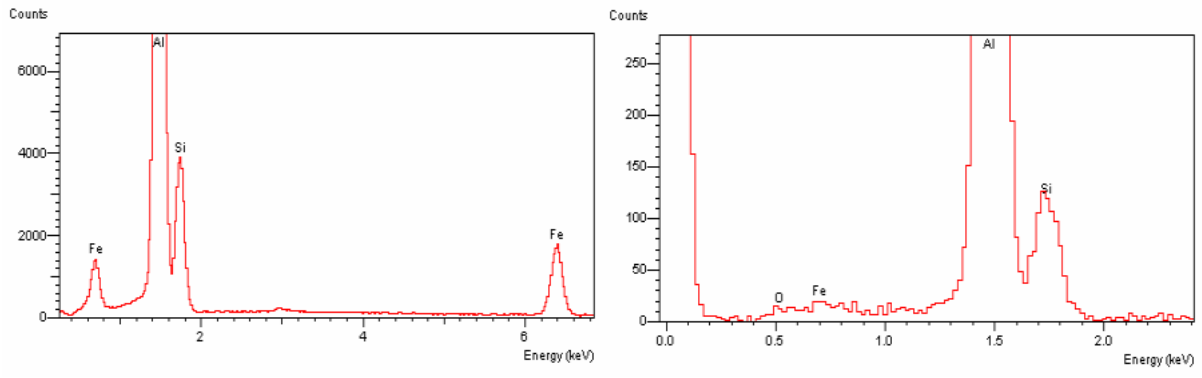
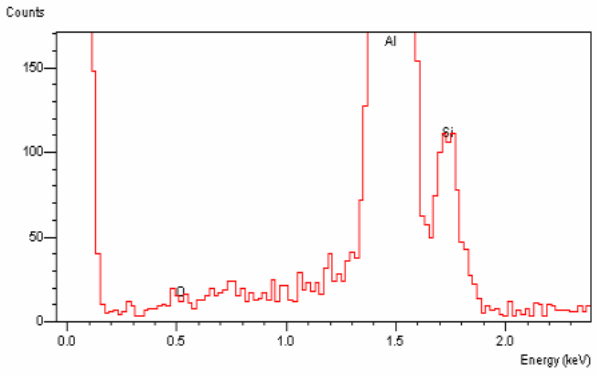


Figure 4.91 The scanning electron micrographs obtained form the fracture surface of the high oxide film and low shrinkage casting showing microporosity in the interdendritic region associated with Fe-rich phases and oxide film.



(a) (b)



(c)

Figure 4.92 The EDX analysis results obtain from points A to C in Figure 4.91.

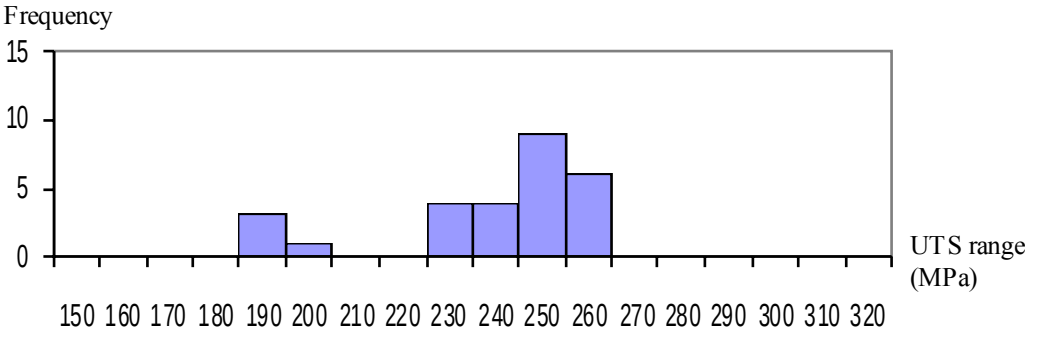
4.2.2.4 Weibull analysis

Figures 4.93 and 4.94 show distribution histograms of the UTS and percent elongation data respectively obtained from the 4 types of castings. It can be seen that the distributions of tensile property data from the experiment were not normally distributed, therefore, the Weibull distribution model was used to describe them. Figures 4.95a to 4.95c show graphs of probability of fracture versus UTS and Weibull plots obtained from the UTS data. The graphs of probability of fracture versus elongation and Weibull

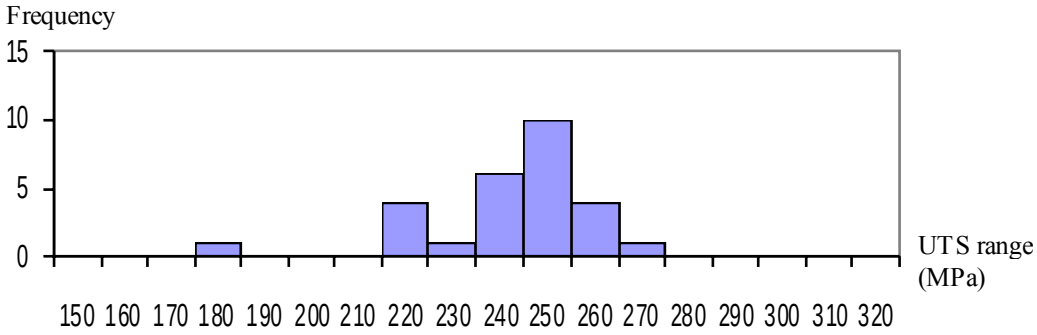
plots obtained from the elongation data have been shown in Figures 4.96a to 4.96c. The Weibull modulus and R values obtained from the UTS and elongation data for all experimental combinations have been shown in Table 4.26.

The results showed that the Weibull modulus of all experimental combinations were low compared to the previous experiment examining interactions between oxide film and shrinkage porosity in the low Fe content alloy (Table 4.17). For example, in the low oxide film and low shrinkage castings, The UTS and elongation Weibull modulus were about 14 and 3.6 respectively while they were about 52 and 4.5 in the previous experiment. The more widely spread tensile properties in this experiment, therefore, was caused by the increase in Fe-rich phases in the casting. This supported the results obtained from the experiment investigating interactions between Fe-rich phase, hydrogen porosity and oxide films that Fe-rich phase influence the reliability of tensile properties of cast aluminium alloys by decreasing the Weibull modulus (see column A in Figure 4.34).

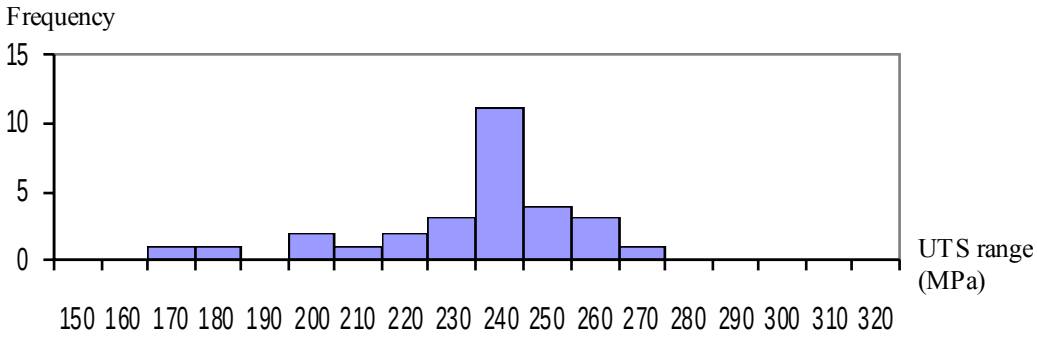
Increasing oxide film defects appeared to have no significant effects on Weibull modulus, for example, the increase in oxide film in the high shrinkage castings resulted in a slight decrease in the UTS and elongation Weibull modulus of about 2.5 and 1.4 respectively. The results also showed that the shrinkage porosity produced in this experimental level did not noticeably influence the Weibull modulus.



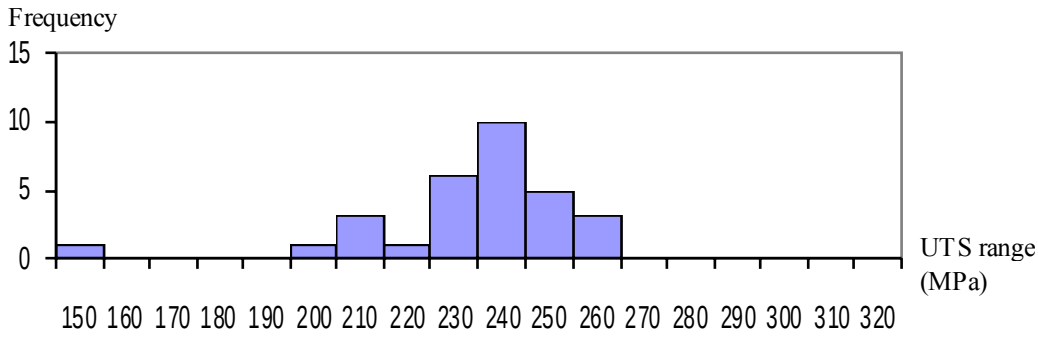
(a) low oxide film, low shrinkage



(b) low oxide film, high shrinkage

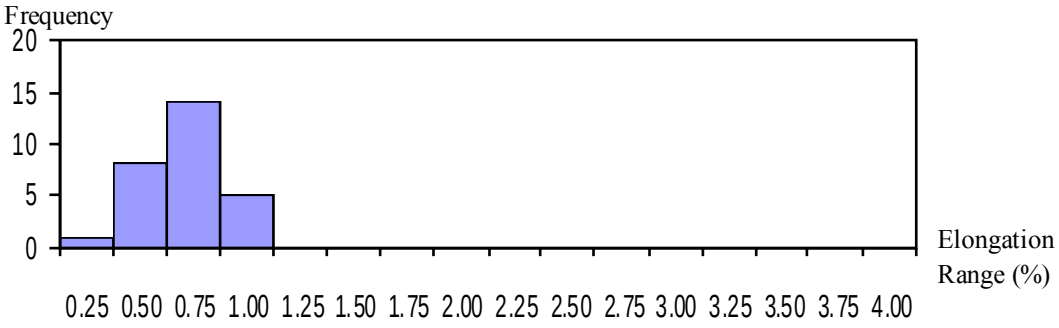


(c) high oxide film, low shrinkage

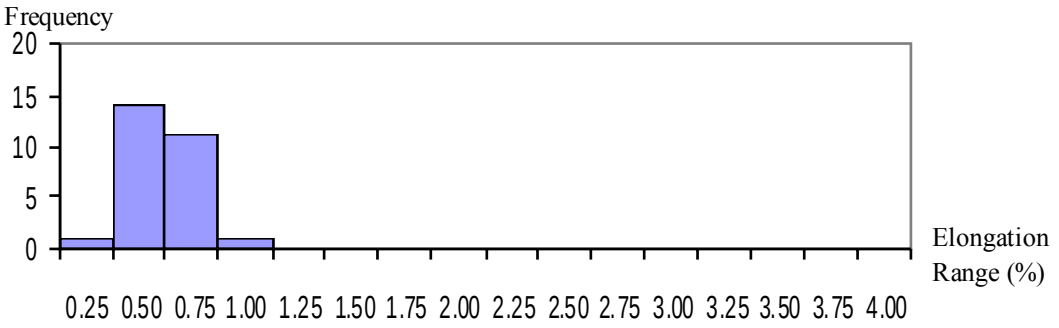


(d) high oxide film, high shrinkage

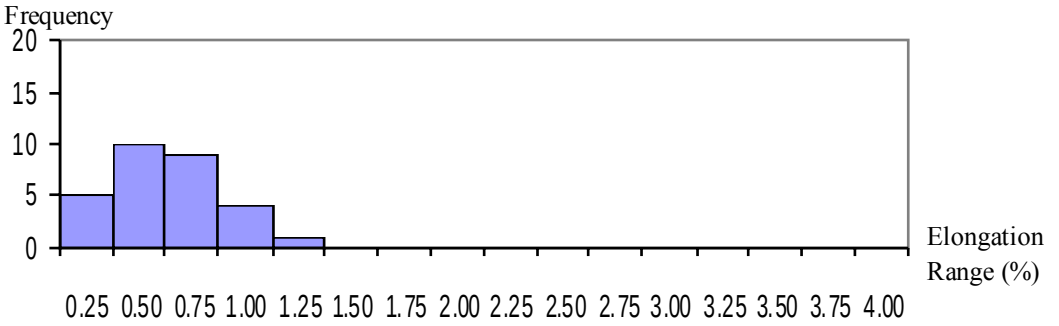
Figure 4.93 Frequency plots of ultimate tensile strength (UTS).



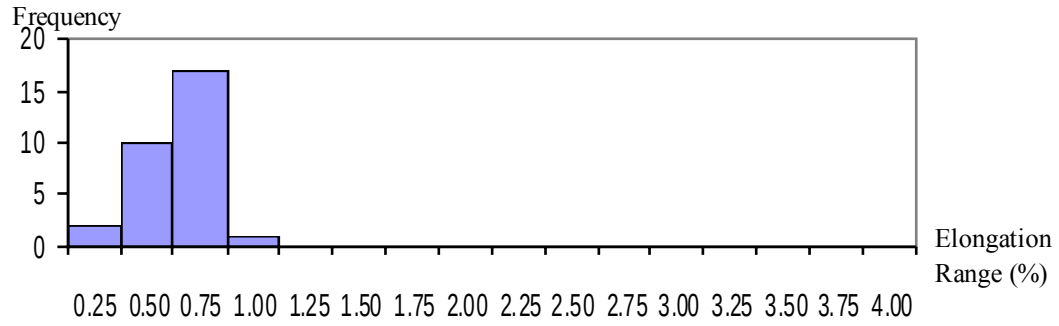
(a) low oxide film, low shrinkage



(b) low oxide film, high shrinkage



(c) high oxide film, low shrinkage



(d) high oxide film, high shrinkage

Figure 4.94 Frequency plots of percent elongation.

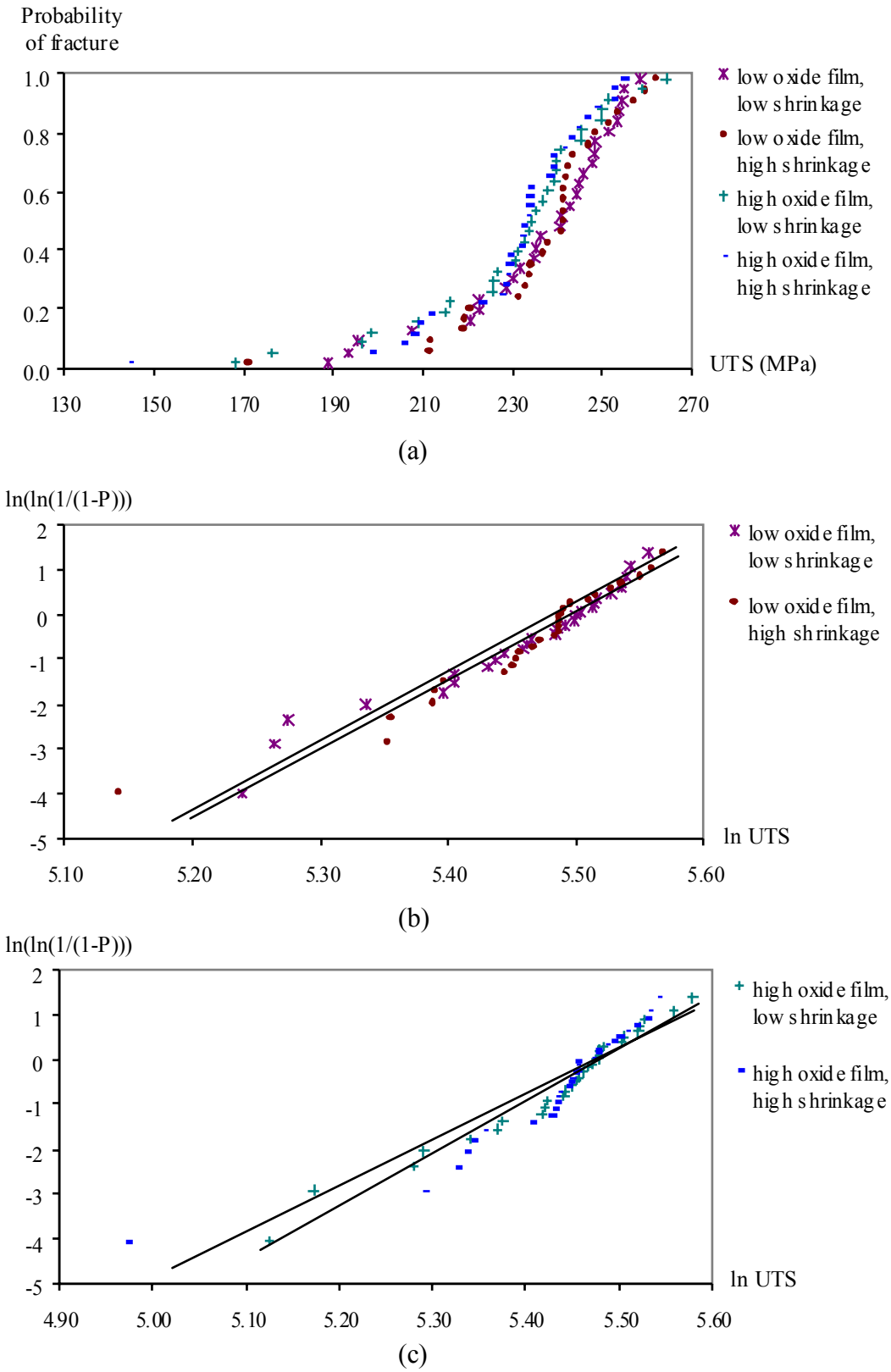
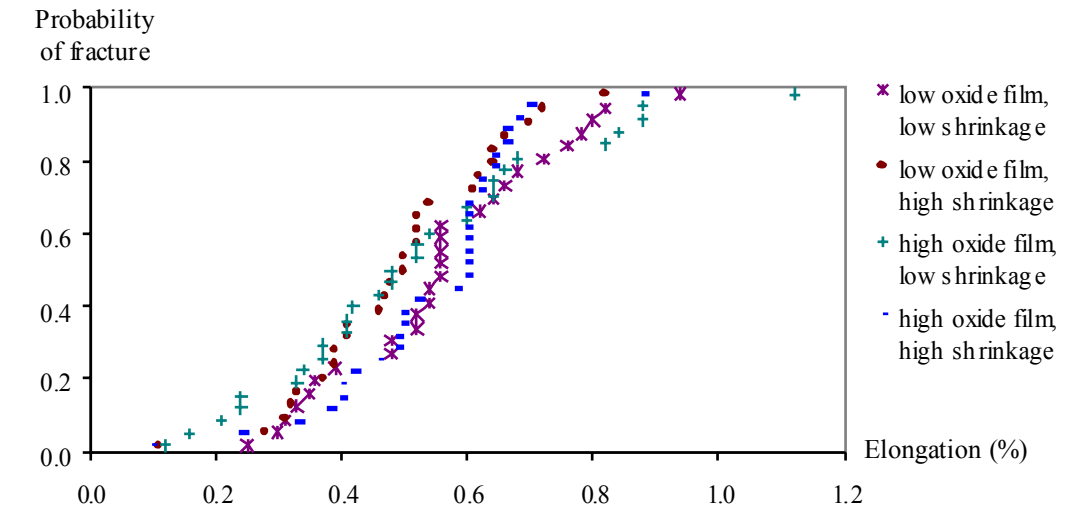
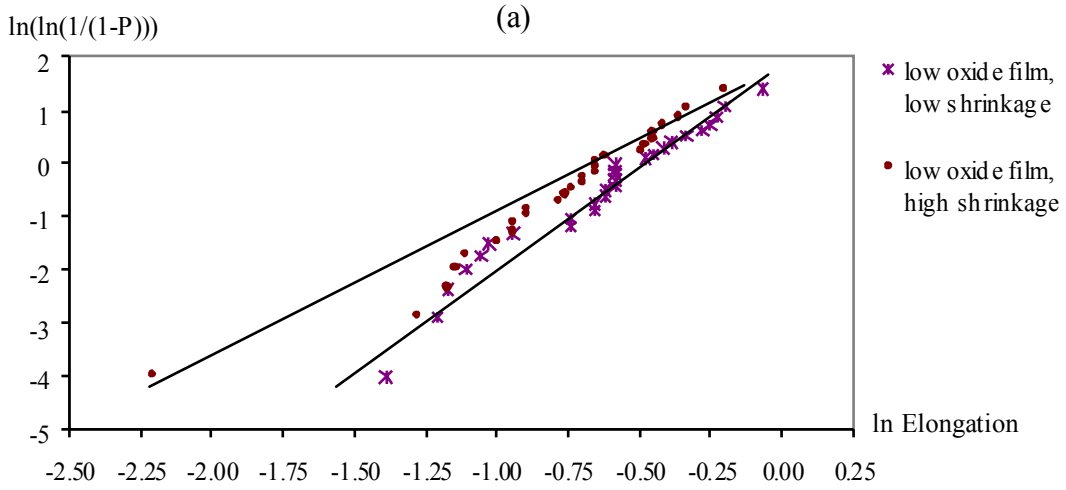


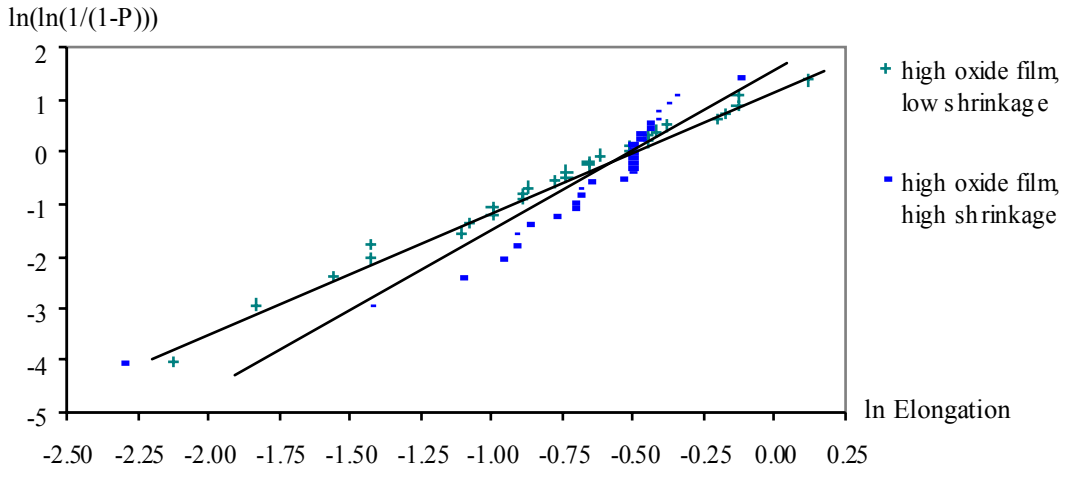
Figure 4.95 The graphs showing a) cumulative plots, b) and c) Weibull plots of ultimate tensile strength (UTS) data.



(a)



(b)



(c)

Figure 4.96 The graphs showing a) cumulative plots, b) and c) Weibull plots of percent elongation data.

Table 4.26 Weibull modulus values obtained from the Weibull plots of ultimated tensile strength (UTS) (Figures 4.95b and 4.95c) and percent elongation (Figures 4.96b and 4.96c).

Combination	UTS Weibull modulus	R	Elongation Weibull modulus	R
low oxide film, low shrinkage	14.2	0.98	3.64	0.98
low oxide film, high shrinkage	14.0	0.96	3.04	0.97
high oxide film, low shrinkage	11.7	0.98	2.37	0.99
high oxide film, high shrinkage	10.8	0.92	2.92	0.93

The Weibull plots and the results in Table 4.26 show that, although the Weibull moduli in this experiment were low, the tensile property data plotted linearly as in a single defect Weibullian distribution manner. This means that the test bars had the same failure mechanism, caused by brittle Fe-rich phases in the casting, as shown in Figures 4.82a to 4.82d. However, the presence of double oxide film defect influenced the distribution of data by decreasing the R value of Weibull modulus. For example, increasing oxide films in the high shrinkage castings resulted in a decrease in the R value of the UTS Weibull modulus from 0.98 to 0.92. Figure 4.95c shows that most of the UTS data was plotted as a linear line except the lowest UTS data point. Again, the SEM images showed that the failure of this test bar was caused by a large double oxide film defect (see Figure 4.84). Therefore a better linear fit can be obtained if the Weibull distribution is divided with two trend-lines by the different failure mechanism as shown in Figure 4.97. The new trend-line shows that Weibull modulus was increased to 14.7, which was the same level of the low oxide film castings, after the test bar with the low UTS was taken out, and the R value also increased to 0.98.

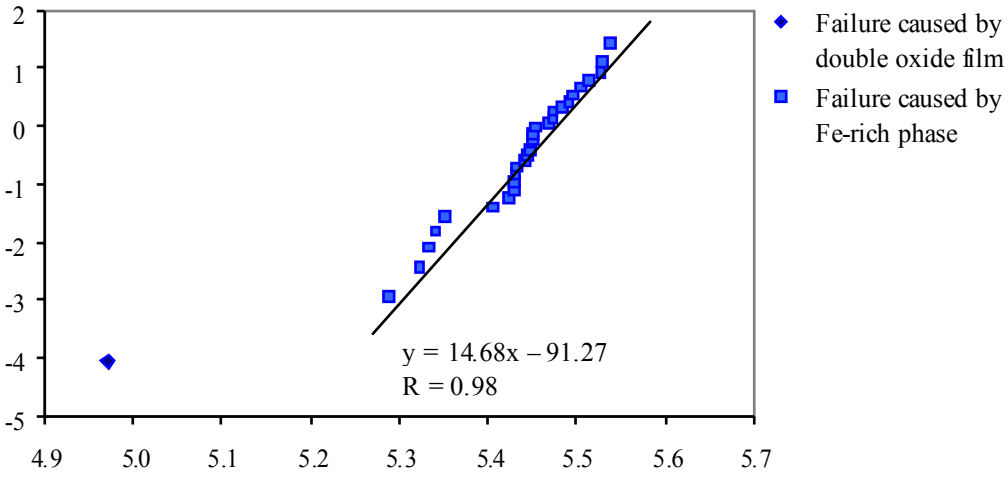


Figure 4.97 The graph showing the new Weibull plots of the UTS data of the high oxide film and low shrinkage castings considering two different failure mechanisms

4.2.2.5 Casting microstructures

The microstructure of the high oxide film and low shrinkage castings obtained from the cross sections of the heat-treated test bar have been shown in Figure 4.98. It can be noticed that the increase in the Fe content (to 1.1 wt% Fe) in cast aluminium alloys directly resulted in an increase in the size of β-Al_5FeSi phase, the needle-like platelet, compared to the other low Fe content castings (see Figures 4.38 and 4.42). Figures 4.99a to 4.99d show microstructures obtained from the cross sections of heat-treated test bars of the 4 types of castings. Apart from Fe-rich phases, the main defect observed in this experiment was microporosity as found in the other low hydrogen casting (Figures 4.43 and 4.76). Figure 4.100 obtained from the cross sections of the runner bars of the high oxide film and high shrinkage casting showed that the microporosity was located in the interdendritic region. The micrograph also showed an interaction between porosity and Fe-rich phase because Fe-rich phases were found at the edges of pores.

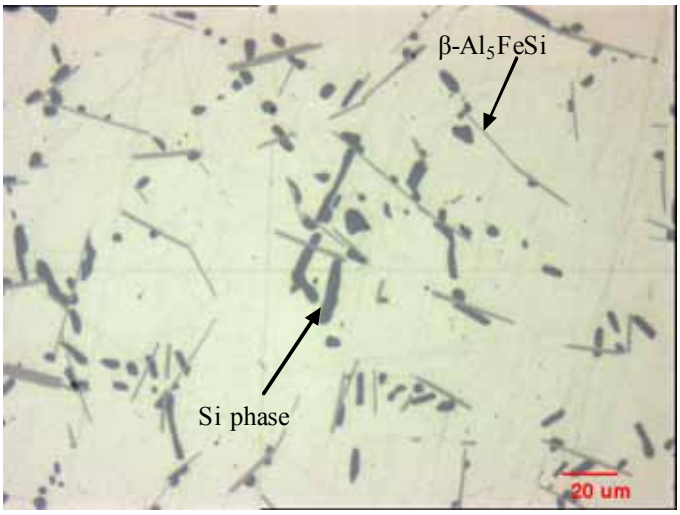
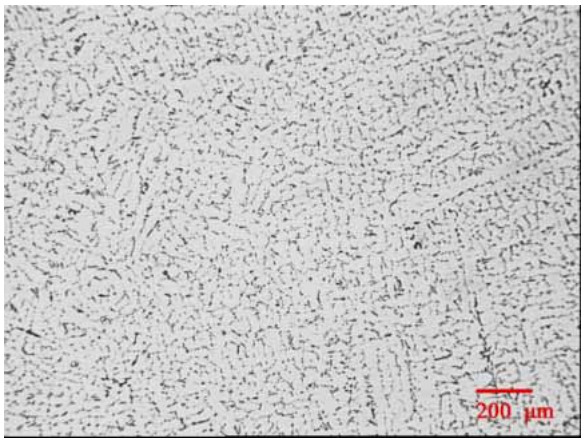
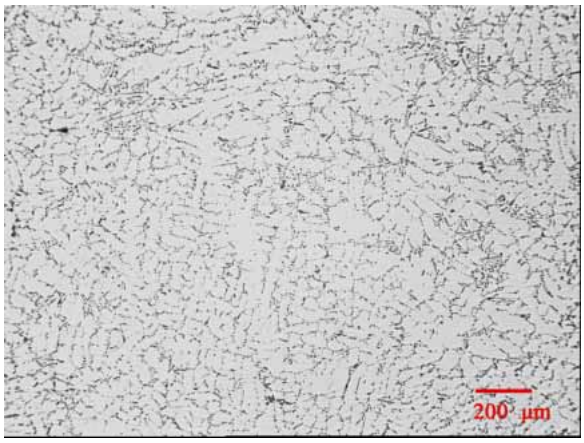


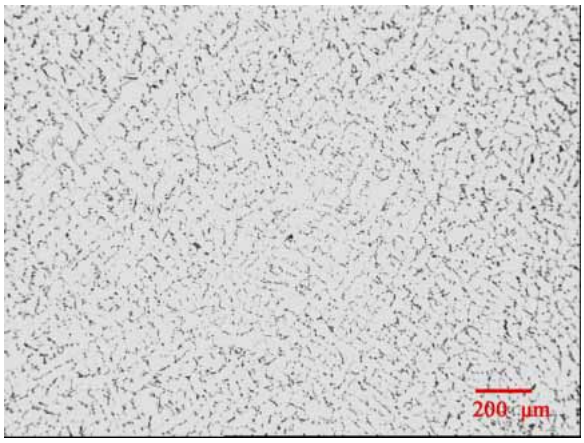
Figure 4.98 Optical micrograph of cross section of heat-treated test bars obtained from high oxide film and low shrinkage combination showing microstructure of the casting.



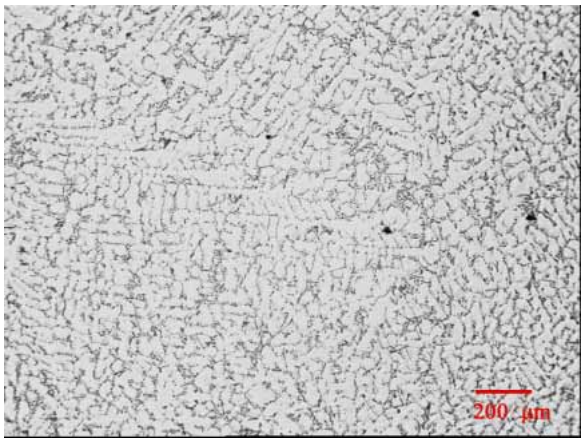
(a) low oxide film and low shrinkage



(b) low oxide film and high shrinkage



(c) high oxide film and low shrinkage



(d) high oxide film and high shrinkage

Figure 4.99 Optical micrograph showing microstructures of the castings for 4 experimental combinations.

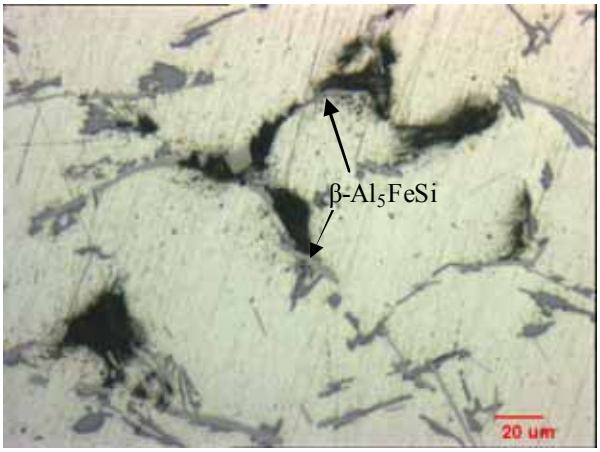


Figure 4.100 Optical micrograph showing microporosity in the castings associated with Fe-rich phases obtained from high oxide film and high shrinkage combination.

4.2.2.6 Image analysis

The runner bars of each combination of castings were examined by optical microscopy and subjected to image analysis. The results of porosity area, number of pores and pore size measurements obtained from image analysis are shown in Table 4.27. These show that the low oxide film and high shrinkage castings had the lowest porosity (porosity area of about 0.3 %, number of pores of about 1200 pores/cm^2 and mean size of pore of about 250 μm^2). Tables 4.28, 4.29 and 4.30 show the Yate's algorithm calculation for the porosity area, number of pore and pore size results respectively. Pareto diagrams illustrating the relative effects of oxide films, shrinkage and their interactions are shown in Figures 4.101a, 4.101b and 4.101c. The Pareto diagrams showed that oxide film (column A) had an effect on the number of pores of about 950 pore/cm^2, or about an 80% increase, while the effect on porosity area was 0.2% or about a 70% increase. Increasing oxide film content in the castings influenced the presence of porosity by increasing the number of pores, and hence the pore area. The shrinkage introduced in the experiment appeared to have no significant effect on the presence of porosity in this experiment. However, the results suggested an effect due to an interaction between oxide film and shrinkage (column AB) on the pore size as was obtained from the previous

experiment (see Figure 4.80c). Their interaction increased the pore size by about 10% or 30 μm^2.

Table 4.27 Image analysis results obtained from 4 experimental combinations.

Combination	Porosity area (%)	Number of pore per cm^2	Mean pore size (μm^2)
low oxide film, low shrinkage	0.30	1193	255
low oxide film, high shrinkage	0.28	1102	257
high oxide film, low shrinkage	0.54	2003	268
high oxide film, high shrinkage	0.47	2202	213

Table 4.28 The effect of oxide film, shrinkage and their interactions on porosity area using Yate's algorithm.

	total	1	2	estimate of effect
(1)	0.30	0.84	1.59	0.80
effect of oxide film: A	0.54	0.75	0.43	0.22
effect of shrinkage: B	0.28	0.24	-0.09	-0.05
AB	0.47	0.19	-0.05	-0.03

Table 4.29 The effect of oxide film, shrinkage and their interactions on number of pore per cm^2 using Yate's algorithm.

	total	1	2	estimate of effect
(1)	1192	3195	6499	3249.50
effect of oxide film: A	2003	3304	1911	955.50
effect of shrinkage: B	1102	811	109	54.50
AB	2202	1100	289	144.50

Table 4.30 The effect of oxide film, shrinkage and their interactions to size of pore using Yate's algorithm.

	total	1	2	estimate of effect
(1)	255	523	993	496.50
effect of oxide film: A	268	470	-31	-15.50
effect of shrinkage: B	257	13	-53	-26.50
AB	213	-44	-57	-28.50

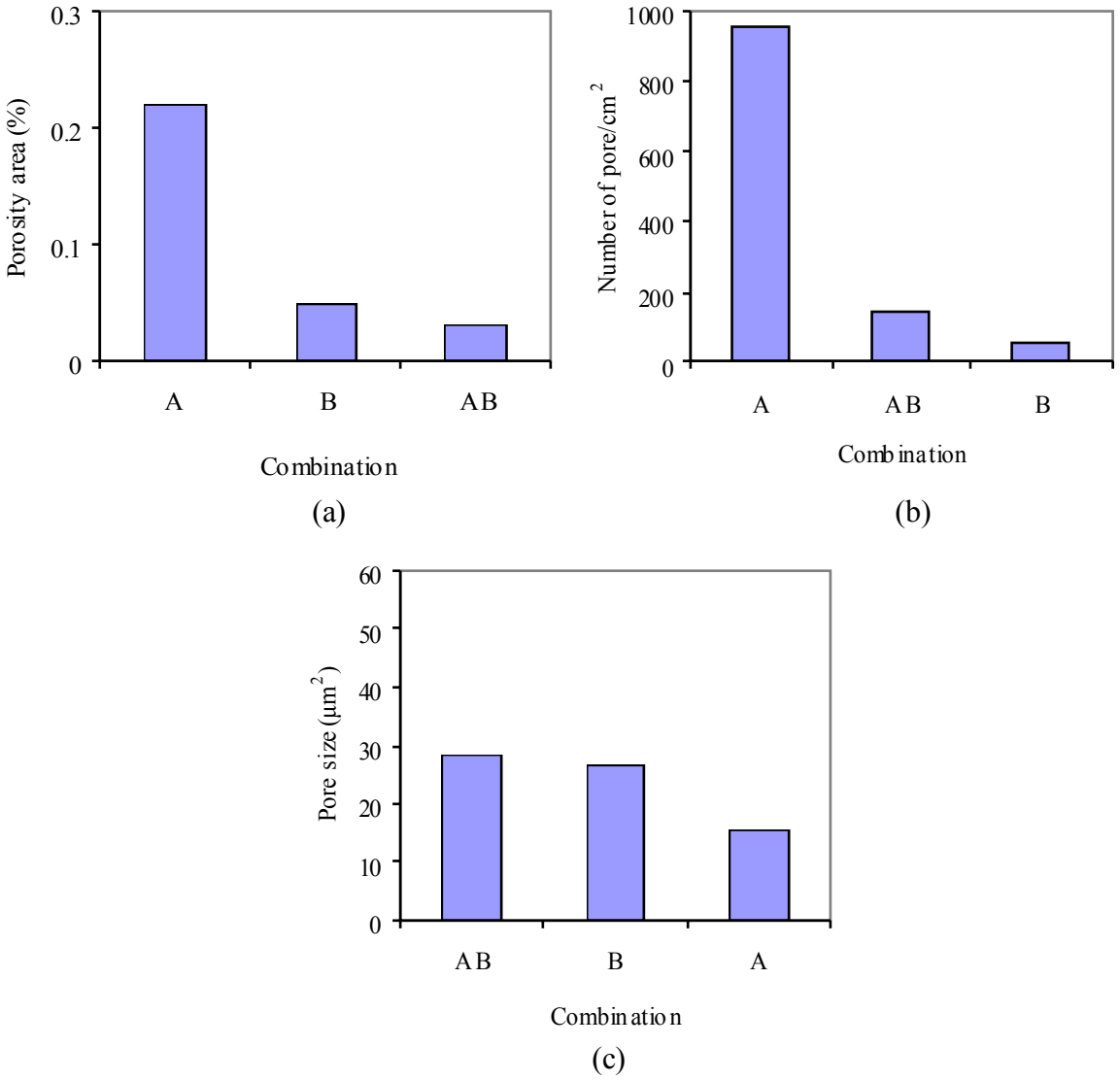


Figure 4.101 Pareto diagrams showing the effects of two defects and their interrelationships on (a) the porosity area (b) the number of pore per cm^2 and (c) the pore size (A = effect of oxide film, B = effect of shrinkage).

4.3 Effects of entrained oxide films on the formation of hydrogen porosity in high purity aluminium and a high purity Al-Si alloy.

This experiment was carried out to investigate the effects produced by entrained oxide film defects on the formation of porosity in high purity aluminium and a high purity Al-7Si alloy containing dissolved hydrogen. As shown in Table 3.5, the high purity aluminium and high purity Al-7Si alloys used contained about 0.01 wt% Fe. Two types of castings were made with two different oxide film contents obtained by using a ceramic filter.

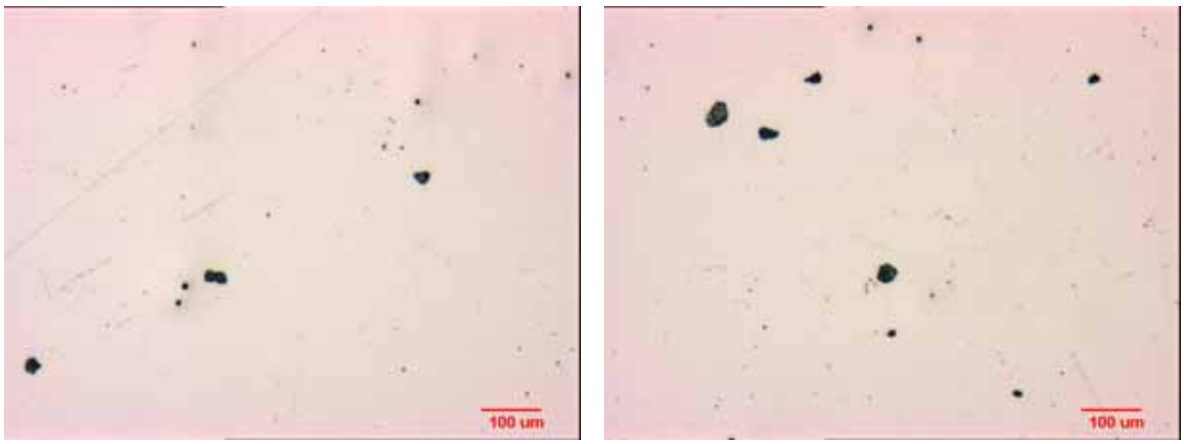
4.3.1 Effect of entrained oxide films on the formation of hydrogen porosity in high purity aluminium

4.3.1.1 Image analysis

Figures 4.102a and 4.102b show micrographs obtained from the cross section of runner bars of the low oxide film and high oxide film castings respectively. Microporosity was observed in both castings. Although the hydrogen content in both castings was high (0.4 ml/100g metal), the images show that the size of pore was smaller than that found in the high hydrogen content castings in the other experiment (see Figures 4.43e to 4.43h).

Table 4.31 shows measurements of porosity area, number of pores per cm^2 and pore size of the low and high oxide film castings obtained by image analysis. It can be seen that the low oxide film casting had the lowest porosity area of 0.29% while the high oxide film casting had a porosity area of 0.36%. The porosity area results of both castings were very low compared to the high hydrogen content casting in the previous experiment to examine the interactions between Fe-rich phase, hydrogen porosity and oxide films (Table 4.9) where the area of porosity was about 3.0% (and where the hydrogen content was 0.45 ml/100g). This suggested that, beside hydrogen content, another factor was required for the formation of porosity in castings.

The results showed that entrained oxide films directly influenced the presence of porosity by increasing the porosity area and number of pores in the castings. For example, increasing oxide film content resulted in an increase in porosity area of 0.07 %, (a 20% increase), and an increase in the number of pores by about 300 pores per cm^2 (a 40% increase). However the increase in oxide film appeared to decrease the average pore size from 364 to 314 μm^2. This suggested that porosity in the high oxide film casting formed with a smaller size, but in greater numbers and had a higher number density of pores than in the case of the low oxide film casting.



(a) (b)

Figure 4.102 Optical micrograph showing microstructures obtained from (a) the low oxide films casting and (b) the high oxide films casting.

Table 4.31 Image analysis results obtained from the high purity aluminium castings.

Oxide film content	Pore area (%)	Number of pore per cm^2	Average pore size (μm^2)
Low	0.29	802	364
High	0.36	1110	314

4.3.1.2 Casting microstructures

Figures 4.103 to 4.106 show SEM images of microporosity obtained from the runner bar of the low and high oxide film castings, and EDX analysis of pores, respectively. It can be noticed that the internal surface of more than 95% of observed pores in this experiment (about 20 pores for each casting were examined) contained oxygen, suggesting that oxide films played a role in the formation of porosity.

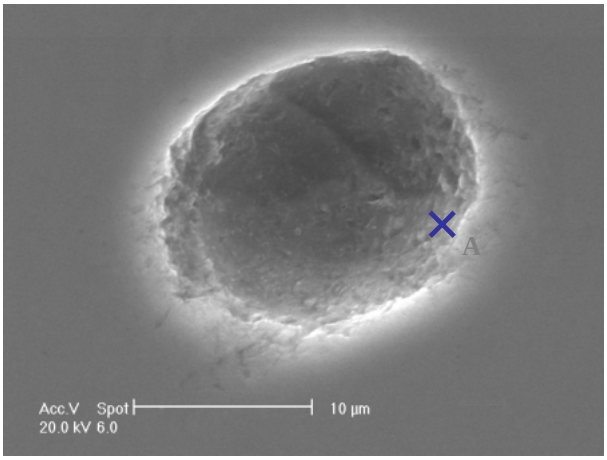


Figure 4.103 The scanning electron micrographs obtained the low oxide film casting showing microporosity.

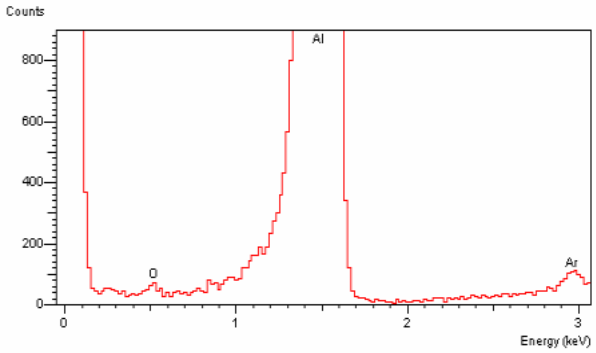


Figure 4.104 The EDX analysis result obtained from point A in Figure 4.103.

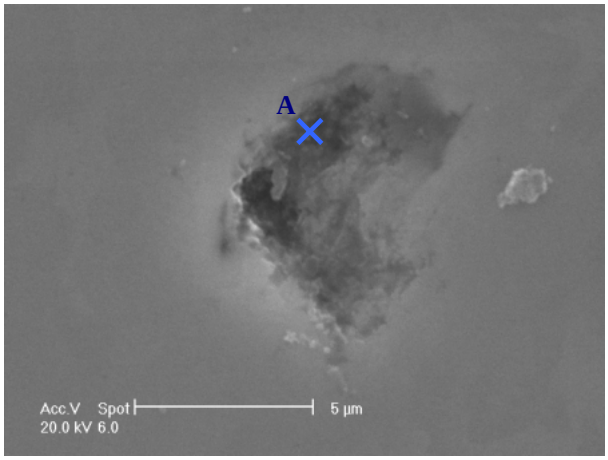


Figure 4.105 The scanning electron micrographs obtained from the runner of the high oxide film casting showing microporosity contained the oxide film.

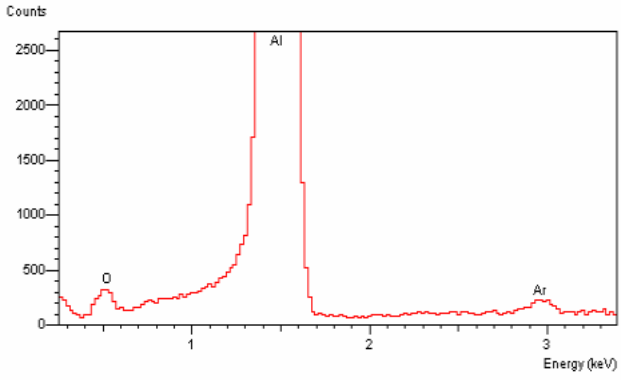
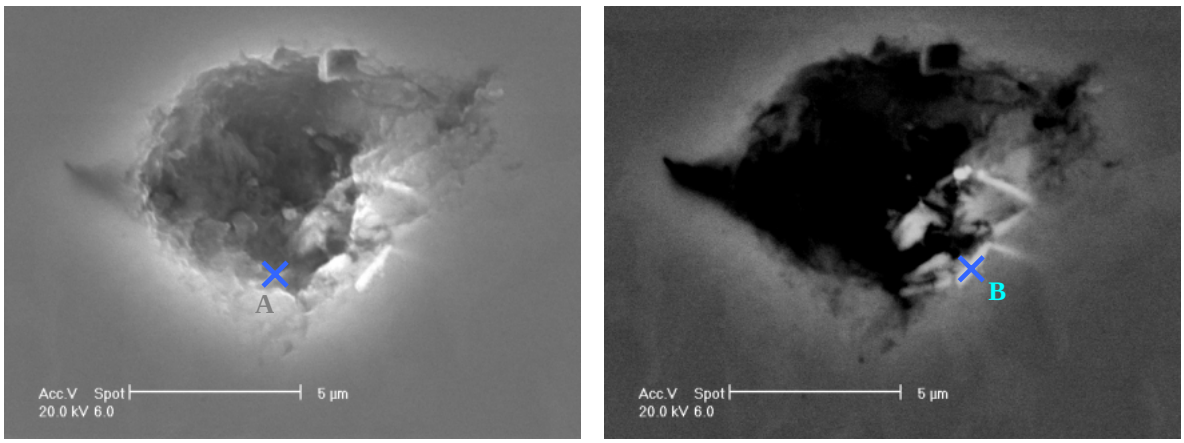


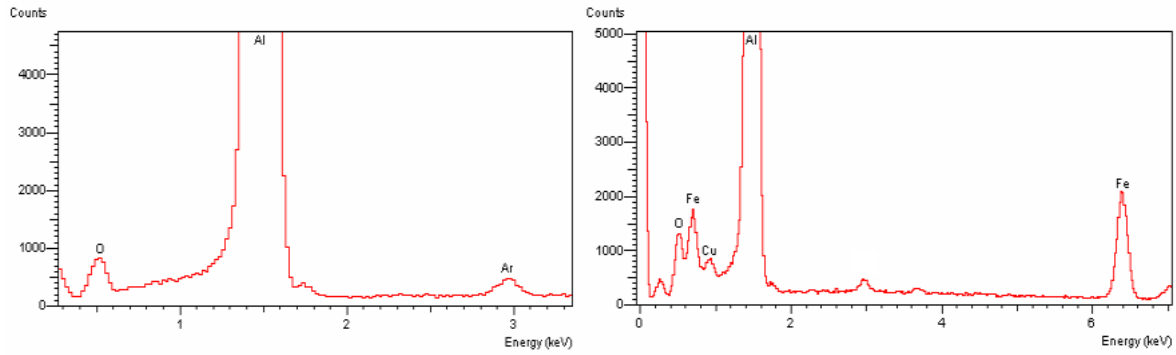
Figure 4.106 The EDX analysis result obtained from point A in Figure 4.105.

Figure 4.107 shows another SEM image of porosity obtained from the high oxide film casting, with the EDX analysis shown in Figure 4.108a. Oxide film was detected at the internal surface of the pore, but the EDX analysis result in Figure 4.108b also showed the presence of Fe intermetallic phases at the edge of the pore. This suggested an interaction between oxide film and Fe-rich phase that influenced the porosity formation mechanism in some way.



(a) (b)

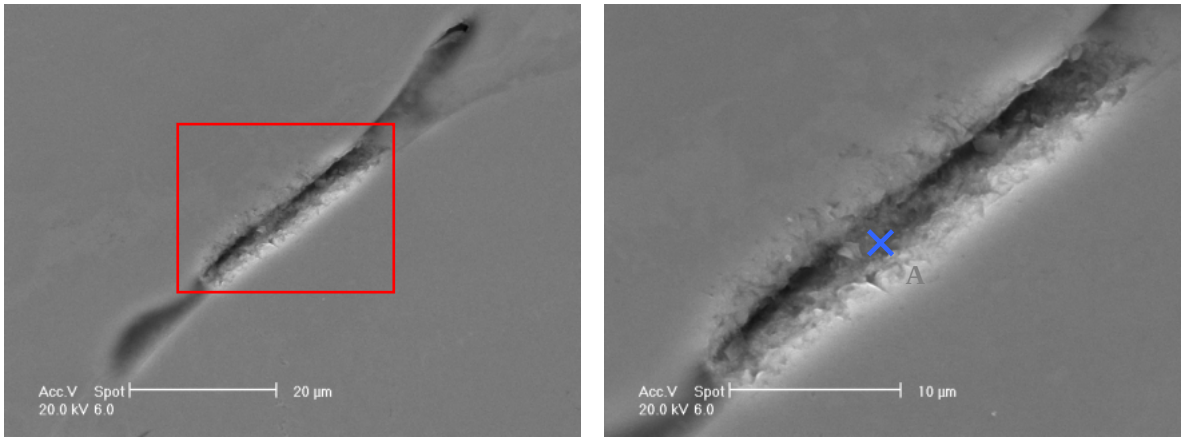
Figure 4.107 The scanning electron micrographs obtained from the high oxide film casting showing (a) the Fe-rich phase associated with porosity in the casting (b) the back-scattered image of Figure 4.107a.



(a) (b)

Figure 4.108 The EDX analysis results obtained from points A and B in Figure 4.107a and 4.107b.

Figures 4.109a and 4.109b show an oxide-related pore obtained from the low oxide film casting, for which the EDX analysis result has been shown in Figure 4.110. The SEM images in Figures 4.111a and 4.111b, and the EDX analysis results in Figures 4.112a and 4.112b show other oxide films observed in the low oxide film casting. These results suggested that entrained oxide films were to be found in every casting. Although a filter was used, the presence of entrained oxide films was still unavoidable.



(a) (b)

Figure 4.109 The scanning electron micrographs obtained from the low oxide film casting showing (a) double oxide films defect (b) the higher magnification of selected area in figure 4.109a.

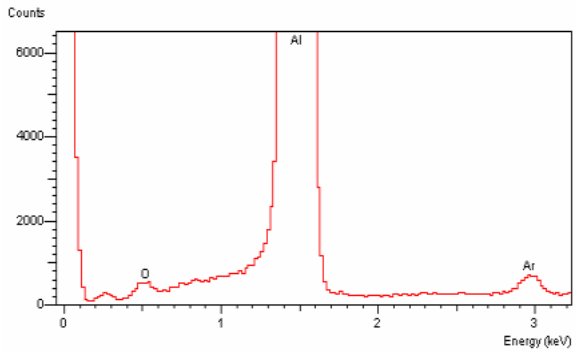
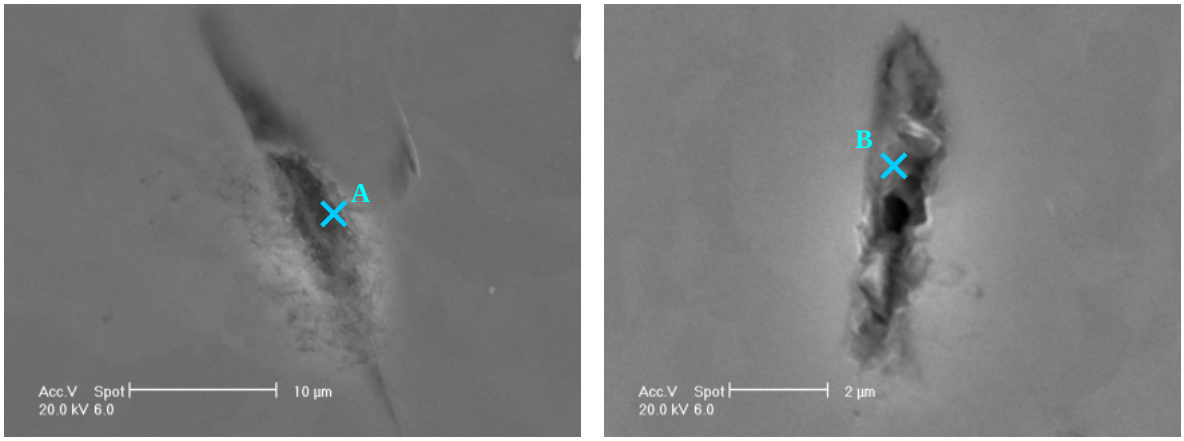
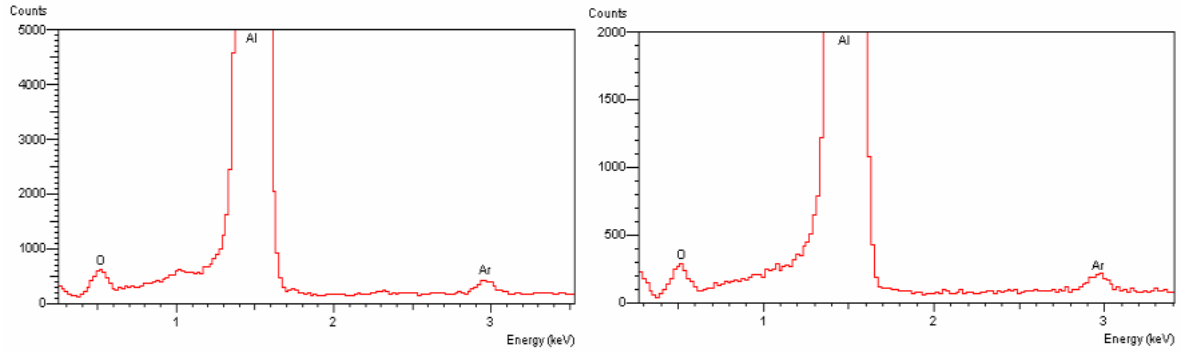


Figure 4.110 The EDX analysis result obtained from point A in Figure 4.109b.



(a) (b)

Figure 4.111 The scanning electron micrographs obtained the low oxide film casting showing oxide film defects in the castings.



(a) (b)

Figure 4.112 The EDX analysis results obtained from points A and B in Figure 4.111a and 4.111b.

Figures 4.113 and 4.114a to 4.114e show an extensive oxide film, with a millimetre in length, obtained from the high oxide film casting with associated EDX analysis results shown in Figures 4.115a to 4.115e. This kind of defect was occasionally observed in the unfiltered castings (as shown in Figures 4.50, 4.51, 4.53 and 4.54). The presence of a large oxide film defect suggested that greater surface turbulence was produced and, of course, resulted in a greater number of oxide films in the casting.

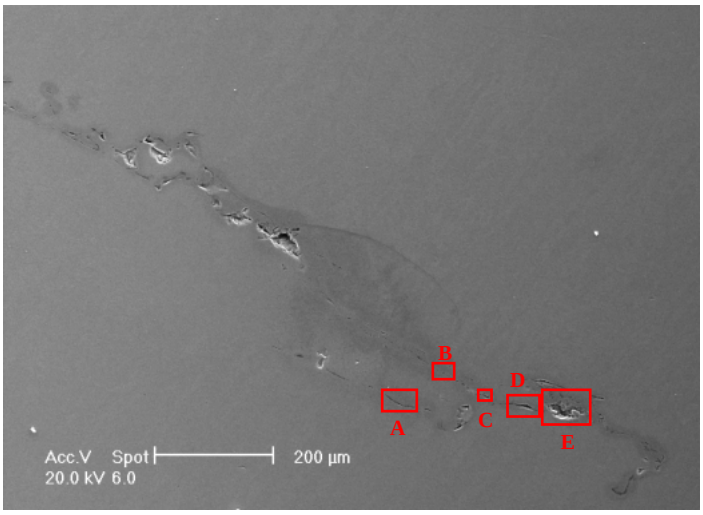
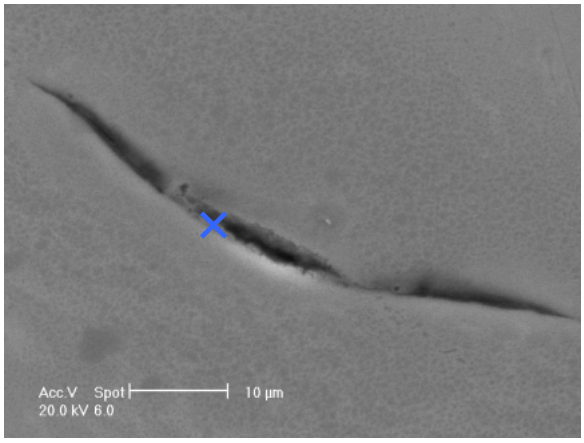
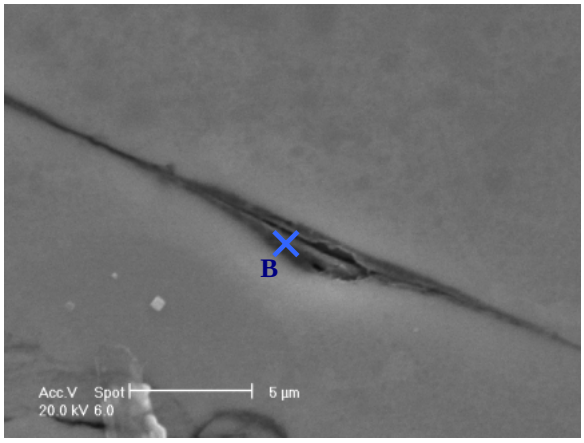


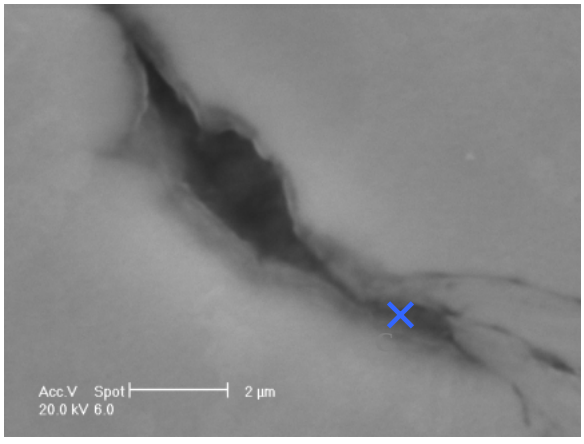
Figure 4.113 The scanning electron micrographs obtained from the high oxide film casting showing the extensive double oxide films defects.



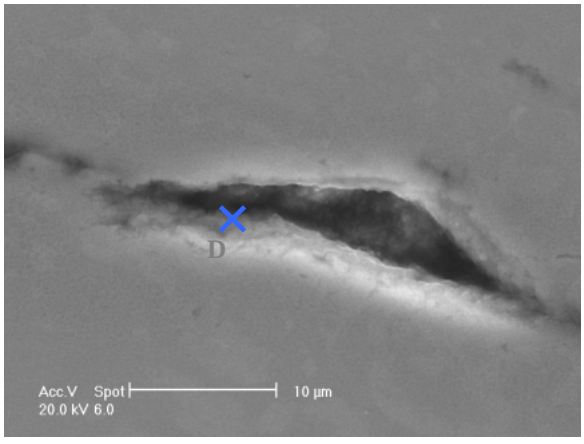
(a)



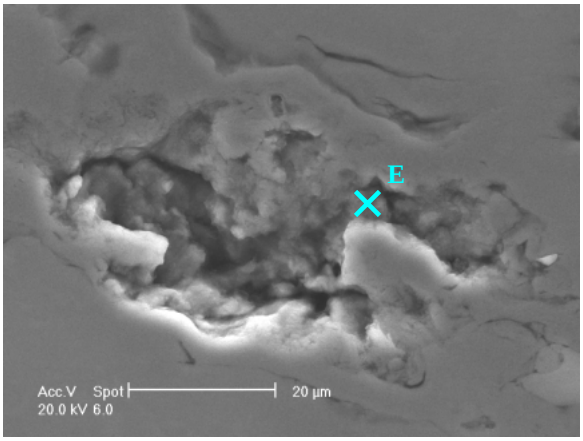
(b)



(c)

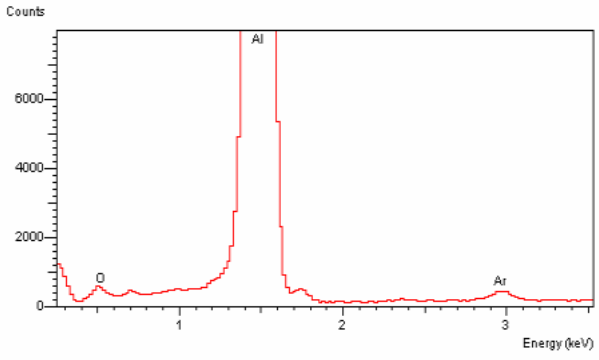


(d)

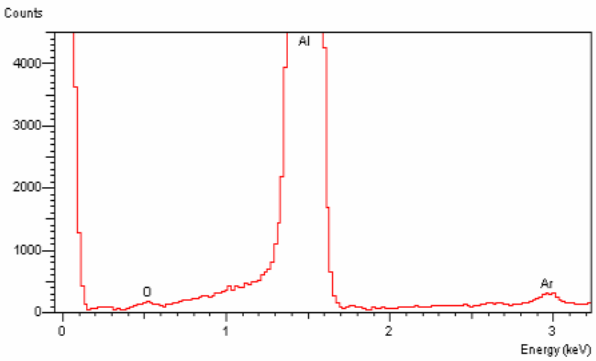


(e)

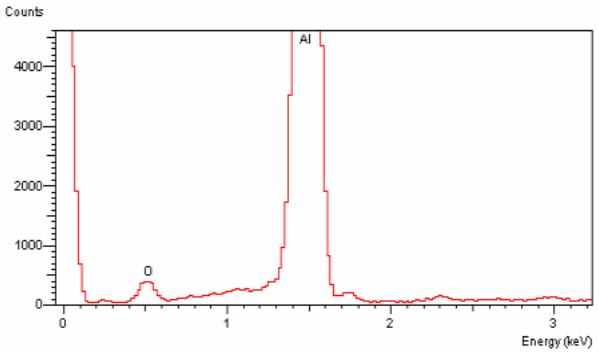
Figure 4.114 The higher magnification of areas A to E obtained from Figure 4.113.



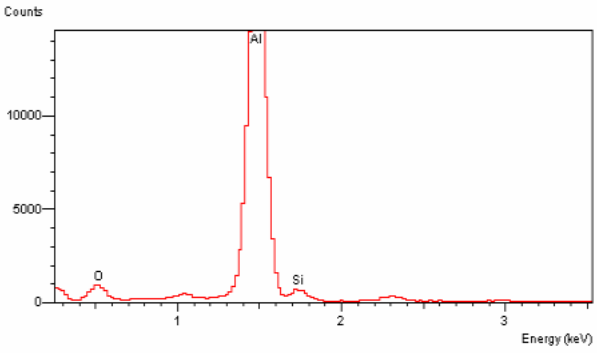
(a)



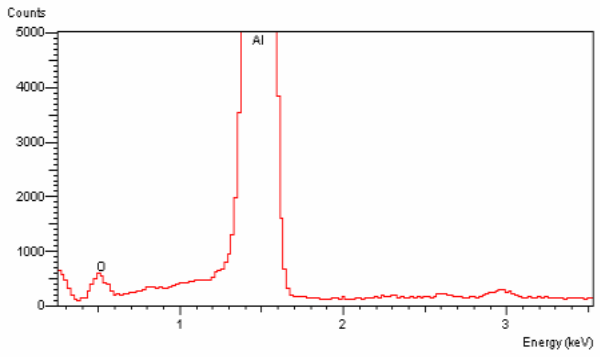
(b)



(c)



(d)



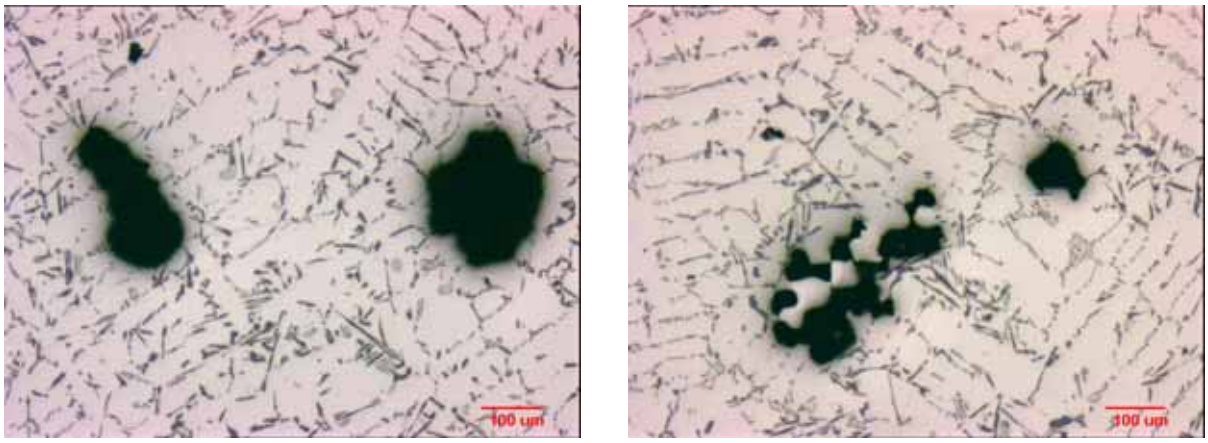
(e)

Figure 4.115 The EDX analysis results obtained from points A and E in Figures 4.114a to 4.114E.

4.3.2 Effects of entrained oxide films on the formation of hydrogen porosity in a high purity Al-Si alloy

4.3.2.1 Image analysis

Figures 4.116a and 4.116b show micrographs obtained from the low oxide film and high oxide film castings respectively. The main defect observed was gas porosity, as expected due to the high hydrogen content of the casting (0.38 ml/100 g metal). The images show that gas porosity with a rounded shape was often observed in the low oxide film casting while the porosity observed in the high oxide film casting was smaller and some had an irregular shape.



(a) (b)

Figure 4.116 Optical micrograph showing porosity defects obtained from (a) the low oxide film casting and (b) the high oxide film casting.

Table 4.32 shows image analysis results of porosity area, number of pore per cm^2 and pore size measurements obtained from the low and high oxide film casting. The low oxide film casting had a greater pore area and pore size, about 3.67 % and 1996 μm^2 respectively, while the number of pores per cm^2 was 1878 pores. The results show that the presence of porosity in the casting was at the same level, compared to the high hydrogen content casting (0.45 ml/100g metal) in the previous experiment that examined the effect of Fe-rich phase, hydrogen porosity and oxide films where area of porosity was about 3.0% (see porosity area in Table 4.9). However the area of porosity of the casting in this experiment was significantly greater than in the case of the high purity aluminium alloy (see Table 4.31). This suggested that the alloying element influenced the porosity formation in the casting.

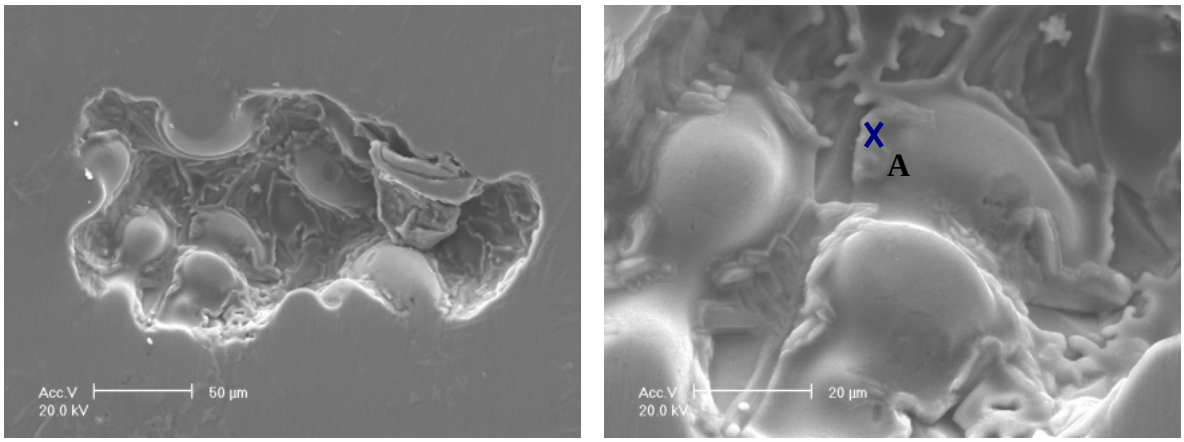
Oxide film defects appeared to affect the formation of porosity since the increase in oxide film content resulted in an increase in the number of pores of about 1200 pores per cm^2, (a 60% increase), while a reduction in the pore area and the pore size of about 0.6% and 1000 μm^2 respectively was observed. This suggested that the high oxide film casting had a higher number density of pores than the low oxide film casting.

Table 4.32 Image analysis of the high purity Al-7Si alloy castings.

Oxide film content	Pore area (%)	Number of pore per cm^2	Average pore size (μm^2)
Low	3.67	1878	1996
High	3.09	3060	1030

4.3.2.2 Casting microstructures

Figures 4.117a and 4.117b show SEM images of gas porosity obtained from the low oxide film castings and Figure 4.118 shows the EDX analysis result. Figures 4.119a and 1.119b show an example of porosity obtained from the high oxide film castings and associated EDX analysis results have been shown in Figures 4.120a and 4.120b. The images suggested an interaction between oxide film and gas porosity since oxide was detected at the internal surface of more than 95% of examined pores (about 20 pores from each casting). Comparing the pore size with the high purity aluminium experiment (see Figures 4.103 and 4.105), the porosity produced in this experiment was larger. This shows that Si, as an alloying element, influenced the formation of porosity in the castings.



(a) (b)

Figure 4.117 The scanning electron micrographs of cross section of the runner obtained from the low oxide film casting showing (a) gas porosity in the casting (b) the higher magnification of the porosity from figure 4.117a.

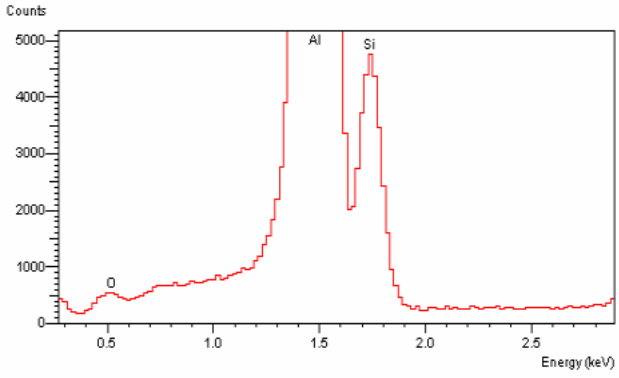
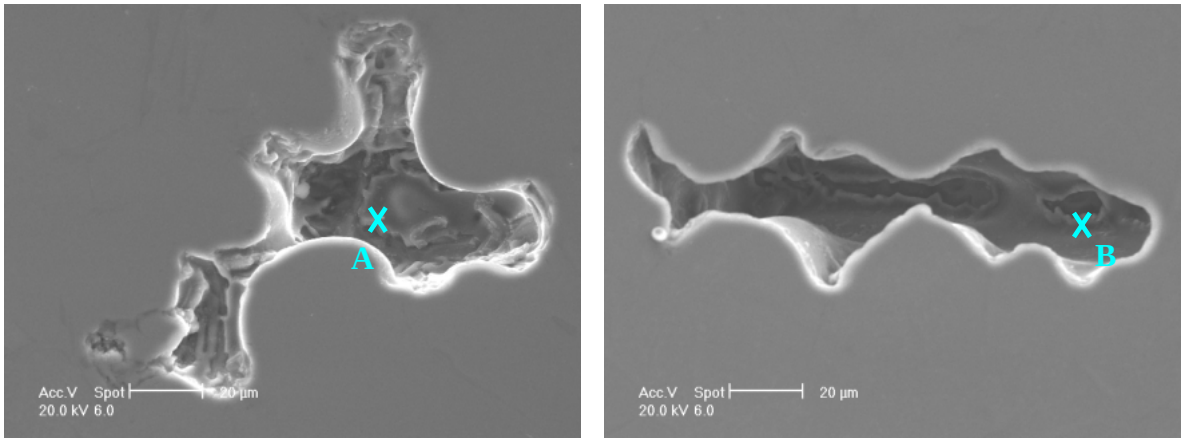
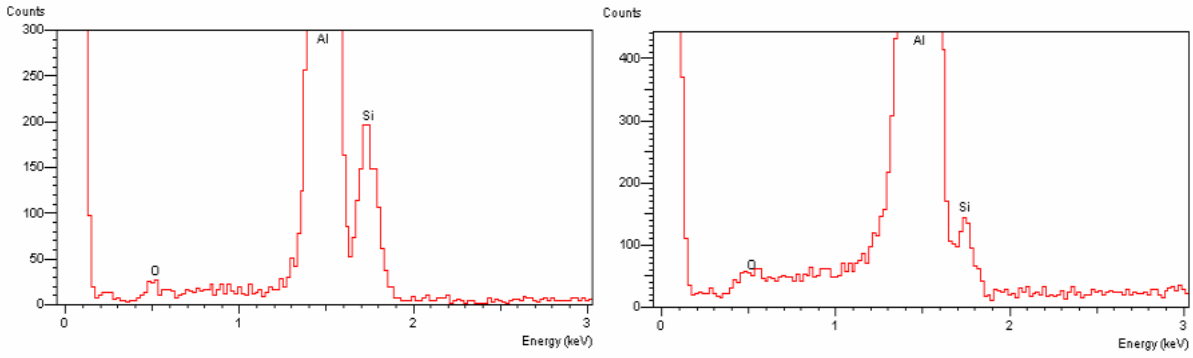


Figure 4.118 The EDX analysis results obtained from point A in figure 4.117b



(a) (b)

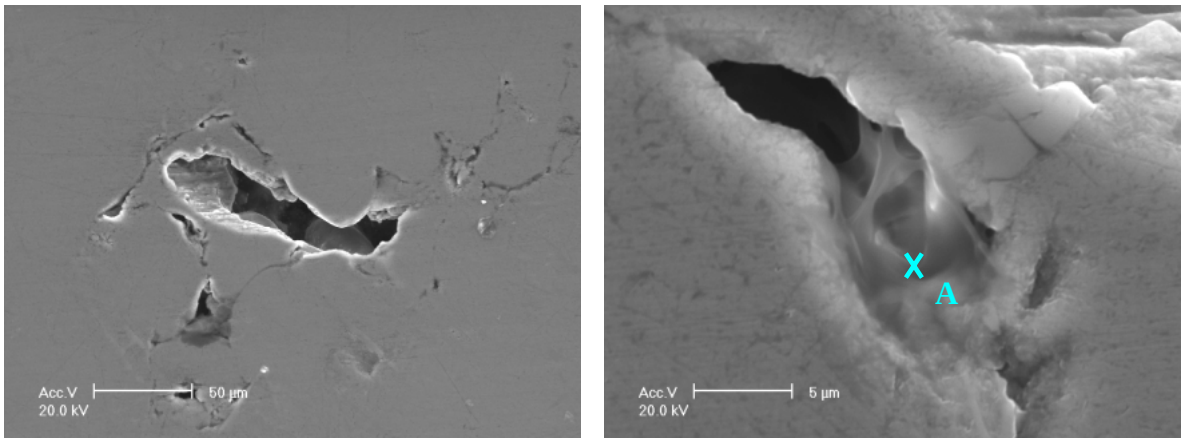
Figure 4.119 The scanning electron micrographs of cross section of the runner bar obtained from the high oxide film casting showing porosity in the castings.



(a) (b)

Figure 4.120 The EDX analysis results obtained from points A and B in figure 4.119a and 4.119b.

Figures 4.121a, 4.121b, and 4.122 show SEM images of a large oxide film defect obtained from the runner bar of the high oxide film casting and the EDX analysis result respectively. Figures 4.123a and 4.123b show another oxide film defect found in the high oxide film casting and the associated EDX analysis result has been shown in Figure 4.124. The large oxide films defect occurred by the folding action of a great surface turbulence. These suggest that surface turbulence produced in the high oxide film casting was greater than the low oxide film castings and greater number of oxide film defects were therefore introduced in the high oxide film casting.



(a) (b)

Figure 4.121 The scanning electron micrographs obtained from the high oxide film casting showing a) double oxide films defects in the casting and b) the higher magnification of double oxide films from figure 4.121a.

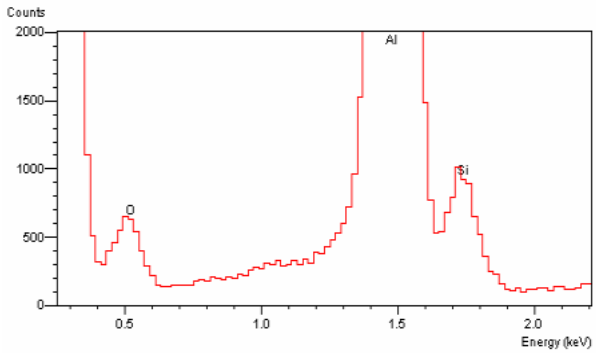
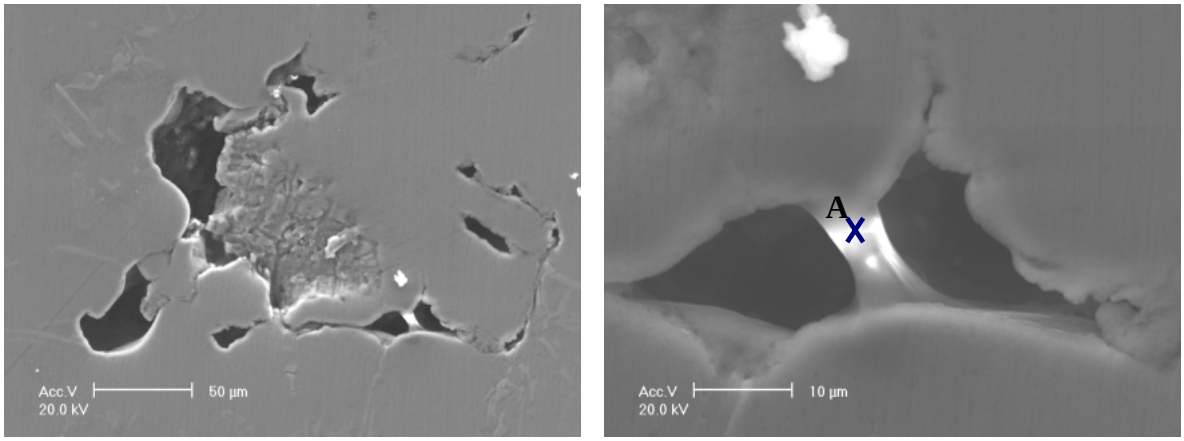


Figure 4.122 The EDX analysis result obtained from point A in figure 4.121b.



(a) (b)

Figure 4.123 The scanning electron micrographs obtained from the high oxide film casting showing (a) the other double oxide films defects in the casting (b) the higher magnification of oxide films from figure 4.123a.

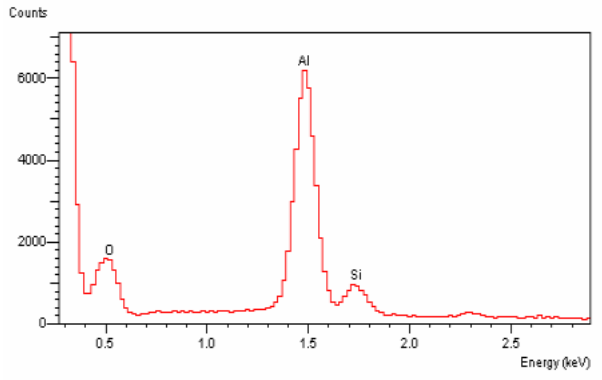


Figure 4.124 The EDX analysis result obtained from point A in figure 4.123b.

In summary, the results from image analysis and SEM images suggested an interaction between oxide film and porosity in that the porosity was associated with entrained oxide films, since oxides were detected at the internal surface of the pores. Increasing oxide film content influenced porosity formation by increasing pore initiators and, thus, resulted in an increase in the number of pores in the casting. Adding Si to the alloy also affected the presence of porosity by greatly increasing the area of porosity. This suggests that Si had an effect on the formation of porosity in some way.

4.4 Effect of entrained oxide films on the formation of shrinkage porosity in Al-Si-Mg alloy.

This experiment was carried out in order to investigate any interrelationship between oxide films and shrinkage porosity in Al castings. Since the results in section 4.2 showed that shrinkage porosity had not been produced to the extent expected in the test bar mould, a plate mould was used in this experiment. The oxide film content in each casting was varied by differences in the amount of surface turbulence produced during the filling process. The density and the image analysis results obtained from each section of the castings were used to examine the role of entrained oxide films on the formation and distribution of shrinkage porosity.

4.4.1 Density measurement results

The plate mould was cast with three different running systems; 1) a filtered mould, 2) an unfiltered and unstoppered mould, and 3) an unfiltered and stoppered mould. As shown in the x-ray images (see Figures 3.11, 3.12 and 3.13), the flow of liquid metal in each mould produced a different entrained oxide film content, from low to high, in the order of the filtered mould, the unfiltered and unstoppered mould, and the unfiltered and stoppered mould, (in which the metal was stirred before casting also). Therefore the three castings were defined in this experiment as a low oxide film casting, a medium oxide film casting and a high oxide film casting.

The plates obtained from all oxide film content castings were cut into 32 sections (see Figure 3.14) and their density measured by Archimedes' method. The density measurement technique used in this experiment was determined to have an accuracy of ± 0.005 kg/m^3. The volume fraction of porosity was estimated by comparing the measured density, with the lower the density the more porosity in the casting. Tables 4.33, 4.34 and 4.35 show the density results from the 32 sections and the mean density of each cast plate for the low oxide film, the medium oxide film and high oxide film castings respectively. The results show that the low oxide film casting had the highest mean density (of 2.67 kg/m^3) while the high oxide film casting had the lowest mean density (of

2.62 kg/m^3). The mean density of the medium oxide film casting was of an intermediate value, 2.65 kg/m^3. This shows that the high oxide film castings contained the greatest porosity and the low oxide film casting had the lowest internal porosity.

Table 4.33 Measured density results of 32 sections obtained from the low oxide film casting (the filtered casting).

Part	Mass (g.) weighed in air	Mass (g.) weighed in air	Density (kg/m^3)
1	25.248	15.870	2.692
2	25.302	15.872	2.683
3	24.214	15.184	2.682
4	24.986	15.666	2.681
5	24.479	15.354	2.683
6	25.113	15.747	2.681
7	24.735	15.529	2.687
8	26.147	16.441	2.694
9	24.792	15.552	2.683
10	24.450	15.267	2.663
11	23.477	14.606	2.646
12	23.219	14.200	2.574
13	22.860	14.036	2.591
14	23.063	14.376	2.655
15	23.762	14.852	2.667
16	25.181	15.803	2.685
17	25.446	15.961	2.683
18	24.752	15.450	2.661
19	24.540	15.218	2.632
20	24.099	14.733	2.573
21	23.231	14.298	2.601
22	23.972	14.930	2.651
23	24.655	15.405	2.665
24	25.764	16.165	2.684
25	26.436	16.613	2.691
26	26.224	16.449	2.683
27	24.956	15.637	2.678
28	25.732	16.136	2.682
29	25.425	15.945	2.682
30	25.113	15.746	2.681
31	26.543	16.658	2.685
32	26.805	16.852	2.693
Mean density			2.665

Table 4.34 Measured density results of 32 sections obtained from the medium oxide film casting (the unfiltered and unstoppered casting).

Part	Mass (g.) weighed in air	Mass (g.) weighed in air	Density (kg/m^3)
1	25.588	15.932	2.650
2	24.123	15.110	2.676
3	24.379	15.263	2.674
4	24.109	15.110	2.679
5	24.263	15.212	2.681
6	24.606	15.428	2.681
7	24.513	15.380	2.684
8	23.994	14.372	2.494
9	25.583	16.026	2.677
10	22.579	14.097	2.662
11	22.362	13.837	2.623
12	23.675	14.485	2.576
13	23.011	14.164	2.601
14	22.682	14.120	2.649
15	24.152	15.087	2.664
16	25.914	16.260	2.684
17	27.008	16.917	2.676
18	23.186	14.470	2.660
19	24.370	15.042	2.613
20	22.411	13.644	2.556
21	23.223	14.142	2.557
22	23.794	14.669	2.608
23	25.905	16.180	2.664
24	25.271	15.857	2.684
25	26.429	16.589	2.686
26	24.894	15.600	2.679
27	24.915	15.604	2.676
28	25.482	15.958	2.676
29	26.265	16.447	2.675
30	24.899	15.600	2.678
31	26.430	16.576	2.682
32	26.580	16.696	2.689
Mean density			2.650

Table 4.35 Measured density results of 32 sections obtained from the high oxide film casting (the unfiltered and stoppered casting).

Part	Mass (g.) weighed in air	Mass (g.) weighed in air	Density (kg/m^3)
1	25.637	15.913	2.636
2	24.191	15.027	2.640
3	24.877	15.454	2.640
4	25.157	15.617	2.637
5	25.437	15.792	2.637
6	25.119	15.601	2.639
7	25.466	15.834	2.644
8	25.298	15.741	2.647
9	26.189	16.254	2.636
10	25.402	15.653	2.606
11	24.726	15.136	2.578
12	24.098	14.698	2.564
13	24.765	15.205	2.590
14	24.403	15.023	2.602
15	24.320	15.038	2.620
16	25.879	16.095	2.645
17	26.142	16.216	2.634
18	24.963	15.330	2.591
19	25.790	15.532	2.514
20	24.193	14.633	2.531
21	25.219	15.461	2.584
22	23.805	14.648	2.600
23	24.247	14.986	2.618
24	25.584	15.903	2.643
25	26.414	16.424	2.644
26	26.112	16.163	2.625
27	26.594	16.414	2.612
28	26.467	16.395	2.628
29	25.611	15.890	2.635
30	25.951	16.107	2.636
31	26.512	16.482	2.643
32	26.658	16.602	2.651
Mean density			2.617

Figure 4.125 shows distributions of density data obtained from the 3 types of castings, which shows that the highest density was found in sections 1 to 10, 15 to 18, and sections 24 to 32. A significant decrease in the density of the castings occurred in 2 main areas, (i.e. sections 11 to 14 and section 19 to 22), the central area of the cast plates. As shown in the computer model image, (see Figure 3.10), the centre of the plate was a hot spot during solidification, i.e., the last zone to solidify and, therefore, the greatest shrinkage was expected to be produced in this area. The distribution diagram also shows that the low oxide film and the medium oxide film contained shrinkage porosity at much the same level, and was similarly distributed. In the high oxide film casting, the increase in oxide film and hydrogen content (to 0.3 ml/100g metal) resulted in a decrease in density of every section.

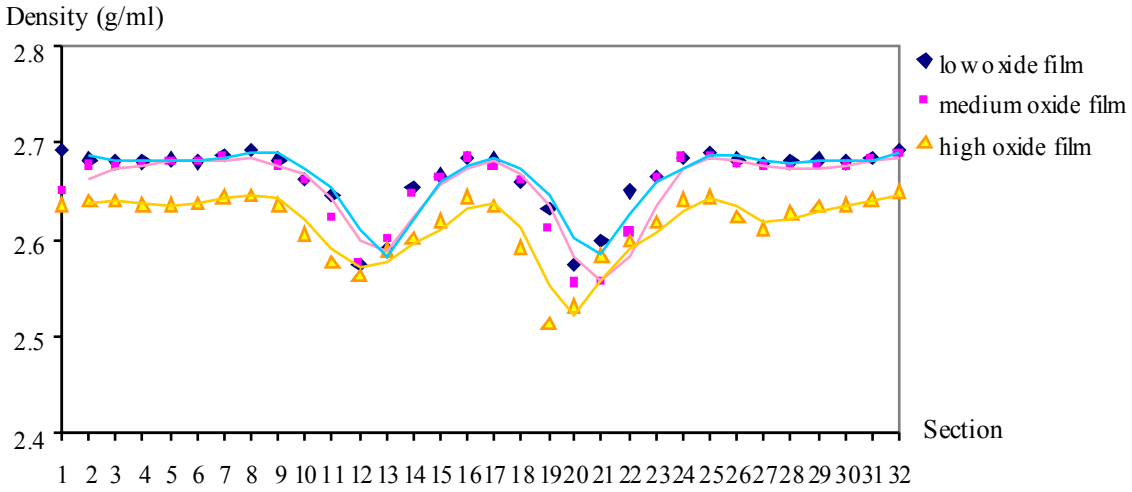


Figure 4.125 The distribution of density in 32 sections obtained from 3 oxide film content castings.

4.4.2 Casting microstructure

Figure 4.126 shows a macrograph of the 32 sections obtained from the low oxide film cast plate. The main defect observed was microporosity, as was expected considering the low hydrogen content of the casting (about 0.2 ml/100g metal). The porosity appeared to

be concentrated in the centre of the casting, suggesting that the porosity in the cast plate was mainly caused by shrinkage. Figure 4.127 shows a macrograph of the medium oxide film casting. Increasing surface turbulence during mould filling resulted in an increase in entrained oxide films and the image showed that several large oxide film defects were observed in the casting, for example, in sections 1 and 23. A large air bubble, which was trapped during solidification was seen in section 8, was also caused by the greater surface turbulence. The main defect observed in the medium oxide film casting was again microporosity, mostly located in the centre of the cast plate, as in the low oxide film casting. Figure 4.128 shows the macrograph of the high oxide film casting. Increasing oxide film content had a significant effect on the presence of porosity since numbers of porosity defects were clearly observed in every section of the casting. However, it is important to note that the higher hydrogen content (of about 0.3 ml/100g metal) in this casting would also influence the presence of porosity in the casting. The main porosity observed in the high oxide film casting was separately formed and well distributed, therefore, it seemed to be gas porosity. Shrinkage porosity, nonetheless, was also observed in the centre of the cast plate (higher magnification image would be shown later), but less in amount compared to the other castings.

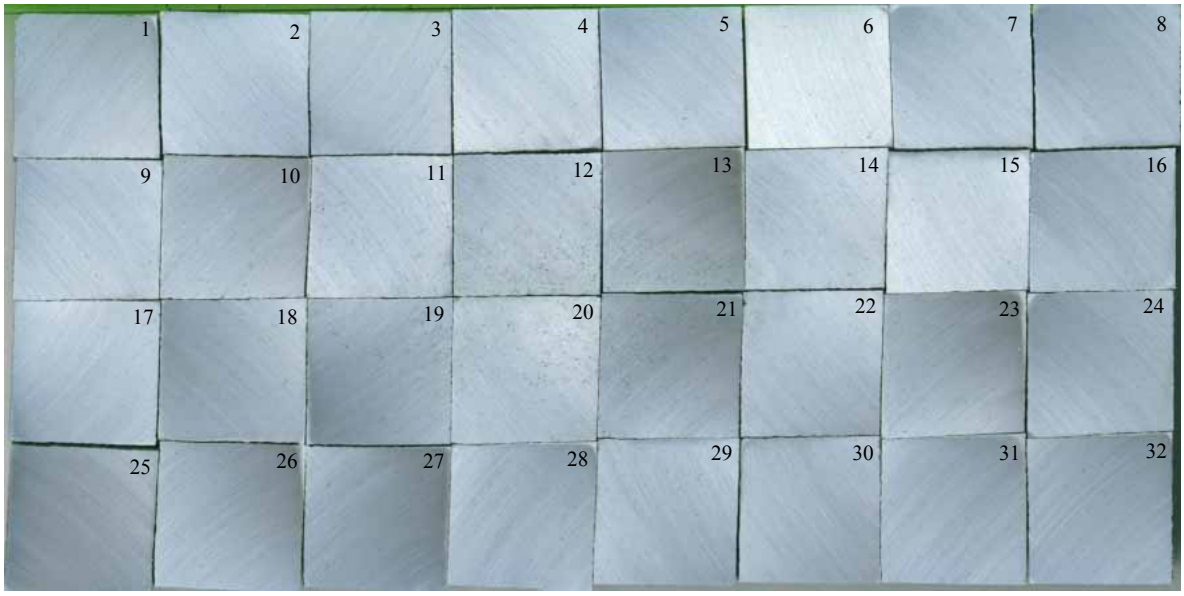


Figure 4.126 The macrograph showing the cross section of 32 sections of the low oxide film casting (filtered casting).

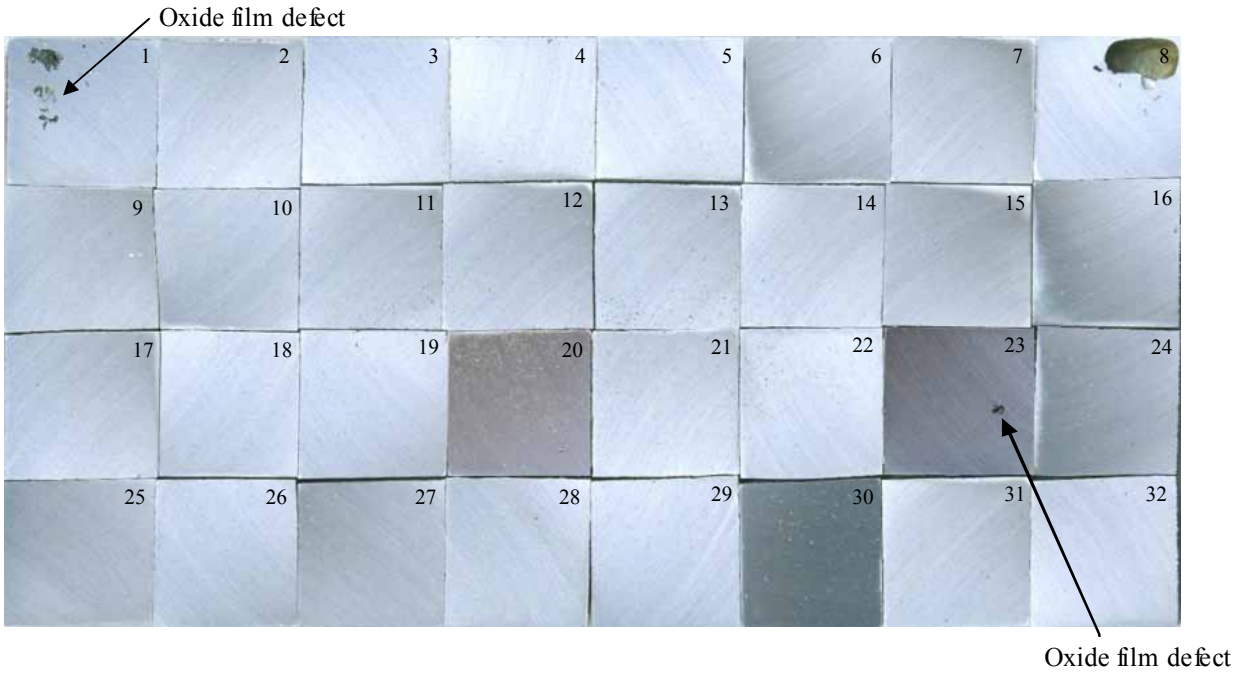


Figure 4.127 The macrograph showing the cross section of 32 sections of the medium oxide film casting (unfiltered and unstoppered casting).

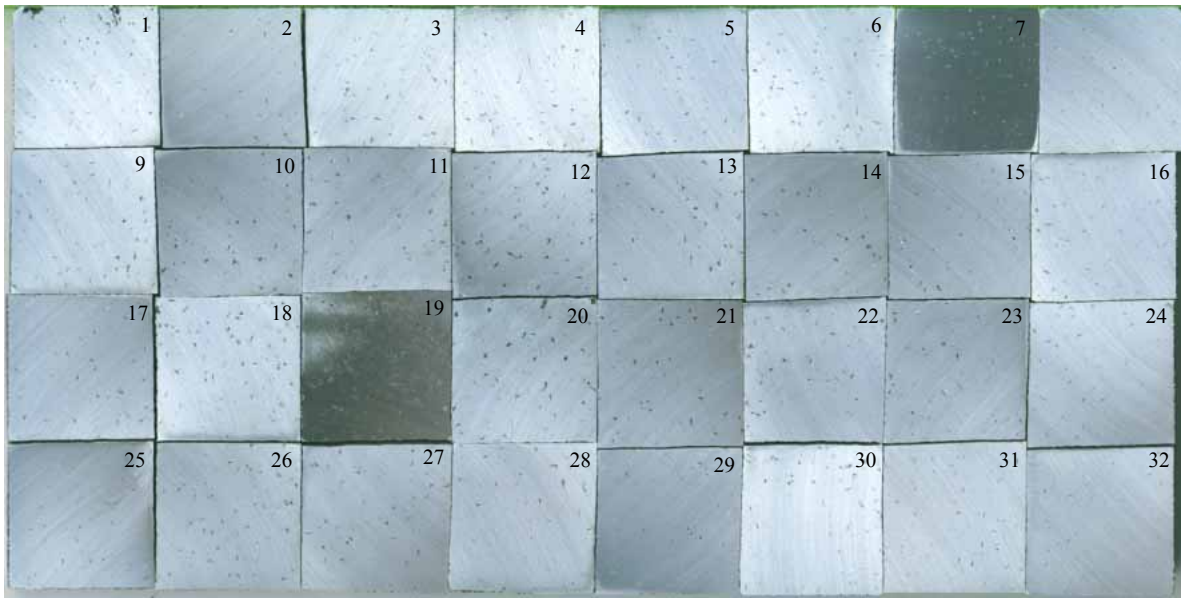
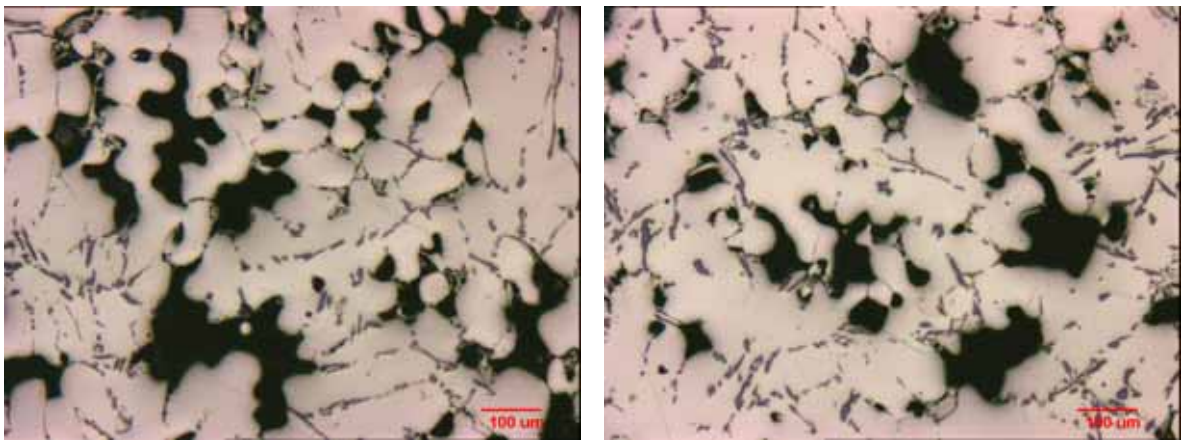


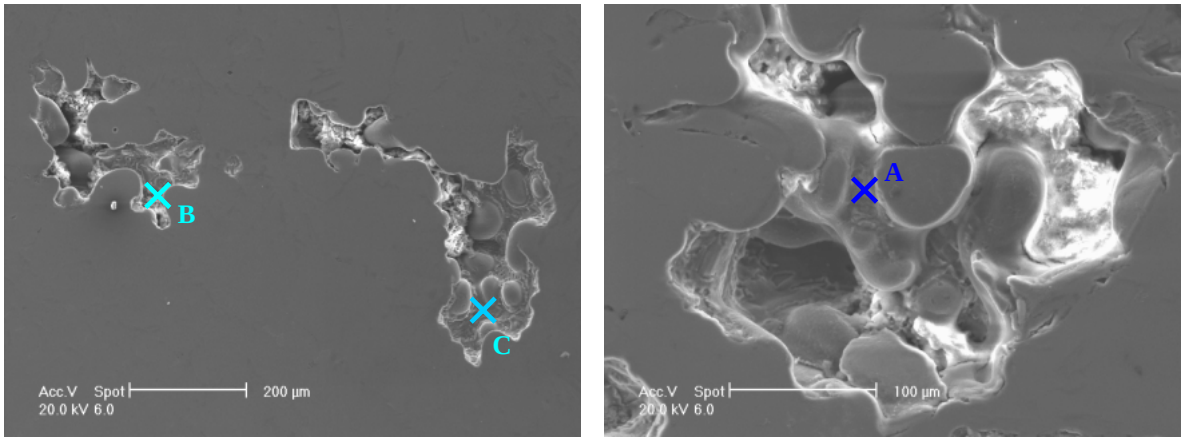
Figure 4.128 The macrograph showing the cross section of 32 sections of the high oxide film casting (unfiltered and stoppered casting).

Figures 4.129a and 4.129b show microstructures of the low oxide film casting obtained from sections 12 and 13 respectively. The porosity observed in this area was formed as connected microporosity in the interdendritic region, suggesting this was shrinkage porosity caused by inadequate feeding of volumetric shrinkage. Figures 4.130a and 4.130b show SEM images obtained from the same sections and associated EDX analyses results have been shown in Figures 4.131a to 4.131c. These images showed that the shrinkage porosity contained oxide films on the internal surface of the pores, suggesting relationship between oxide film and shrinkage porosity. Figure 4.132 shows shrinkage porosity obtained from section 20 of the medium oxide film casting, and Figures 4.133a and 4.133b show SEM images and Figures 4.134a and 4.134b show EDX analysis results from the porosity. The examination of pores in the three types of castings showed that more than 90% of observed pores (about 20 pores from each combination of oxide film defects) had oxides at the internal surface. This, therefore, suggested that oxide films played a role in the formation of shrinkage porosity.



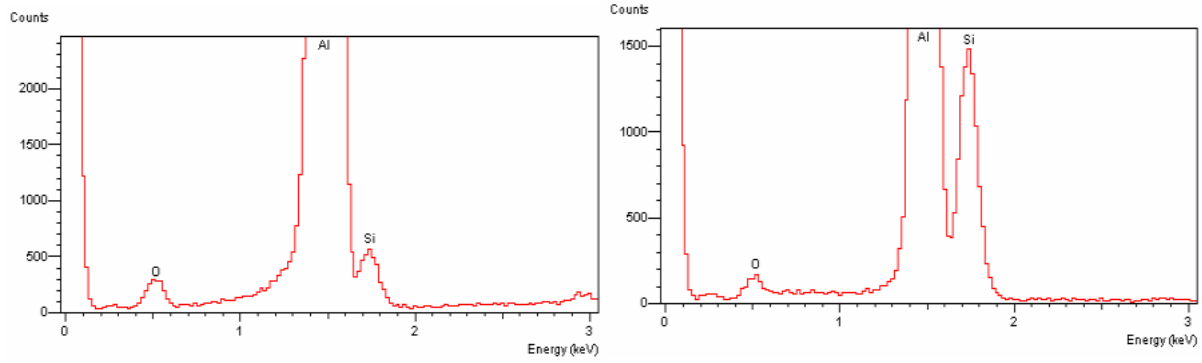
(a) (b)

Figure 4.129 Optical micrograph showing shrinkage porosity obtained from (a) section 12 and (b) section 13 of the low oxide film casting.

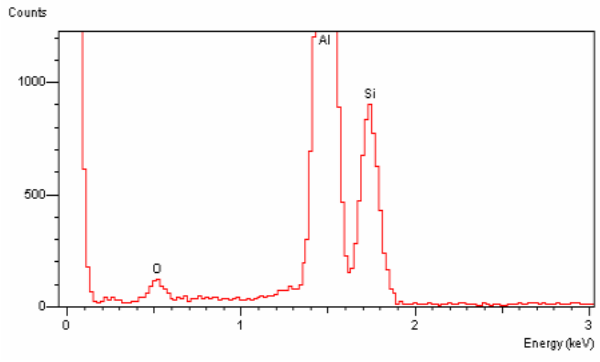


(a) (b)

Figure 4.130 The scanning electron micrographs of the cross section of a) section 12 and b) section 13 obtained from the low oxide film casting showing the shrinkage porosity.



(a) (b)



(c)

Figure 4.131 The EDX analysis results obtained from points A to C in Figure 4.125a and 4.130b.

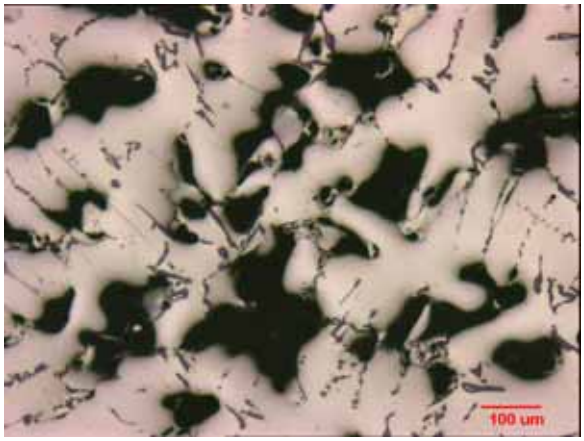
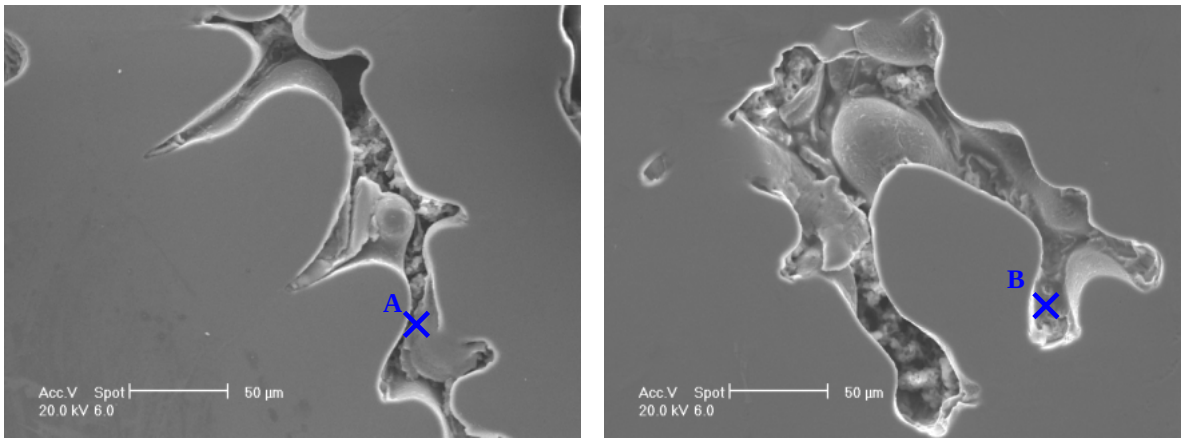
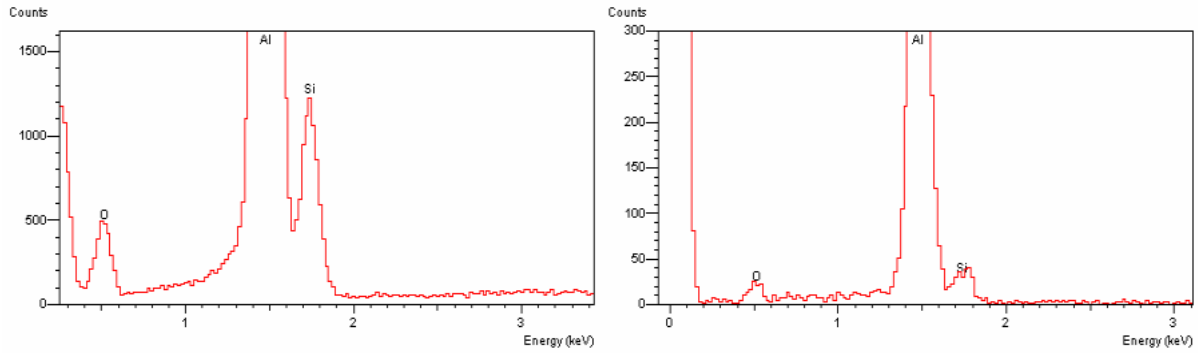


Figure 4.132 Optical micrograph of cross section of section 20 obtained from the medium oxide film casting showing shrinkage porosity.



(a) (b)

Figure 4.133 The scanning electron micrographs of cross section of section 20 obtained from the medium oxide film casting showing shrinkage porosity.



(a) (b)

Figure 4.134 The EDX analysis results obtained from points A and B in figure 4.133a and 4.133b.

In the high oxide film casting, shrinkage porosity was also observed. Figure 4.135 shows shrinkage porosity in microstructures of the high oxide film casting obtained from the central area of the cast plate (section 20). Beside shrinkage porosity, an elongated pore or crack-like porosity, was frequently observed in every part of the casting. Figure 4.136 shows a microstructure from the high oxide film casting (section 4). Figure 4.137 shows an SEM image of the section and Figure 4.138 shows the associated EDX analysis result. These suggest that these defects were entrained oxide films. Figure 4.139 shows an SEM image of an extensive oxide film defect obtained from section 4 of the high oxide film casting. Figures 4.140a and 4.140b show higher magnification images of the oxide films, and associated EDX analysis results have been shown in Figures 4.141a and 4.141b. The presence of large oxide film defects suggested that the stirring action during melt preparation and the greater surface turbulence produced during mould filling, compared to the other castings, had led to larger numbers of larger entrained oxide films in every section of the casting.

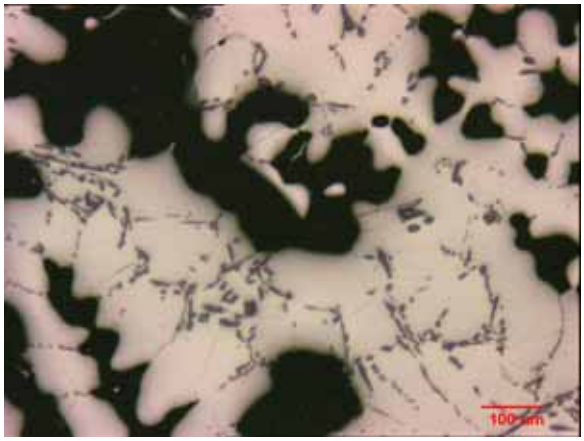


Figure 4.135 Optical micrograph of cross section of section 20 obtained from the high oxide film casting showing shrinkage porosity.

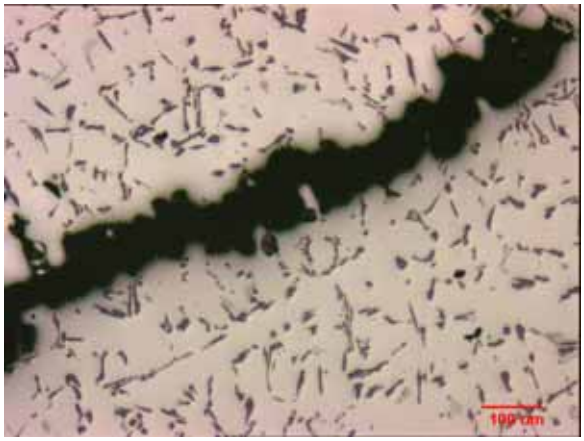


Figure 4.136 Optical micrograph of cross section of section 4 obtained from the high oxide film casting showing oxide film defects.

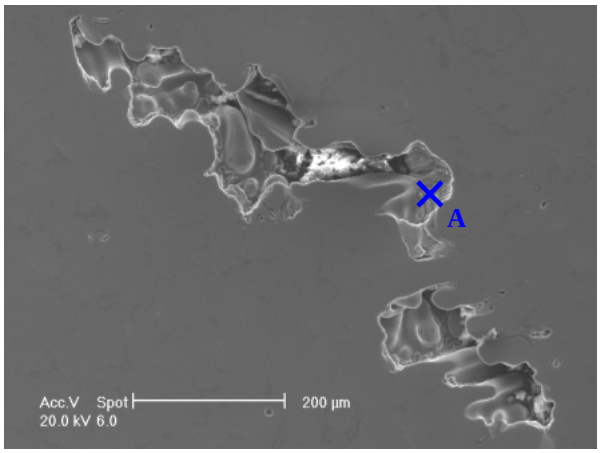


Figure 4.137 The scanning electron micrographs of cross section of section 4 obtained from the high oxide film casting showing oxide film defects in the casting.

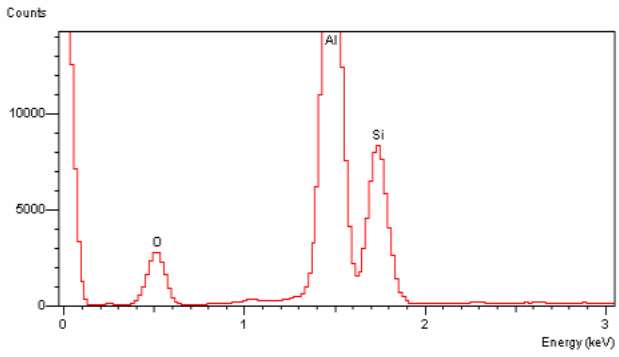


Figure 4.138 The EDX analysis result obtained from point A in figure 4.137.

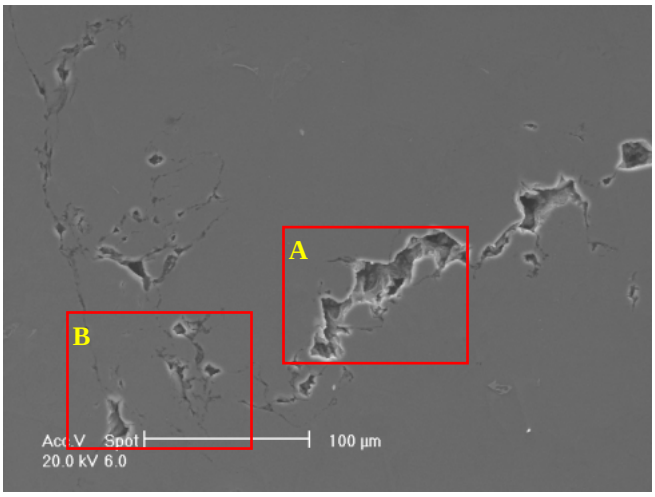
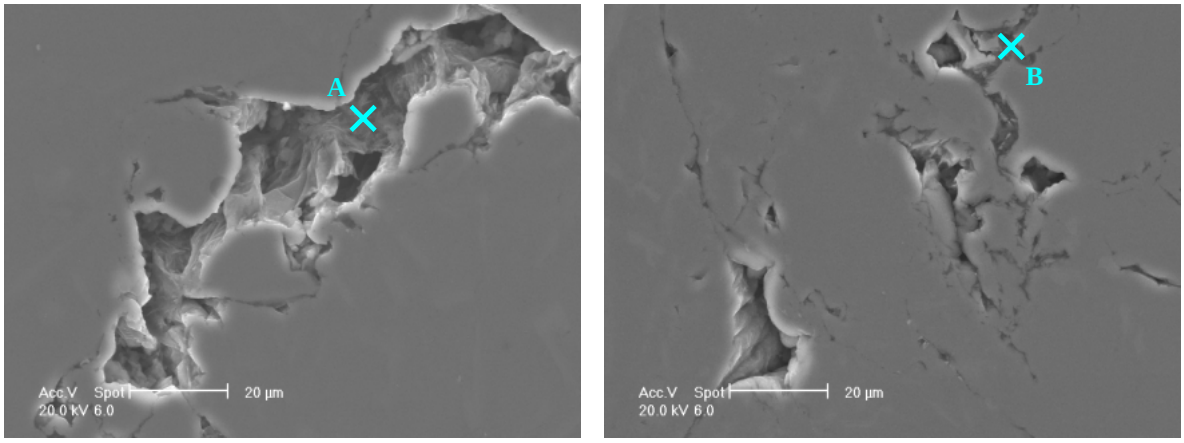
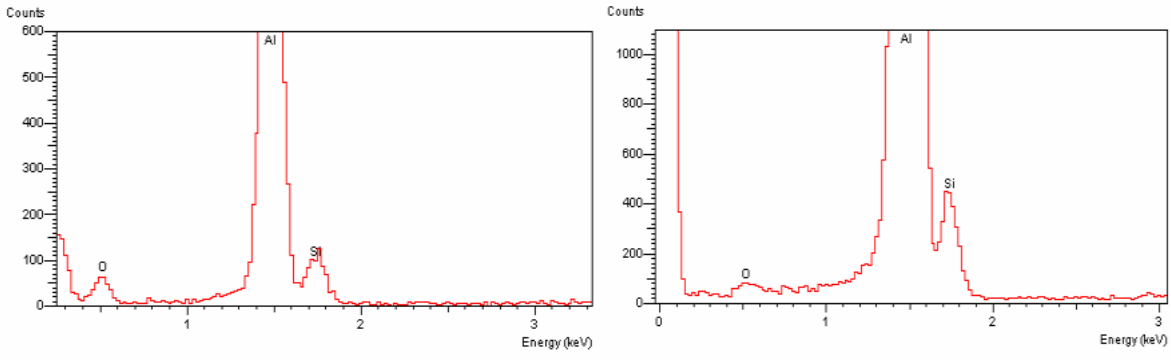


Figure 4.139 The scanning electron micrographs of cross section of section 4 obtained from the high oxide film casting showing the extensive oxide film defects.



(a) (b)

Figure 4.140 The scanning electron micrographs of section 4 obtained from the high oxide film casting showing the higher magnification of areas A and B in Figure 4.139.



(a) (b)

Figure 4.141 The EDX analysis results obtained from points A and B in Figure 4.140a and 4.140b.

4.4.3 Image analysis

The micrographs of the 32 sections of the cast plates were subjected to image analysis. The results for porosity area, number of pores in the section and mean length of pore obtained for the 3 castings have been shown in Tables 4.36, 4.37 and 4.38 respectively. The low oxide film casting appeared to have the lowest mean porosity area, mean number of pores and mean length of pore (about 0.29%, 117 pores and 148 µm respectively) while the high oxide film casting had the highest mean porosity area, mean number of pores and mean length of pore (about 1.03%, 165 pores and 249 µm respectively). The mean porosity area, mean number of pore and mean length of pore in the medium oxide film casting was 0.44%, 128 pores and 155 µm respectively, values intermediate between the low and high oxide film castings although closer to the low oxide film casting than the high oxide film casting. The large air bubble in section 8 of the medium oxide film casting was not included in the image analysis. The results show that increasing oxide film content in the medium oxide film casting resulted in a slight increase in porosity area, number of pores and the length of pore of about 0.15%, 11 pores and 7 µm respectively. The further increase in oxide film, and increase in hydrogen content by 0.1 ml/100g, in the high oxide film casting significantly affected the presence of porosity in the casting causing a three-fold increase in mean porosity area, while the

number of pores and the length of pore were increased by 40% and 70% compared to the low oxide film casting.

Table 4.36 Image analysis results of 32 sections obtained from the low oxide film casting (filtered casting).

Part	Pore area (%)	Number of pore	Average length of pore (μm)
1	0.03	7	201
2	0.15	61	148
3	0.09	23	183
4	0.14	56	141
5	0.18	63	159
6	0.12	57	114
7	0.08	28	155
8	0.03	14	140
9	0.12	48	136
10	0.29	118	139
11	0.45	193	131
12	1.29	524	139
13	1.49	573	168
14	0.39	147	135
15	0.19	94	114
16	0.06	15	175
17	0.12	35	182
18	0.18	107	126
19	0.43	199	184
20	0.69	369	114
21	0.97	435	130
22	0.26	126	138
23	0.16	83	109
24	0.05	8	197
25	0.06	12	191
26	0.06	30	127
27	0.14	59	144
28	0.10	38	137
29	0.14	58	130
30	0.03	18	123
31	0.06	29	130
32	0.05	15	199
Avg.	0.29	117	148

Table 4.37 Image analysis results of 32 sections obtained from the medium oxide film casting (unfiltered and unstoppered casting).

Part	Pore area (%)	Number of pore	Average length of pore (μm)
1	3.29	55	472
2	0.17	49	165
3	0.07	30	140
4	0.20	79	125
5	0.14	47	181
6	0.15	72	134
7	0.12	51	153
8	0.21	19	244
9	0.11	51	148
10	0.18	87	111
11	0.54	246	126
12	0.99	299	129
13	1.33	395	159
14	0.30	149	124
15	0.31	132	134
16	0.15	67	161
17	0.13	54	140
18	0.29	92	162
19	0.95	308	149
20	1.39	551	142
21	0.87	411	126
22	0.83	305	150
23	0.55	107	209
24	0.19	92	141
25	0.08	46	126
26	0.10	65	96
27	0.11	49	139
28	0.14	52	131
29	0.16	68	130
30	0.12	54	148
31	0.12	31	208
32	0.04	18	129
Avg.	0.44	128	155

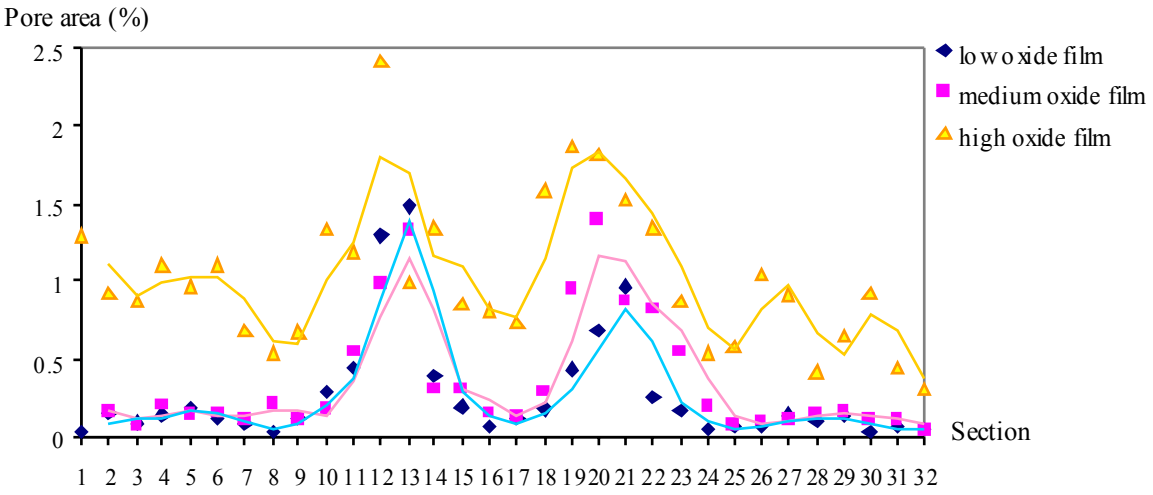
Table 4.38 Image analysis results of 32 sections obtained from the high oxide film casting (unfiltered and stoppered casting).

Part	Pore area (%)	Number of pore	Average length of pore (μm)
1	1.12	145	286
2	0.93	148	263
3	0.87	117	290
4	1.10	177	308
5	0.96	140	287
6	1.10	131	321
7	0.68	151	207
8	0.53	157	166
9	0.67	192	179
10	1.23	186	249
11	1.19	263	199
12	2.42	343	243
13	0.99	133	271
14	1.35	223	224
15	0.85	157	235
16	0.81	142	262
17	0.73	145	231
18	1.59	199	276
19	1.87	293	229
20	1.83	185	249
21	1.52	255	231
22	1.34	164	269
23	0.87	164	220
24	0.53	108	245
25	0.59	127	223
26	1.04	149	280
27	0.92	152	260
28	0.42	97	230
29	0.65	109	294
30	0.93	117	327
31	0.44	110	249
32	0.30	110	174
Avg.	1.03	165	249

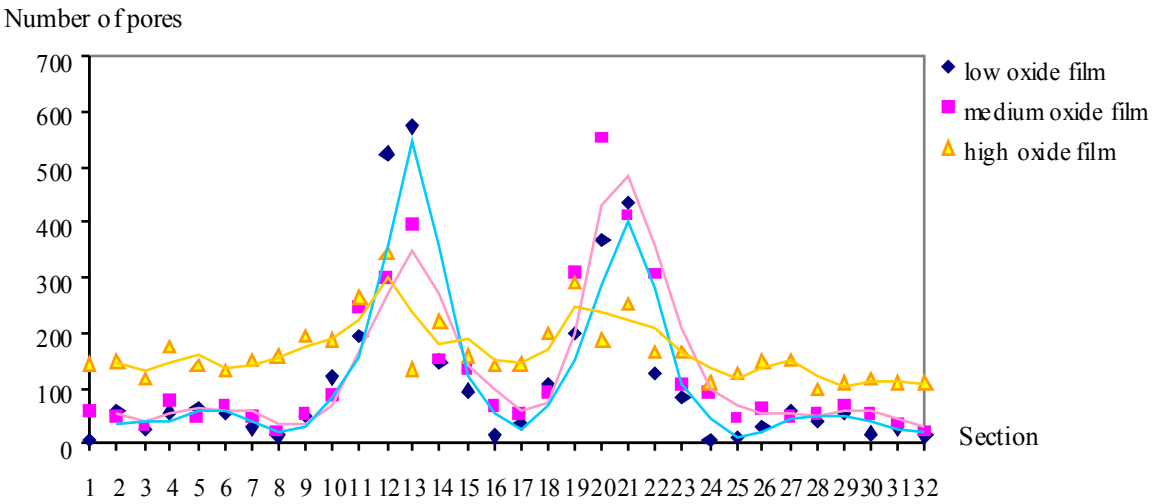
Figures 4.142a, 4.142b and 4.142c respectively show the distribution of the porosity area, the number of pores per section and the length of pore obtained from the image analysis results of the 3 types of casting. It can be seen that the data was distributed the same way as the distribution obtained from the density results. The distribution of porosity area and the number of pores obtained from the low oxide film casting and the medium oxide film casting were similar. Most sections of the castings had a porosity area less than 0.3%, as was to be expected in the low hydrogen content casting.

The increase in oxide film in the high oxide film casting resulted in an increase in the number of pores and pore area in most sections of the casting. However, the increase in hydrogen content would influence the formation of porosity in this casting. The distribution diagram also showed that the number of pores at the centre of the high oxide film casting was lower than in the low and medium oxide film castings. For example, in section 13, the number of pores in the high oxide film casting was only 133 pores, while the medium oxide film and the low oxide film casting had 395 and 573 pores respectively. However, the mean number of pores from every section in the high oxide film casting was still higher compared to the other castings. This suggested that an increase in number of pores in every section of the casting might influence the formation of shrinkage porosity, which mostly formed in the central area (the last zone to solidify).

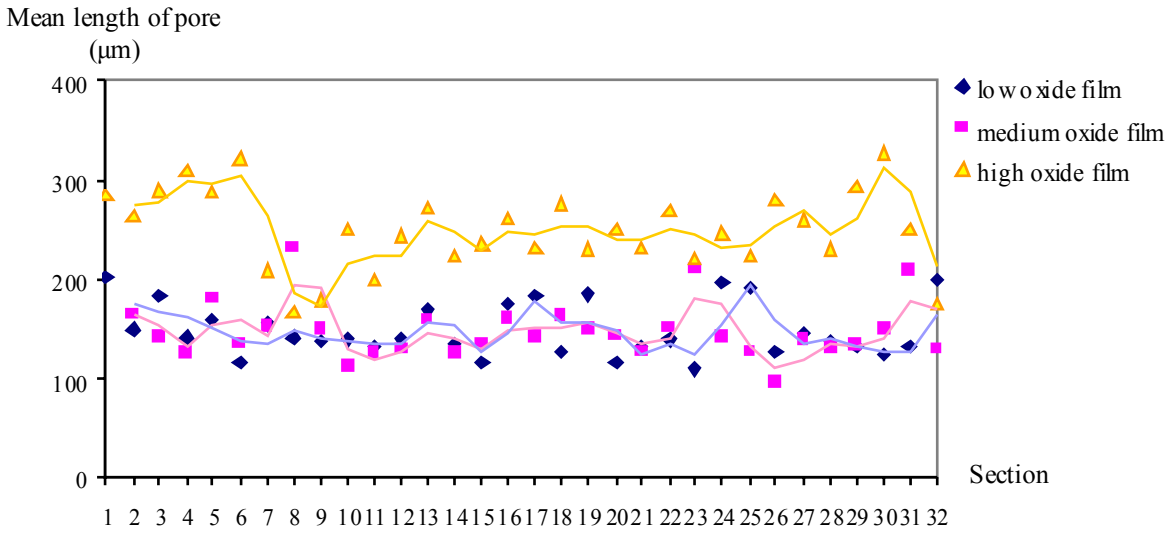
In summary, the microstructures and SEM results showed that entrained oxide films had an effect on the formation of shrinkage porosity since more than 90% of the shrinkage porosity observed in this experiment contained oxide films at the internal surface of pore, (i.e. less than 10% of pores did not contain oxide films). Increasing oxide film content in the medium oxide film casting showed no significant effect on the formation of shrinkage porosity, while an increase in the presence of porosity was observed in the high oxide film casting. However, the effect of increasing hydrogen has to be considered in this case.



(a) porosity area %



(b) number of pores per section



(c) mean pore size

Figure 4.142 a) distribution of a) porosity area, b) number of pores/cm^2, and c) mean pore size data obtained from 3 types of the castings.

CHAPTER 5

DISCUSSION

This chapter examines and discusses the characteristics and effects on tensile properties of Al-Si-Mg alloys produced by the three deleterious defects, namely oxide films, Fe-rich phase and porosity, using the results obtained from tensile property testing and image analysis. In addition, interrelationships between them will be commented upon.

5.1 Oxide film defects in cast aluminium alloys

Entrained oxide films have become a well known microstructural defect. They are initially formed on the surface of a molten aluminium alloy when it is exposed to an oxidising atmosphere and introduced into the casting during mould filling by surface turbulence. Since oxide films have a deformability and flexibility, they tend to be compressed or bent by surface turbulence. The folded over oxide films, dry side to dry side, will trap some air between them and act as a crack-like defect or well known as double oxide film defect in the final casting. Oxide film defects were frequently observed on the fracture surfaces of the test bars and in the microstructures obtained from polished samples in this study, particularly in the unfiltered castings. At least two large oxide film defects, (of more than 2 mm length), were observed by visual inspection in every 30 test bars of the unfiltered castings. The fracture surfaces shown in Figures 4.6, 4.10, 4.13, 4.16 and 4.84 clearly showed the doubled-over nature of oxide film defects, revealed by the fact that symmetrical oxide films were apparent on both sides of the fracture surfaces, opened up by the fracture of the test bar. The images showed no evidence of any bonding developed across the internal oxide-oxide interface. It therefore acted as a pre-existing crack and played a part in the reduction of the mechanical properties of the castings.

The SEM images also showed that both young and old oxide films, defined by their different thickness, were observed in the castings. The thickness of oxide films was

measured by estimating the width of the wrinkle or crease in the film. As shown in Figures 4.25a, 4.25b and 4.66, young oxide films were thin, transparent, and had fine wrinkles. Their approximate thickness of less than one micron suggested that young oxide films were newly formed during pouring or mould filling [Campbell 2000]. Old oxide films, as shown in Figures 4.9a and 4.9b, had coarse wrinkles and varied thickness, of up to several microns. The EDX analysis results shown in Figure 4.9c also showed that the old oxide film had a significantly higher oxygen content compared to young oxide films (see Figures 4.25c and 4.67). Since time is required for the thickening, this suggested that the old oxide film was formed in the holding furnace or during melt transfer.

The maximum length of the double oxide film defects observed in the castings varied from a few microns (see Figure 4.111), to at least 7 mm (across the fracture surface of the test bar and presumably therefore larger than the test bar diameter) as shown in Figure 4.10. Their size depended on the filling systems used and the surface turbulence produced in the mould. In an unfiltered mould, extensive double oxide film defects were easily detected in the microstructures (see Figures 4.50, 4.51, 4.53, 4.54, 4.113, 4.121, 4.123 and 4.139). These defects are similar to the crack-like defects found in the unfiltered cast Al-Si-Mg alloys (see Figure 2.7) carried out by Green and Campbell [1994]. Their larger size, compared to other types of defects, produced a significant effect on the mechanical properties of the castings. The SEM images show that large double oxide film defects were caused by considerable surface turbulence that might have occurred in the melt preparation or melt transferring process. The absence of a crumpled oxide film in the filtered castings shows the effects of filters on decreasing double oxide film defects. This suggested that the filter could be used to reduce the surface turbulence in the mould by controlling the in-gate velocity of the liquid metal, and also would trap any large oxide films formed before the mould filling process. However the presence of double oxide film defects was still observed in the filtered castings (e.g. Figures 4.20, 4.25, 4.109 and 4.111), therefore oxide films can still be a common defect, and almost unavoidable despite the use of a filter.

The EDX analysis results of oxide film defects showed that $MgO.Al_2O_3$ or spinel (see Figures 4.8, 4.9c, 4.12, 4.15, 4.18, 4.55 and 4.86) were the main oxide films in the cast Al-Si-Mg alloys. This supports the suggestions that spinel is expected to be formed in aluminium alloys at magnesium levels of between 0.005 and 2.0 wt% since the formation of MgO requires less free energy than the formation of Al_2O_3 [Makarov 1999, Campbell 2000]. However, there also was some oxide film, particularly the young oxide film, that contained a small amount of magnesium or was likely to form as Al_2O_3 (e.g. Figure 4.25c, 4.67). This might be due to the old oxide films, which previously formed in the furnace or during melt transfer, were previously formed as spinel and magnesium underneath these film would be consumed for the thickening of the oxide films. The young oxide film, which newly occurred in the mould, therefore formed as Al_2O_3 after a local decrease in magnesium content. On the other hand, the lack of magnesium in the very thin oxide film might be caused by the difficulty of measurement using EDX analysis. For the high purity aluminium and high purity Al-Si alloy experimental cases, the oxide films found were, of course, Al_2O_3, (e.g. Figures 4.112, 4.115, 4.122 and 4.124).

5.1.1 Effect of entrained oxide films on the tensile properties of castings

As mentioned, the double oxide film defects, containing a gap between the two dry sides of the films, act as crack-like porosity, and can result in a great reduction in tensile properties. The tensile property data shown in Tables 4.1 and 4.2 relating to filtered and unfiltered castings showed that the increase in oxide film defects directly resulted in a reduction in tensile properties since the mean UTS and mean elongation noticeably decreased in every high oxide film casting. The Pareto diagrams in Figure 4.1 calculated from all tensile data showed that the effects produced by oxide film defects (column C) on the UTS and elongation of the Al-Si-Mg alloy resulted in a reduction of about 21 MPa and 0.9% respectively. The variety in shape and size of oxide film defects also made them have a variety of influences on the mechanical properties of the castings. In the unfiltered castings, extensive oxide films could be observed on the fracture surfaces of the test bars and these defects were sometimes present on the majority of the area of the fracture surfaces (see Figures 4.6 and 4.16), causing great structural weakness in the

test bar. The results showed that large oxide film defects decreased the UTS by about 150 MPa, for example, test bar 21 in the high oxide film, high Fe-rich phase and high hydrogen casting (UTS of 74 MPa) and test bar 21 in the high oxide film, low Fe-rich phase and low hydrogen casting (UTS of 117 MPa). However, oxide films were not found to be the most detrimental defects in this study. This is because the experiment attempted to bracket the extremes of casting practice, in that the molten metal used had a high quality and the running system used was not extremely bad, but represented what might be used in a foundry. If the molten metal quality was low or a very bad running system had been used, that would generate many more oxide film defects, for example, the running system of the plate casting shown in Figure 3.13, then the deleterious effect would have been much larger.

In the experiment examining the interactions between oxide film and shrinkage porosity in the Al-Si-Mg alloys with low and high Fe content, the Pareto diagrams obtained from the tensile data (see column A in Figures 4.64 and 4.81) showed that the effect on tensile properties produced by the oxide film defect was lower than in the previous experiment (the effect on UTS was about 9 MPa). Although it was difficult to measure the oxide film defects from both qualitative and quantitative points of view, the x-ray images of the liquid metal flow (see Figure 3.6) showed that there was more surface turbulence produced in this mould, compared to the unfiltered mould in the first experiment (see Figure 3.3), suggesting that more oxide film defects were introduced into the castings during mould filling than in the case of the first experiment. Nonetheless large double oxide films on the fracture surfaces and in the microstructure appeared to a lesser extent than was expected. As shown in the SEM images of fracture surfaces, the large double oxide films, which had a remarkable effect on the tensile properties, were the old oxide films (e.g. Figure 4.9 which had a UTS of 157 MPa). This suggested that the large old oxide film defects were normally formed by holding in the furnace, or during melt transfer, played a major role in a reduction in tensile properties of the castings whereas double oxide film defects that newly formed during mould filling had a less effect (e.g. Figures 4.22 and 4.23, which had a UTS of 261 MPa). The cleaner melt, therefore, has better tensile properties at the same oxide film content produced in the mould. The result of the melt quality tests shown in Figure 3.7 suggested that the alloy used in this

experiment was cleaner since the flow time for the 1400 gram melt was only 31 seconds compared to that of 39 seconds in the first experiment as shown in Figure 3.4. A study of cleanliness measurements using the same technique in Al-Si-Mg alloys was presented by Godlewski and Zindel [2001]. They reported that an aluminium alloy melt that was degassed/fluxed for 5 minutes with a temperature of 720 ^{o}C had a flow time for the 1400 gram of melt of about 50 seconds. This showed that in comparison the alloy melt used in the experiments described here was very clean. This therefore suggests that the extensive oxide film defects were not introduced into the castings as much as in the previous experiment.

The Weibull distribution for a single defect distribution was applied to describe the tensile properties data obtained from the combinations of castings. Green and Campbell [1993] suggested that a linear equation obtained from a Weibull plot of $ln(ln(1/1-F_w))$ versus $ln(x)$ (Equation 2.10) was an accurate distribution estimator of tensile strength. As mentioned the oxide film defects in the castings formed in a variety of shapes and sizes, which therefore influenced the distribution of tensile properties by increasing the scatter or the range of tensile property data. Tables 4.5, 4.6, 4.17 and 4.26 show the Weibull modulus obtained from the Weibull plots of the tensile property data. These show that increasing oxide film content in all high oxide film or unfiltered castings resulted in a reduction in the Weibull modulus. For example, in the low Fe and low hydrogen castings of the first experiment, increasing oxide films resulted in a reduction in the UTS Weibull modulus by about 51. The Pareto diagrams in Figures 4.34a and 4.34b show that oxide film defects had an effect on the UTS Weibull modulus and the elongation Weibull modulus of a reduction of about 37 and 3.2 respectively. These agree with results of experiments by Green and Campbell [1994] and Mi et al. [2004] which showed that entrained oxide films were responsible for much of the scatter in tensile properties of cast aluminium alloys.

In addition, the oxide film defects affected the distribution manner of the tensile properties. It can be seen in the Weibull plots (Figures 4.31b, 4.32b, 4.73b, 4.74b, 4.95c and 4.96c) that the tensile properties data, particularly the UTS data, did not plot linearly as would be expected if the data was distributed in the form of a Weibull single defect

distribution. This indicated that either the data was distributed in a non-Weibullian manner, or there was more than one defect type competing to cause the failure. The latter alternative was confirmed by observations of the fracture surface because the large (old) oxide film defect found on the fracture surfaces seemed to be another defect type competing to cause the failure in the tensile test.

Generally, the failure of cast Al-Si-Mg alloys is caused by the presence of brittle particles, for example Fe-rich and Si phases, which act as stress raisers and initiators of cracks [Murali et al. 1995, Taylor et al. 1999]. The mechanism of failure caused by a brittle fracture will be discussed in the section on the effect of Fe-rich phase on tensile properties (section 5.2.1). In the low oxide film castings, the fracture therefore was dominated by the cracks initiated in the Fe-rich phase as shown in Figures 4.2a, 4.4 and 4.82. The presence of double oxide film defects also affected the failure mechanism of the casting since their doubled nature acted as pre-existing cracks and could dominate the failure of the casting. As mentioned that double oxide film defect is almost unavoidable in the practice, the normal failure of castings is therefore caused by a combination of Fe-rich phase and double oxide film defect. However, the presence of large double oxide film defects can affect the failure mechanism of the castings and resulted in a great reduction in tensile properties. This is supported by the SEM images showing that the large double oxide film defects were observed on the fracture surfaces of every low UTS test bar (e.g. Figures 4.6, 4.10, 4.13, 4.16 and 4.84). It can be seen in the Weibull plots of the tensile property data that the failure caused by a large oxide film defects was distributed in a different manner compared to that caused by the normal failure mechanism. Figures 4.33a, 4.33b, 4.75 and 4.97 show that the distribution of UTS data obtained from the high oxide film content casting could be divided with two trend-lines, first was the Weibull distribution associated with failure where the initiation of the crack was caused by the brittle particles and small double oxide film defects in the test bar and second was the Weibull distribution associated with the failure dominated by large double oxide film defects. It can be seen that 2 separate lines, classified by the different crack initiation methods gave the best fit. The Weibull plots of the new trend-lines of the data show that when oxide film defects dominated the failure gave very low Weibull modulus values were obtained compared to the low oxide film castings, (see table 4.6).

This suggests that double oxide film defects, particularly large oxide film defects, resulted in a great reduction in the reliability and reproducibility of castings.

The effects of oxide film on the distribution of tensile properties obtained from this study were similar to the work of Nyahumwa et al [1998] who studied fatigue properties of cast aluminium alloys. They used the three-parameter Weibull models for partially concurrent double defect distributions to describe fatigue life behaviour where the Weibull analyses were obtained from computer software to give the best fit of the data. This suggests that the Weibull distribution, that is thought to be an accurate statistical tool for describing the distribution of tensile properties in aluminium alloys, may not be used for castings that contain double oxide film defects. Other models, for example the three-parameter Weibull distribution, may be a better distribution estimator.

The results obtained from the Weibull plots of the tensile properties in this study also showed that the effect produced by oxide films in the castings was mainly caused by large old double oxide film defects. Figure 4.33 shows that the new trend-lines of the data obtained from the high oxide film castings that did not contain large double oxide film defects gave a high UTS Weibull modulus, for example, in the low Fe and high hydrogen castings, the UTS Weibull modulus increased to 42, which was the same level of Weibull modulus obtained from the low oxide film castings (Weibull modulus of 44). To estimate the effect of double oxide film defects, which newly formed in the moulds, the low UTS values containing large oxide film defects were therefore taken out. Figure 5.1 shows the new Pareto diagram of UTS Weibull modulus after large oxide film defects were removed. It can be seen that Fe-rich phase had the greatest effect on the distribution of the UTS in the case of castings that contained no large oxide film defects. This supports the fact that the brittleness of Fe-rich phase influences the tensile properties of the cast aluminium alloys since the failure of test bars were mainly controlled by Fe-rich phases. The variation of the size and the orientation of the Fe-rich phases, particularly the large β-phase platelets, therefore affected the distribution of tensile properties. The diagram also shows that the effect of young oxide film defects on UTS Weibull modulus was only 17 or a decrease of 57% compared to that produced with the large double oxide film defects included (see Figure 4.34). This therefore suggests

that the reliability of the cast aluminium alloys can be improved by removing large double oxide film defects from the melt.

Figures 5.2a and 5.2b show the new Pareto diagram obtained from the UTS and elongation values from the 8 combinations of castings by removing the test bars that contained large double oxide film defects. The diagrams show that the effects on UTS and elongation produced by young oxide film defects were decreased significantly, by about 57% and 27% respectively, compared to the effect produced with large oxide film defects included (as shown in Figure 4.1). This suggested that, when the large old oxide film defects previously formed in the furnace or during melt transfer were not considered the young oxide film defects had the least detrimental effect on tensile properties compared to Fe-rich phases and gas porosity. This might be due to; either the size of double oxide film produced in the moulds was less than Fe-rich phases and gas porosity, or the amount of oxide film defects produced by the surface turbulence in the unfiltered moulds was not greatly different compared to the filtered moulds.

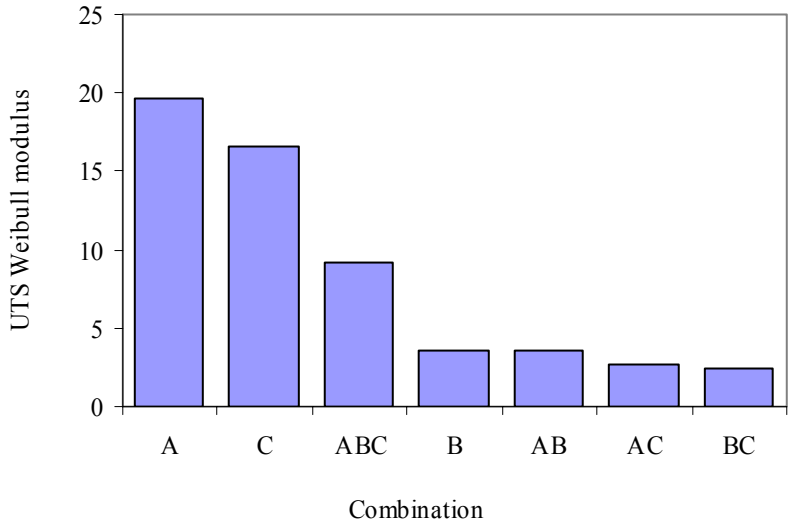
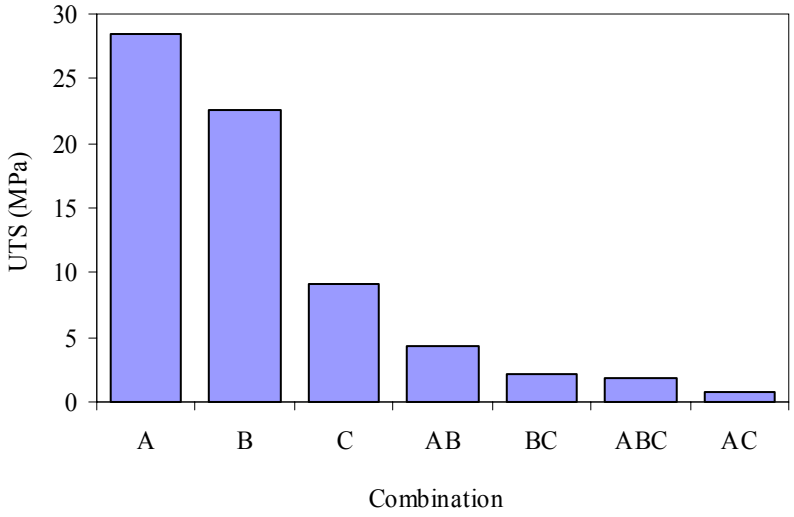
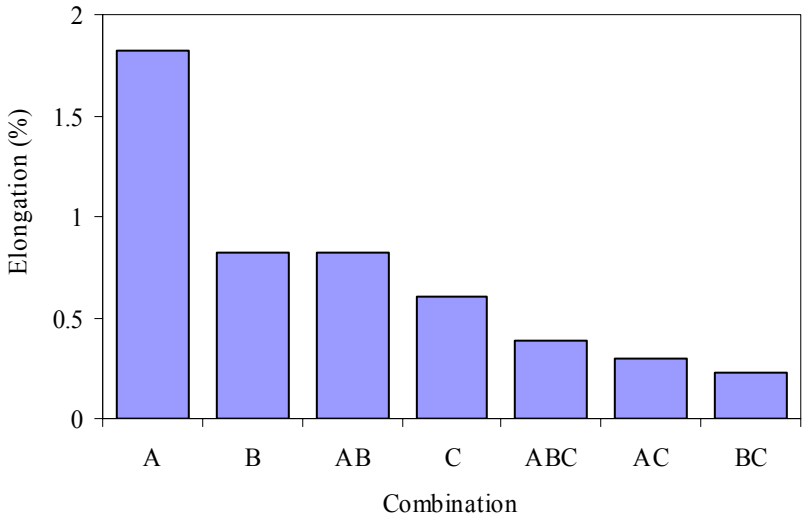


Figure 5.1 Pareto diagram showing the effects of defects and their interaction on UTS Weibull modulus after removing the test bars that contained large double oxide film defects (A = Fe-rich phase, B = hydrogen, C = oxide film).



(a)



(b)

Figure 5.2 Pareto diagram showing the effects of defects and their interaction on (a) UTS and (b) elongation after removing the test bars that contained large double oxide film defects (A = Fe-rich phase, B = hydrogen, C = oxide film).

5.2 Fe-rich phases in cast aluminium alloys

Iron is the most common impurity in aluminium alloys since it cannot be economically removed. It is widely accepted that high iron contents are responsible for inferior mechanical properties of aluminium alloys due to the presence of β-Al_5FeSi phase. This phase, like most intermetallic particles, is brittle, and because of its platelet-like or needle-like morphology, up to a millimetre long, β-Al_5FeSi phase directly influences the strength and ductility of cast Al alloys. In this study, the aluminium alloy used was Al-7Si-0.3Mg alloy with 3 different Fe contents (0.1, 0.5 and 1.1 wt%). The results obtained from the microstructural images show that the main Fe-rich phases observed in the experimental alloys were β-Al_5FeSi, and π-$Al_8FeMg_3Si_6$ phases.

During the solidification of Al-Si eutectic alloys (see Table 2.4), the nucleation of particles and intermetallic phases may be divided into three different types: pre-eutectic, eutectic and post-eutectic [Backerud et. 1990]. After mould filling was completed, the molten metal started to solidify and in the pre-eutectic period ($T > T_{E\ (575^oC)}$) the first phase to precipitate following the α-Al dendrites was the β-Al_5FeSi phase. In the main eutectic reaction ($T = T_{E\ (575^oC)}$) the β-Al_5FeSi phase would precipitate together with Al-Si eutectic. In the post-eutectic stage ($T < T_{E\ (575^oC)}$), β-Al_5FeSi phase might transform to π-$Al_8FeMg_3Si_6$ phase and there would also occur precipitation of Mg_2Si.

The presence of π-$Al_8FeMg_3Si_6$ phase was observed as the main Fe-rich phase in the microstructures of castings obtained from the runner bar, particularly in the low Fe content castings (0.1 wt%), as shown in Figures 4.35 and 4.36. This phase was formed as a Chinese script-like morphology and is thought to be less harmful to the mechanical properties of castings [Shabestari et al. 1995, Roy et al. 1996]. However the results obtained from micrographs and the SEM images shown in Figures 4.38 and 4.39 showed that heat treatment resulted in the absence of π-$Al_8FeMg_3Si_6$, by changing π-phase back to β-phase.

The observation of Fe-rich phase in all experiments (e.g., Figures 4.26, 4.28, 4.38, 4.39, 4.41, 4.42, 4.87, 4.89 and 4.98) shows that increasing Fe content from 0.1 to 1.1 wt%

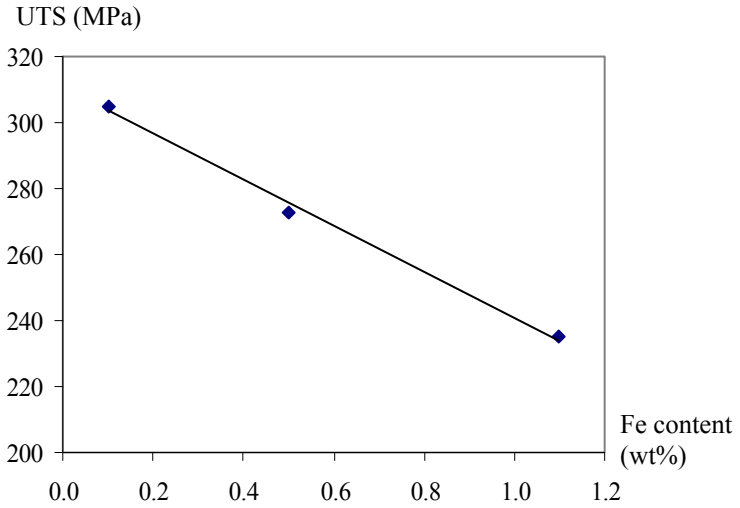
resulted in an increase in the size of the β-Al_5FeSi phase. The images showed that the length of β-Al_5FeSi phase was about 5 μm in the 0.1 wt% Fe content casting but increased with increasing Fe content to 40 μm at 0.5 wt%, and to 80 μm when the Fe content was increased to 1.1 wt%. This showed that Fe content would have a direct effect on the tensile properties of a casting, not only by increasing the amount of Fe-rich phase, but its size as well.

5.2.1 Effect of Fe-rich phases on tensile properties of the casting

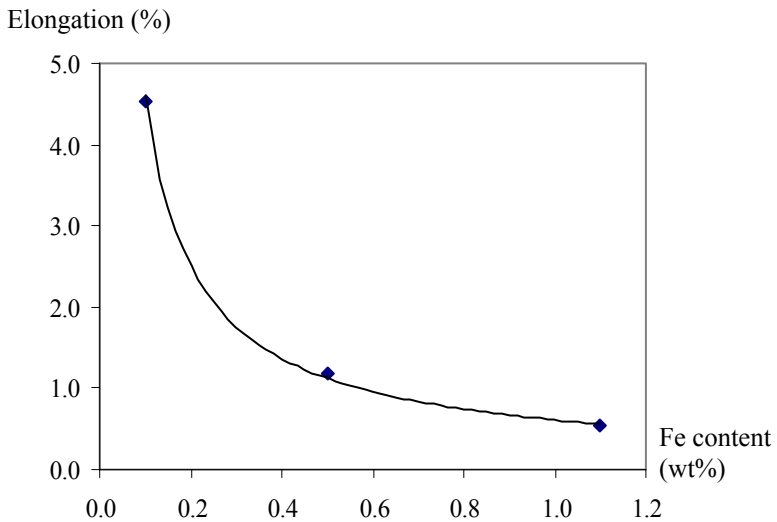
Many authors have suggested that the Fe-rich phase was responsible for inferior mechanical properties in cast aluminium alloys due to its brittle characteristic [Murali et al. 1995, Taylor et al. 1999]. This suggestion was supported by the results of this experiment because the Fe-rich phases, particularly the β-Al_5FeSi platelet, were observed on the fracture surfaces of all test bars and the SEM images revealed that cracked β-Al_5FeSi phases were easily observed (see Figures 4.2a, 4.4 and 4.82). The failure of alloys due to a brittle fracture can be explained in three stages as follows; 1) the initiation of cracks occuring in the Fe-rich phases, 2) the cracks becoming wider and forming cavities, and 3) the cavities joining together due to the collapse of the resisting matrix ligaments [Lawn 1993]. Therefore the presence of Fe-rich phase plays a major part in the failure of castings by acting as stress raisers and as initiators of cracks.

Cao and Campbell [2000] studied the effect of Fe-rich phase on the tensile properties of cast Al-Si-Mg alloys and suggested that the brittleness of Fe-rich phase might be the result of the presence of oxide film defects. In their work, transverse cracks in Fe-rich phases were observed, as shown in Figure 2.15, and they proposed that the cracks were actually double oxide films which had the Fe-rich phases nucleated independently on their wetted sides, acting as a precrack along the central axis of the Fe-rich phase. However, the results obtained from SEM images of the fracture surfaces and the associated EDX analysis in this experiment disagreed with their suggestion because no evidence of oxide films associated with cracks in the Fe-rich phase was observed. This therefore showed that the brittleness of the Fe-rich phase and cracks within it was due to the nature of the phase.

The Pareto diagrams in Figure 4.1 showed that increasing Fe content from 0.1 to 0.5 wt% had the greatest effect on tensile properties (column A), compared to gas porosity and oxide film defects, by decreasing the UTS and elongation by about 28 MPa and 1.7% respectively. This suggested that the brittleness of Fe-rich phases, particularly the large β-Al_5FeSi phase, significantly influenced the tensile properties of cast aluminium alloys. Figures 5.3a and 5.3b show the mean UTS and elongation of the castings containing Fe from 0.1 to 1.1 wt% with the conditions of low hydrogen and low oxide film content (see Tables 4.1, 4.2, 4.13, 4.14, 4.22 and 4.23).



(a)



(b)

Figure 5.3 Tensile properties of cast Al-Si-Mg alloy containing Fe.

Figure 5.3a shows an effect of Fe-rich phase on tensile properties such that the UTS of the castings had a linear relationship, with a decrease in UTS of about 7 MPa for every 0.1 wt% Fe increase. For example, an increase in Fe content from 0.1 to 0.5 wt% resulted in a reduction in mean UTS from 305 to 271 MPa and it decreased further to 235 MPa when the Fe content increased to 1.1 wt%. However, the decrease in tensile properties of Al-Si-Mg alloy with 1.1 wt% Fe might also be influenced by the reduction in magnesium, which is known to strengthen the alloy by precipitating Mg_2Si, because the chemical analysis results showed that the magnesium content in the experiment with 1.1 wt% Fe was reduced to 0.2% during the melt preparation. An effect of Mg on the UTS property in the sand-cast Al-7Si-0.3Mg alloys was reported by Drouzy et al. [1980]. They indicated that a decrease in Mg of about 0.13 wt% resulted in a reduction in UTS of about 20 MPa. This, therefore, suggested that the decrease in Mg only slightly influenced the tensile properties of the castings in this experiment and that the major effect was caused by the presence of the Fe-rich phase.

For elongation, it can be seen that increasing the Fe content from 0.1 to 0.5 wt% decreased ductility considerably, but with a further increase of the Fe content to 1.1 wt%, elongation was further reduced but less dramatically. This might be due to the β-Al_5FeSi platelets are brittle and therefore produce a great influence on the ductility of castings. The diagrams obtained from this study are similar to those presented by Ravi et al. [2002] who studied the mechanical properties of Al-7Si-0.3Mg alloy in the T6 heat treatment condition, (see Figure 2.17). This showed that the effects of Fe-rich phase on the tensile properties of aluminium alloys can be estimated.

In addition, the Weibull plots in Figures 4.31b, 4.32b, 4.95b, 4.95c, 4.96b and 4.96c and the Weibull modulus results in Table 4.5 and 4.26 showed that an increase in Fe content influenced the distribution of tensile properties by decreasing the Weibull modulus. With the low hydrogen and low oxide film content castings, increasing the Fe content in the castings from 0.1 wt% to 0.5 wt% resulted in a decrease in the UTS Weibull modulus from 55 to 26 and it was further decreased to 14 when the Fe content was increased to 1.1 wt%. It can be seen that the reliability (i.e., reproducibility of properties) of castings would decrease with an increase in Fe content. The Weibull modulus obtained from the

high Fe content castings, however, was still high compared to that of in the high oxide film castings. The Pareto diagrams in Figure 4.34 show that increasing Fe content from 0.1 to 0.5 wt% produced the effects on UTS Weibull modulus and elongation Weibull modulus about 10 and 0.5 respectively, which were three-times and six-times less than that produced by oxide film defects. This, therefore, showed that, although the Fe-rich phase had the greatest influence on the reduction of tensile properties, the distribution of tensile properties obtained from them was at least narrow and predictable, compared to the effects associated with high oxide film contents.

5.3 Porosity defects in cast aluminium alloys

Porosity is one of the most common defects that can be found in cast aluminium alloys [Anson and Gruzleski 1999, Sabau and Viswanathan 2002, Atwood and Lee 2003]. Porosity has been classified by its cause into gas porosity and shrinkage porosity. The micrographs obtained from all experiments show that both gas porosity and shrinkage porosity were observed in this study. In the low hydrogen content castings, (of about 0.1 and 0.2 ml/100g metal), the most frequently observed porosity was gas porosity, formed as microporosity, which had the average size of about 250 μm^2 (see Tables 4.9, 4.18, and 4.27) and was well distributed in the interdendritic regions of the castings as shown in Figures 4.43, 4.76 and 4.99. Increasing hydrogen content to about 0.45 ml/100g metal had a significant effect on the presence of gas porosity by increasing the area and size of porosity in the castings. Figures 4.43 and 4.116 showed that pores, larger than the interdendritic cell size and was visible to the naked eye, was the main type of porosity formed in the high hydrogen content castings. However the image analysis results in the high purity aluminium experiment shown in Table 4.31 suggest that hydrogen gas is not the only factor responsible for increasing porosity in the castings because, although the hydrogen content in the molten aluminium was high (0.4 ml/100g metal), the overall porosity area was only 0.3%, and there was not the presence of large gas porosity defects were absent, compared to the results of the other aluminium alloys with a similarly high hydrogen content where the area of porosity was 3.5 %. The formation of porosity will

be further discussed in the next section where the role of oxide film defects will be considered (section 5.4).

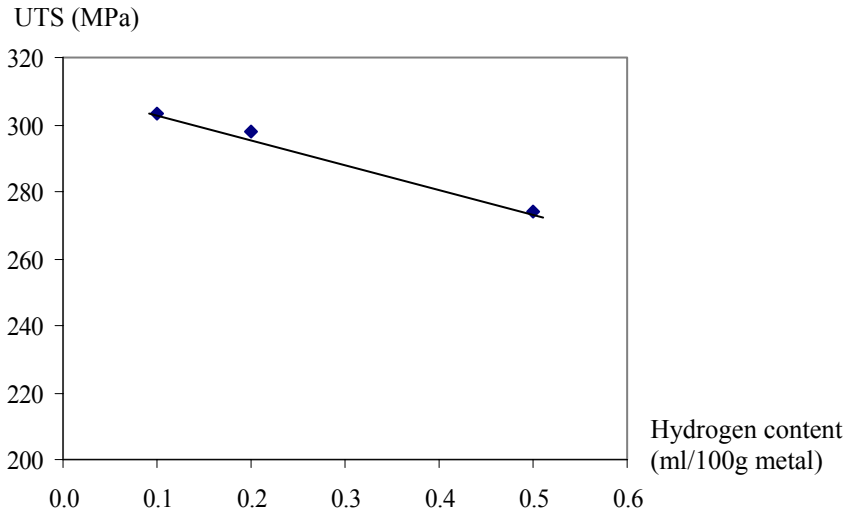
Shrinkage porosity was not often found in the castings obtained from the test bar mould. This suggests that the mould used in the experiment to examine the effect of shrinkage porosity on the tensile properties (section 4.2) did not generate much shrinkage porosity as was expected. However, shrinkage porosity was produced in the cast plates, specially designed to determine the effect of shrinkage porosity, and most shrinkage porosity was located in the central area of the plate, the last zone to solidify (see Figures 4.126, 4.127, 4.129 and 4.132). A combination of shrinkage porosity and gas porosity was present when the hydrogen content was increased to 0.3 ml/100g metal in the high oxide film plate casting (see Figure 4.128). The image shows that gas porosity was distributed in every section of the cast plate whilst shrinkage porosity was usually located in the central area of the casting. This suggests that, during solidification, gas porosity was formed first by the precipitation dissolved hydrogen and shrinkage porosity would be formed at the last stage due to the incomplete feeding of liquid metal which flow to compensate for the liquid/solid volume change.

5.3.1 Effect of porosity on tensile properties of the casting

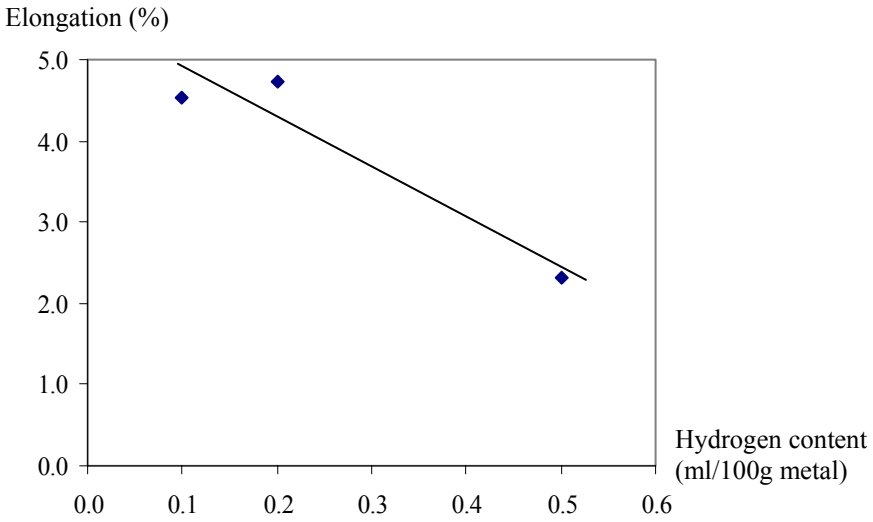
Porosity defects are widely known to negatively influence tensile properties because they act as material discontinuities and result in a reduction in load bearing area [Caceres and Selling 1996]. As previously mentioned, the increase in hydrogen content in alloys resulted in an increase in the area of porosity, and therefore hydrogen gas in the casting directly influences the tensile properties of the castings. The Pareto diagrams in Figure 4.1 showed that the effect of increasing hydrogen gas from 0.1 to 0.45 ml/100g metal on the UTS and elongation resulted in a reduction of about 20 MPa and 0.7% respectively. The effect of porosity defects caused by hydrogen gas on tensile properties appeared to be the least detrimental in this experiment, compared to Fe-rich phase and oxide film defects. The physical characteristics of gas porosity, therefore, influenced the tensile properties less than the brittle, platelet-like, β-Al_5FeSi phase and double oxide film defects.

Figures 5.4a and 5.4b show results of mean UTS and mean elongation obtained from filtered castings with the same iron content of 0.1 wt% (see Tables 4.1, 4.2, 4.13 and 4.14). It can be seen that the mean UTS of castings decreased from about 305 to 295 and 278 MPa when the hydrogen gas content increased from 0.1 to 0.2 and 0.5 ml/100g metal respectively. For elongation, the castings that contained 0.1 and 0.2 ml/100g hydrogen had elongations at the same level of about 4.5%. However, when the hydrogen content increased to 0.5 ml/100g metal, the elongation of the castings significantly decreased to about 2.3%. This suggested that the microporosity that occurred at the low hydrogen contents only slightly affected elongation. The decrease in tensile properties was greater and more noticeable when the hydrogen content was increased until large gas porosity, (normally with sizes greater than 100 μm), was introduced.

The results obtained from this study support the suggestions of other authors [Herrera and Kondic, 1977 and Surappa et el., 1986] that reduction in tensile properties does not relate to the area of porosity but a better correlation can be obtained with the length of porosity. In addition, it supports the research of Griffin et al. [2003] who studied porosity defects found on the fracture surfaces of tensile test bars and concluded that the UTS of aluminium alloys significantly decreased when porosity with a diameter of greater than 250 μm was present.



(a)



(b)

Figure 5.4 Effect of hydrogen gas on tensile property of cast Al-Si-Mg alloy

5.4 Interaction between oxide film and porosity defects

The interactions between the three microstructural defects, oxide films, Fe-rich phase and porosity, were examined. The results suggested that the greatest interaction was the relationship between oxide film and porosity, since the SEM images showed that more than 90% of porosity, both gas porosity and shrinkage porosity, observed in all experimental castings contained oxide films on the internal surface of the pores (see Figures 4.44, 4.46, 4.78, 4.103, 4,105, 4.107, 4.117, 4.119, 4.130, 4.133 and 4,137). The Pareto diagrams obtained from image analysis shown in Figures 4.63a, 4.80a and 4.101a also showed that increasing oxide film content (column C) in the castings influenced the presence of porosity by increasing the area of porosity by about 0.2%. This suggests that oxide films play an important role in the formation of porosity in cast aluminium alloys.

Many authors have studied the nucleation of pores during solidification using theoretical, mathematical and analytical approaches [Fisher 1948, Pehlke 1992, Kato 1999, Tayler 1999, Campbell 2000, 2003, Lee et al 2001]. The classical theory explaining the nucleation of porosity was proposed by Fisher [1948], who suggested that a pore would

nucleate either homogeneously or heterogeneously during solidification, and that the pressure required for the nucleation could be estimated by Equations 2.5 and 2.6 respectively. This theory showed that nucleation was unlikely to occur in practice since the pressures required for both homogeneous and heterogeneous nucleation were extremely high, of the order of about 31,000 atm and 1,500 atm respectively [Campbell 2000, Lee et al 2001].

Since nucleation of pore in the cast aluminium alloys was difficult to occur in practice, the other theories have been researched to describe the formation of the pore. Campbell [2003] suggested that the perfect sites for the formation of porosity were double oxide film defects, since double oxide films contain a nonsoluble gas between the two dry sides of the films, which would act as an existing pore entrained in the melt. These existing pores could grow further by the diffusion of hydrogen into the pore, or by opening under the pressure developed by shrinkage. This mechanism suggests that high pressures of gas or shrinkage are not required for nucleation, it could occur easily, and is likely to occur in practice.

Kato [1999] reported that non-wetted surfaces on surfaces of oxide inclusions in the liquid metal might be sites for nucleation and explain oxide-related porosity. He suggested that the contact angle between Al_2O_3 and liquid Al was 150^o, and that pores were formed heterogeneously on the surfaces of oxides when the pressure in the liquid at the solid-liquid interface was about 2.7 atm. However, it is important, in the context, to realise that surface oxide film can only be entrained as a double oxide film when introduced into a liquid metal. Even if a thick oxide was to be pushed into a melt, in an effort to create a single immersed inclusion, the surface film on the liquid metal would be pulled down either side of the introduced oxide and surround it by two, non-wetting surface films as shown in Figure 5.3 [Dignam 1962, Fox and Campbell 2000]. Therefore the oxides found in Kato's study were probably not a site for heterogeneous nucleation but were double oxide films that acted as initiators of pores in the castings.

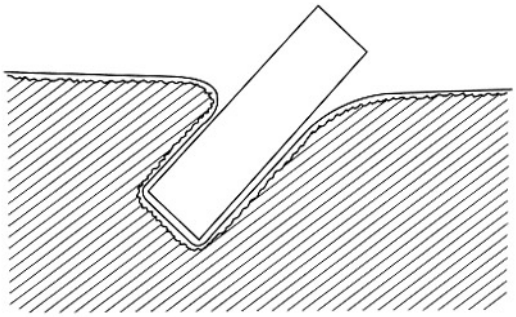


Figure 5.5 Schematic view of the introduction of an inclusion into the melt.

It is known that double oxide film defects are almost unavoidable in practice. In these experiments, even castings having filters were found to contain oxide films, (Figures 4.20, 4.23, 4.109, 4.111), every casting was therefore likely to contain the initiator of porosity. Moreover the negligible force involved in the formation of the pore by the opening of double oxide films suggested that it is the easiest mechanism for the formation of pores during solidification compared to other theories. The results obtained from this study have been examined to determine whether they support the suggestion that double oxide film defects are the initiator of porosity defects in castings.

The presence of oxide films at the internal surface of more than 90% of the observed pores was strong evidence that porosity formed by double oxide film defects. According to this mechanism, porosity cannot form without an oxide film defect, the presence of an oxide film therefore is expected to be found in all pores. The SEM results show that the pores, which did not contained oxide films, were microporosity (classified as a less than 100 μm in size) as shown in Figure 4.48. It, however, is not clear whether porosity did not initiate from double oxide film defects or the samples were sectioned the part of pores that did not contained oxide films. Moreover, the measurement of oxygen using EDX on a very thin oxide film or at the surface of deep pore might influence the analysis.

Another expectation of the formation pores by this mechanism was that the presence of pores should increase with an increase in oxide film defects, i.e. with an increase in surface turbulence. This assumption was support by the image analysis results, which

shows that increasing oxide film content led to a direct increase in the number of pores in every experiment. For example, the Pareto diagrams in Figures 4.63b, and 4.80b showed that increased oxide film content in the first and second experiment increased the number of pores by about 14% and 10% respectively. Tables 4.31 and 4.32 showed that, in high purity aluminium and high purity Al-Si alloy experiments, an increase in oxide film content resulted in an increase in the number or pores of about 40% and 60% respectively. In the plate casting examining the effect of oxide film on the formation of shrinkage porosity, the same behaviour of the results was found since Tables 4.36, 4.37 and 4.38 showed that the mean number of pores increased with an increase in oxide film content.

The action of oxide film defects as an initiator of the pores was therefore likely to be the main mechanism of the formation of porosity, both gas porosity and shrinkage porosity, in the castings. In this mechanism, porosity in casting is not caused by nucleation but is only a growth state. According to the equilibrium pressure estimated by Equation 2.8, the growth of a pore will depend on two main causes, the pressure due to dissolved gases and the pressure created by shrinkage. If there is enough feeding, the growth of the pore will be controlled by only dissolved hydrogen gas and become a gas porosity defect in the casting. Shrinkage porosity will be formed in the case of poor feeding of castings. The formation of gas porosity and shrinkage will be separately discussed in the following.

5.4.1 Gas porosity

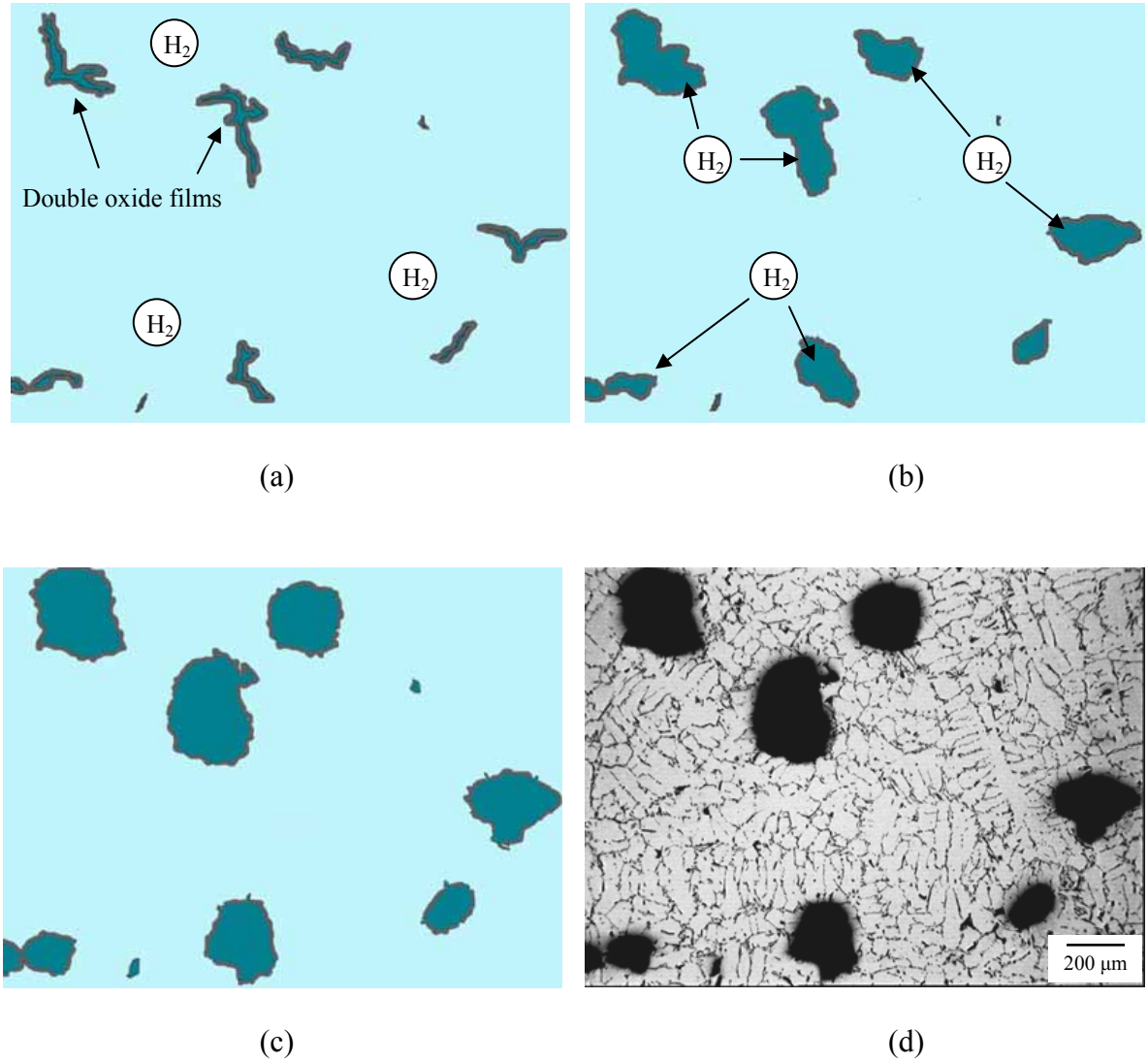
Beside oxide film defects, the factor that influences the presence of gas porosity in cast Al alloys is hydrogen gas. The Pareto diagram obtained from the image analysis results of the experiment examining the interaction between Fe-rich phase, gas porosity and oxide film (Figure 4.63) showed that hydrogen had the greatest effect on the presence of gas porosity by increasing porosity area and the size of pores by about 3.5% and 1600 μm^2 respectively. Possible mechanisms of gas porosity formation by the inflation of a double oxide film in aluminium alloy castings have been shown in Figures 5.6a to 5.6c.

Firstly, double oxide film defects are introduced into the melt by surface turbulence during the mould filling process. These defects contain some air, (i.e. O_2, N_2 and Ar), between the two dry sides of the films and act as a void in the melt. Double oxide films will be thickened by further formation of oxide and nitride, and might be sealed if all the gases in the interior are consumed. Although the oxide film is not permeable to diffusion by aluminium and oxygen, a thickening of the oxide film results from the transportation of oxygen through continuous pathways [Agema and Fray 1989]. The pathways in the oxide films can be cracks, zones of loose structure inherent in the films, or formed by the volume change associated with conversion of metal to oxide. Gas dissolved in the melt (i.e. hydrogen) can also diffuse into the double oxide film defects through these pathways.

During solidification, the solubility of hydrogen decreases with decreasing temperature therefore it is rejected by the growing solid and diffuses in the remaining liquid or becomes supersaturated in the solid. Since it cannot be nucleated, (either homogeneously or heterogeneously), porosity will be formed only when the hydrogen meets a double oxide film, which already acts as an existing pore. The diffusion of hydrogen will further expand the pore, inflating any compacted, folded oxide films, causing them to open and form pores in the castings. It can be seen that the expansion of double oxide films directly depends on the hydrogen content in the liquid metal. In high hydrogen content castings, the folded oxide films tend to be opened sufficiently to take the form of spherical bubbles and become the large gas porosity shown in Figure 5.6d.

Figure 5.7 shows the area of porosity of the castings with different hydrogen contents, obtained by image analysis, for all experimental results. It can be seen that the area of porosity increases with increasing hydrogen gas content. Therefore the best way to solve the gas porosity problem would be to reduce oxide film defects and hydrogen gas together. Figure 5.7 also shows that increased oxide film content influenced the presence of gas porosity by increasing the porosity area of the castings. This supports the formation of porosity by oxide films because increased oxide films resulted in an increase in number of initiators of pores. As mentioned that dissolved hydrogen is likely to become supersaturate in the solid if there is no double oxide film defects, overall

porosity in the casting therefore was expected to be greater in the high oxide film content castings.



(a) (b)

(c) (d)

Figure 5.6 Sketches of gas porosity formation in the cast aluminium alloy showing (a) the presence of double oxide film defects in the melt, (b) dissolved hydrogen diffusing into double oxide film defects, (c) the inflation of double oxide film defects causing gas porosity, and (d) a micrograph of gas porosity in a casting.

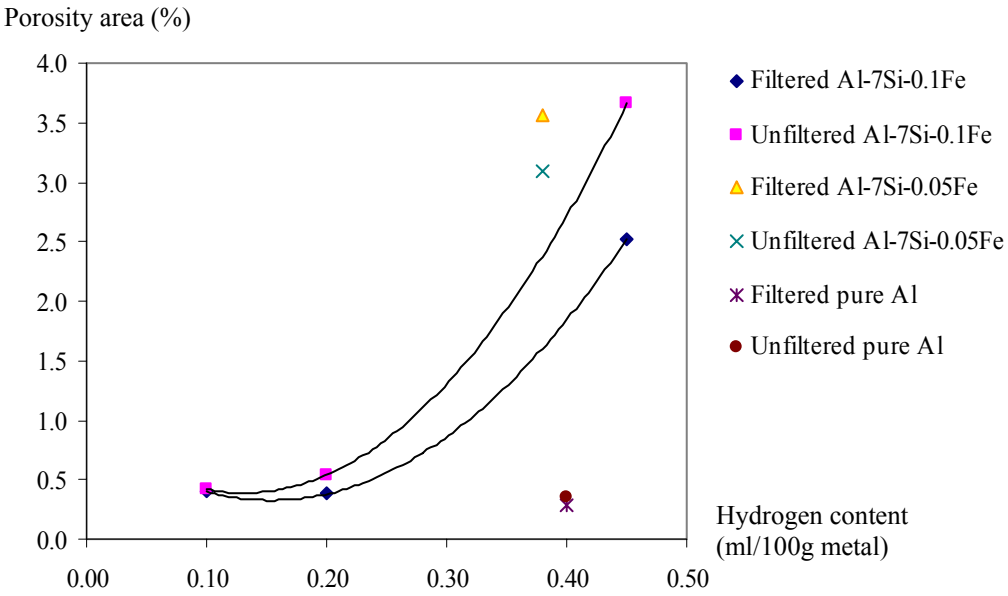


Figure 5.7 Graph of porosity area versus hydrogen content obtained from all experimental combinations.

There were some results in the diagram that disagreed with the inflating double oxide film theory, for example; the porosity area obtained from the high purity aluminium, (shown in Table 4.31), was not as high as was expected (about 0.3 %), although the hydrogen content was high (0.4 ml/100g metal), and the presence of oxide films were observed in SEM images (Figures 4.103, 4.105, 4.107, 4.109, 4.111 and 4.113). This may be because of several possible reasons. The First explanation involves the morphology of the oxide films. It has been reported by many authors that the oxide films formed at the surface of pure aluminium are amorphous and this kind of film is impermeable (or less permeable) to hydrogen [Silva and Talbot 1988, Impey et al. 1988]. Figures 4.104, 4.106, 4.108, 4.110 and 4.112 show EDX analysis results of oxide films produced in a high purity aluminium casting. The small amount of oxygen measured suggests that the oxide film observed was a young oxide film, which was thin and newly formed in the mould filling, and likely to be amorphous. This therefore prevented the rapid diffusion of hydrogen into a double oxide film defect in the casting. Secondly, the solidification range in pure aluminium is very narrow so the hydrogen has much less time for diffusion into double oxide films and might be supersaturated in the solid. The latter alternative is supported by the image analysis results shown in Table 4.32 because,

when the same hydrogen content was applied to a high purity Al-Si alloy, with the same kind of oxide film in the casting but has a longer solidification range, a ten times greater area of porosity was obtained compared to the cast pure aluminium. Therefore the solidification time of the castings is another factor that influences the porosity formation in aluminium alloy castings.

The results of the porosity area obtained from the high purity Al-7Si alloys, however, contradicted the other casting since the low oxide film casting had greater porosity area than the high oxide film casting, by about 0.5%. The image analysis results in Table 4.32 show that the high oxide film casting had a higher number density of pores than the low oxide film casting. It can be seen in the high oxide film casting that the number of pores increased by about 63% compared to the low oxide film casting and porosity was mainly formed as microporosity with the mean pore length of about 15 μm. The presence of numbers of small pores therefore might influence the accuracy of pore determining since image analysis used in this experiment did not include the small pores which had the length less than 10 μm. The other reason is that the diffusion of hydrogen into oxide film defects might be restricted in someway. The porosity area of the high oxide film casting might increase if there was the presence of other particles in the casting, for example, Fe-rich phase.

5.4.2 Shrinkage porosity

Many results in this study suggested that shrinkage had an effect on the formation of porosity in the cast aluminium alloys. Figure 4.142 obtained from the cast plate shows that the main defect that occurred in these castings was shrinkage porosity, that formed at the centre of the plates, as the greatest shrinkage was expected to be produced in this area. As with gas porosity formation, the initiators of shrinkage porosity are double oxide films. This was confirmed by the SEM images of shrinkage pores that showed more than 90% of pore contained oxide film at the internal surface of pores (e.g. Figures 4.130 and 4.133). The Pareto diagrams obtained from the second experiment (Figures 4.80c and 4.101c) also showed an interaction between oxide film and shrinkage (column AB) that influenced the size of porosity by decreasing pores size by about 10% and 20% in the

high Fe content and the low Fe content castings respectively. Therefore oxide film defects and shrinkage play a part in the presence of shrinkage porosity in the cast Al-Si-Mg alloys.

Figures 5.8a to 5.8c explain the formation of shrinkage porosity in cast aluminium alloys. Shrinkage porosity is formed during solidification because of a difference in the specific volumes of liquid and solid metal. When the first regions of the casting solidified, this shrinkage would be fed by drawing liquid from neighbouring areas and the ability to draw this liquid metal will become more difficult due to the presence of an interdendritic network of solid metal which results in a reduction in the feeding channels. The negative pressure from shrinkage helps a double oxide film defect or an existing pore, to grow. The shrinkage porosity, therefore, is formed in an irregular shape in the interdendritic region and usually observed as a group of connected microporosity in the cross sections of castings, as shown in Figure 5.8d.

The mechanism of shrinkage porosity formation suggests that oxide film defects are necessary as the initiators of pores, therefore the number of shrinkage pores and pore area, therefore, should be greater if oxide film content in the casting increases. However the distribution of pore area in 32 sections obtained from image analysis results (shown in Figure 4.142a) showed that increased oxide film content in the medium oxide film casting produced no difference in the distribution of the number of pores and pore area compared to the low oxide film casting. In the case of the high oxide film casting, its distribution could not be compared with the others because the presence of porosity in the casting was caused by the combination of shrinkage and hydrogen gas. However the pore area of the high oxide film casting, was estimated, at the same hydrogen content of the low and medium castings using the relationship between the pore area and the hydrogen content obtained from the cast Al-7Si-0.1Fe alloys obtained from in the first experiment (see Figure 5.7).

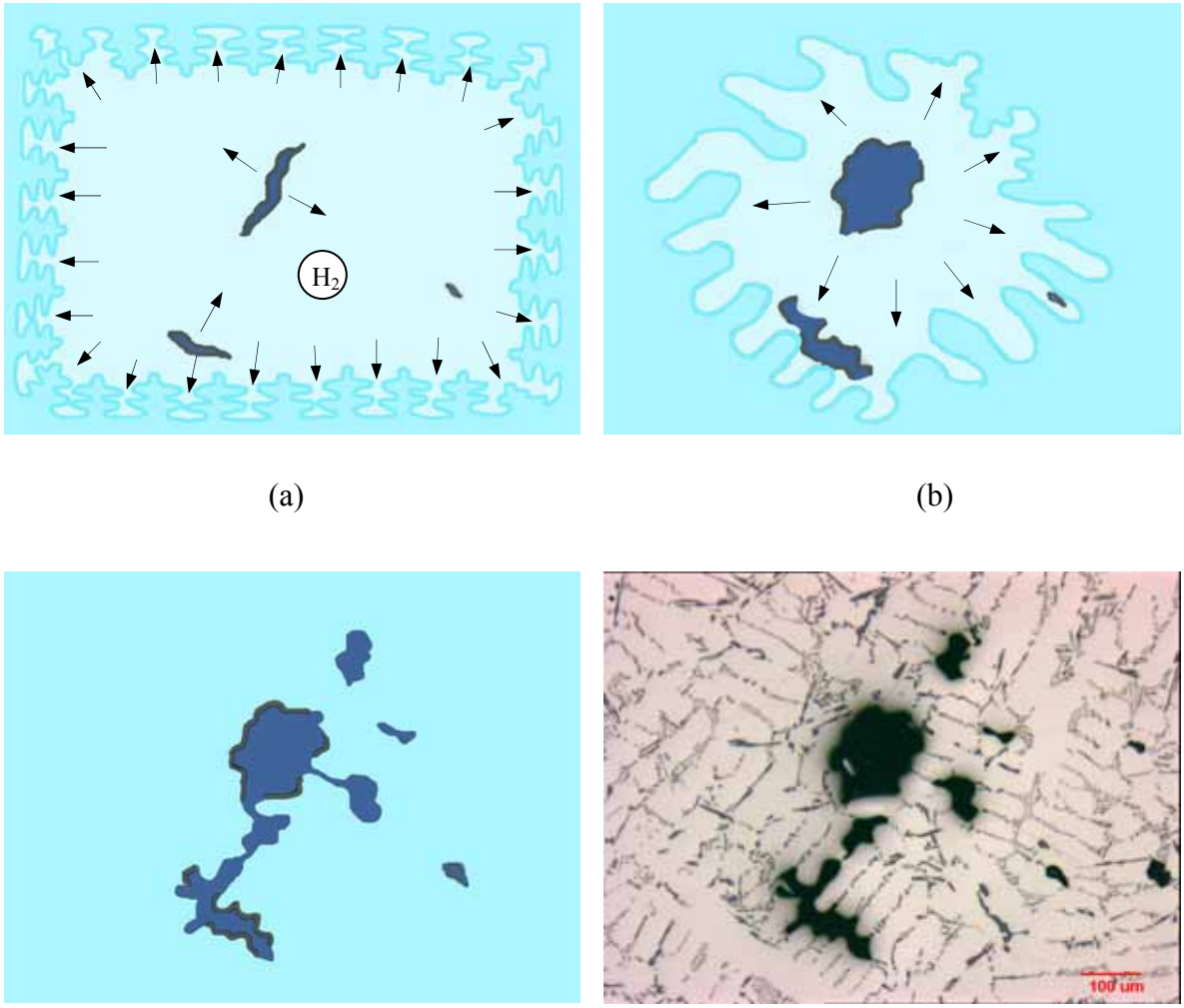


Figure 5.8 Sketches of shrinkage porosity formation in the cast aluminium alloy showing (a) the molten alloy contained double oxide film defects, (b) volumetric shrinkage occurred during solidification, (c) the expansion of double oxide film causing by the negative pressure of shrinkage and (d) a micrograph of shrinkage porosity in a casting.

Figure 5.9 shows the new distribution of pore area obtained from 32 sections of the low, medium and high oxide film castings at the same hydrogen content (0.2 ml/100g metal). The diagrams show that increasing oxide film content appeared to have no significant effect on the presence of shrinkage porosity since all castings had similar pore area distribution. The SEM images showed there was about 10% of shrinkage porosity that

had no evidence of the presence of oxide film in the pores. This might be due to shrinkage porosity could be formed without oxide film defects. Shrinkage porosity, as mentioned, is formed with an irregular shape that was usually observed as a group of microporosity in the cross sections. Therefore the numbers of shrinkage pores might initiate from only one oxide film defect. This suggests that the pores, which oxide film was not detected, might be formed by double oxide film but the samples were sectioned the parted of pores that did not contained oxide films.

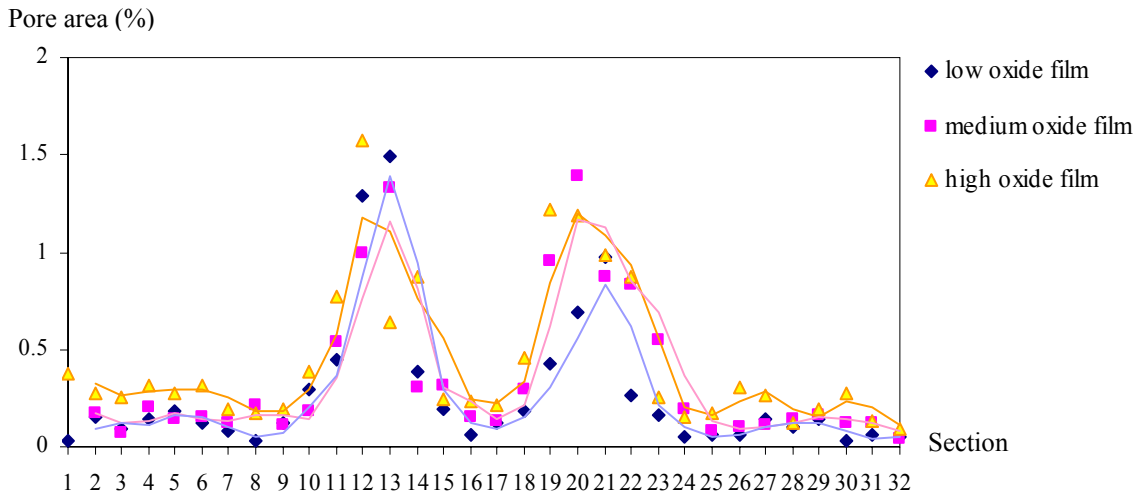


Figure 5.9 The distribution plots of porosity data obtained from 3 type castings (hydrogen content of 0.2 ml/100g metal)

In summary, this study revealed interactions between oxide films and porosity in aluminium alloy castings, and that double oxide films are the key to the mechanism by acting as pore initiators in the casting. Hydrogen gas also plays an important role by diffusing into these defects, inflating them to become porosity in the castings, while in the case of poor feeding, the negative pressure caused by shrinkage will control the growth of double oxide film defects. Generally, the growth of double oxide film defects will be controlled by the combination of shrinkage and dissolved hydrogen since hydrogen gas would be rejected from the melt during solidification and diffuse into the

entrained oxide films. The pressure of dissolved hydrogen and the negative pressure created by shrinkage will help the pore to grow easier. The other factor that might influence the formation of porosity is solidification time, which will allow more time for dissolved hydrogen to inflate the pore.

5.5 Interaction between oxide film defects and Fe-rich phases

The results in this study showed that oxide films had an interaction with Fe-rich intermetallic phases since they were one of the nucleation sites of Fe-rich phases. Figures 4.26, 4.28, 4.87 and 4.89 show SEM and back-scattered images obtained from the fracture surfaces, in which it can be clearly seen (through the thin oxide film) that β-Al_5FeSi phases precipitated onto the wetted side of oxide films. A relationship between oxide film and Fe-rich phase was also found in microstructures of the castings, for example, Figure 4.100 shows crack-like porosity, which actually was an entrained oxide film, associated with the Fe-rich phases in the interdendritic region.

Many authors have reported evidence for the nucleation of Fe-rich phases onto oxide films [Leoni and Fommei 1976, Narayanan et al. 1994, Doty et al. 2000]. Cao and Campbell [2003] claimed that the oxide film was a favourite nucleation site and that Fe-rich phase might not be able to precipitate at all in aluminium castings without the presence of oxide films. They evaluated the effect of oxide films on the nucleation of Fe-rich phases by examining their relative planar disregistry and claimed that MgO, $MgO.Al_2O_3$, γ-Al_2O_3 and α-Al_2O_3 could be good substrates for the nucleation and growth of α-Fe phase (primary or script type) because of the similarity in lattice parameter between them. If the disregistry between oxides and β-Al_5FeSi phase was calculated, this might explain why oxide films act as a good nucleation site for β-Al_5FeSi phases. Cao and Campbell also found cracks along the centre of the Fe-rich phases (see Figure 2.15) and believed that it was caused by double oxide film defects. They suggested that the two halves of the Fe-rich phase were separate particles that nucleated independently on the wetted sides of the double oxide films and grew along the oxide film, causing it to straighten. However, the microstructural examination in this study revealed no crack in

the Fe-rich phase as they suggested, and there was no evidence of oxide films associated with the cracks in the Fe-rich phases observed on the fracture surfaces. Cao and Campbell held the melt at the precipitation temperature of Fe-rich phase (about 600 ^{o}C) for a long time, which might have helped the nucleation and growth of Fe-rich phase on oxide films. On the other hand, the cracks observed in their work may not be double oxide films defects but occurred later during the polishing and preparation of the samples.

The microstructures examined in this study showed that oxide film was not the only nucleation site during solidification but that Fe-rich phase could also nucleate elsewhere, such as the aluminium matrix and/or boundary as shown in Figures 4.38, 4.42 and 4.98. If the oxide film was the preferred substrate for the nucleation of Fe-rich phase, then effects on the presence of the Fe-rich phase should be found when the oxide film content was increased. However, image analysis results carried out on ten samples of the high Fe castings (0.5 wt% Fe) from the first experiment showed that the mean size (30 μm^2) and number of Fe-rich phase (540 phases/mm^2) in both the low and high oxide film castings was similar. There was no difference in the distribution of Fe-rich phase in both the low and high oxide film castings.

It has been suggested that, since β-Al_5FeSi phase is monoclinic and grows in a plate-like fashion [Brandes and Brook 1992], the Fe-rich phase might grow along the surface of crumpled oxide films, which had been compacted by bulk turbulence and were relatively harmless, and straighten them. This would cause one surface of the double oxide film defect to be separated from the other surface, opening a gap between them to appear as crack-like porosity in the casting that resulted in a decrease in tensile properties. Several SEM images obtained from the fracture surfaces contradict this suggestion, since they showed that β-Al_5FeSi platelets appeared to grow along the wrinkles of oxide films (see Figures 4.87 and 4.89). However the straightening mechanism might be possible if large Fe-rich phases nucleated onto a small double oxide film (i.e., a young oxide film), having more deformability and flexibility, as shown in Figure 4.59.

The straightening of folded oxide films by Fe-rich phases reflects the effect of Fe-rich phase on the reliability of the castings since the results obtained from the Weibull plots

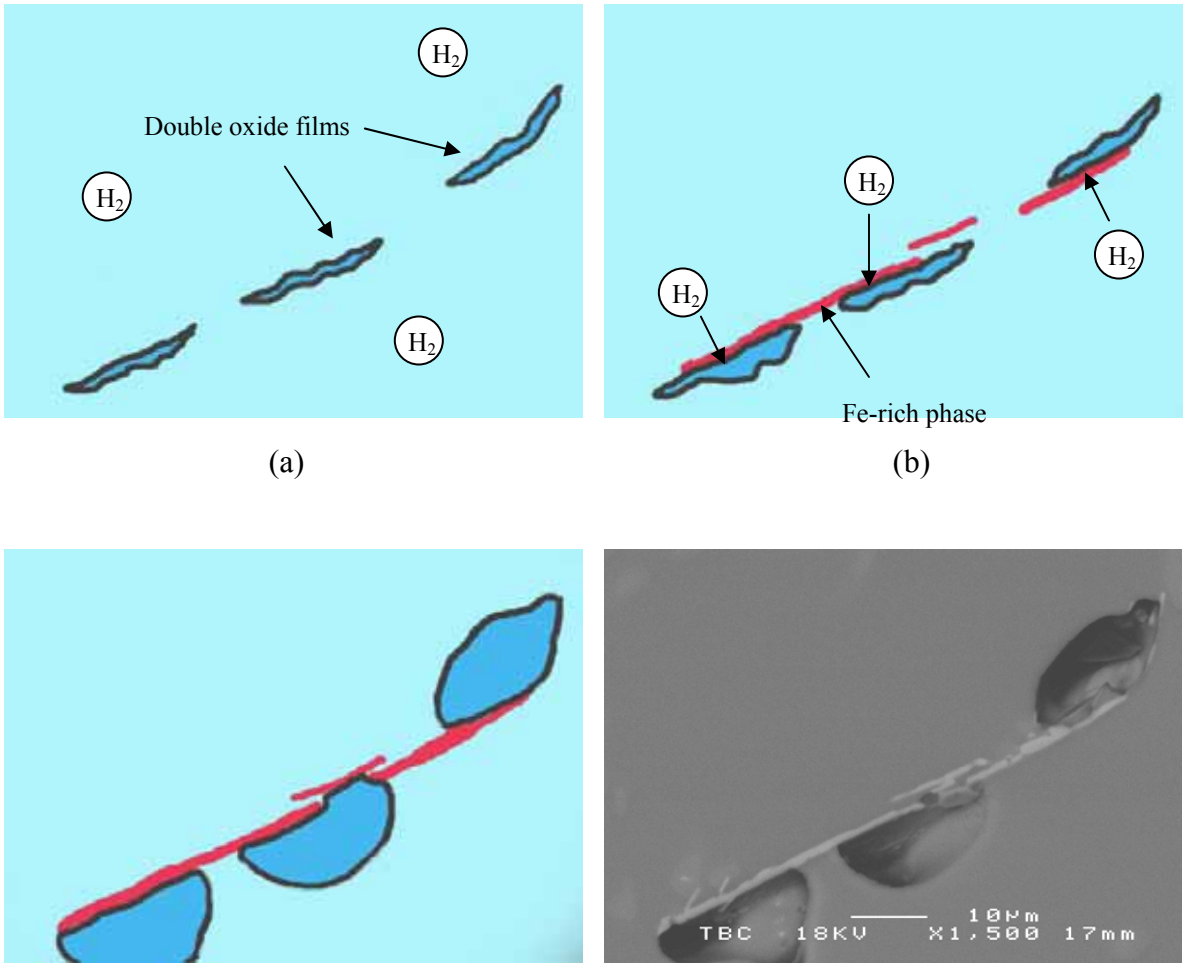
shown in Figures 4.95 and 4.96 show that increasing Fe content to 1.1 wt% resulted in not only a reduction in UTS and elongation but also a significant reduction in Weibull modulus compared to the low Fe content castings (see Figures 4.31b, 4.32b, 4.73b and 4.74b). As the Fe-rich phases had the same size and amount in the low and high oxide film content castings, the tensile properties of test bars should be the same and the distribution of tensile properties should not be affected if the failure was mainly caused by Fe-rich phase. It was clearly shown in the Pareto diagrams of Weibull modulus (Figures 4.34a and 4.34b) that oxide film defects had the greatest effect on the production of unreliable properties in the casting (column C). This therefore suggested that the reduction in Weibull modulus of the high Fe content casting might be caused by the effect of oxide film defects that were straighten and unfolded by the nucleation of Fe-rich phase onto them. Or the effect could be explained by the nucleation of Fe-rich phase on the oxide films alone, resulting in a scatter of defect sizes and positions, and hence a scatter in properties.

5.6 Interactions between oxide films, Fe-rich phases and porosity defects

The interaction between Fe-rich phase and oxide film also involves an interaction between Fe-rich phase and porosity since, as mentioned in the previous section, double oxide films act as initiators of porosity formation in aluminium alloy castings. As shown in the Pareto diagram obtained from the image analysis results (see Figure 4.63), Fe-rich phases (column A) appeared to markedly influence the presence of porosity because increasing Fe content resulted in an increase in the number density of pores in the castings of about 1500 pore/cm^2. Moreover SEM images showed that there were many pores associated with Fe-rich phases, particularly β-Al_5FeSi phases, as shown in Figures 4.56, 4.57, 4.59, and 4.61. Since the formation of porosity has been interpreted as requiring double oxide films as the initiator for the pore, these three defects should have interrelationships between them, which would influence the tensile properties of aluminium alloy castings and the reproducibility of properties as shown in the Pareto diagrams (e.g., column ABC in Figures 4.1 and 4.34).

The other evidence that shows an influence of Fe-rich on the presence of porosity in the cast aluminium alloys was the image analysis results obtained from the first experiment (Table 4.7). It can be seen that, in the high oxide film and high hydrogen content castings, the number of pores dramatically increased from about 1500 to 3600 pore/cm^2 when the Fe content in the castings was increased about 0.45 wt%. Some authors claimed that the β-Al_5FeSi phase might act as pore nucleation sites since Fe content influenced the amount of porosity that formed in a casting [Roy et al. 1996]. This assumption is unlikely to occur in practice due to the good wetting or the small contact angle of the liquid on the Fe-rich phases and therefore the extremely high pressures required for heterogeneous nucleation of porosity. Other authors have pointed to the possibility of heterogeneous nucleation of pores in crevices in inclusions, but Fisher showed that heterogeneous nucleation on a plane surface was unlikely. Since β-Al_5FeSi phase forms as a platelet, then Fisher's argument about the unlikely possibility of nucleation on a plane surface is more relevant than the suggestion of pore nucleation in a crevice. The increase in porosity can be explained by the evidences and results obtained from this study by two possible mechanisms.

First, the Fe-rich phase enhances the diffusion of hydrogen into the entrained oxide film. This mechanism can be explained by Figure 5.10 as follows; to begin with, young oxide films are formed by surface turbulence produced during mould filling and, in the case of Figure 5.10, three double oxide films, or perhaps a young oxide film that broke into three double oxide film defects, is entrained into the melt as shown in Figure 5.10a. In the castings that do not contain Fe, hydrogen is thought to slowly diffuse into the entrained oxide films through pathways in the films, (which were mentioned in section 5.4.1), while the young double oxide films tend to be sealed by further oxidation consuming the oxygen inside the oxide film interior. The presence of Fe-rich phase may help the formation of porosity to be easier since it can nucleate on the wetted-side of the double oxide film and create a crack in the oxide film allowing hydrogen to diffuse into the interior of the double oxide film, though the Fe-rich phase, causing it to inflate into a pore (see Figures 5.10b and 5.10c).



(a) (b)

(c) (d)

Figure 5.10 Sketches of porosity formation in the cast aluminium alloy containing Fe-rich phases showing (a) double oxide film defects in the melt, (b) the nucleation of Fe-rich phases on the wetted side of double oxide film, (c) the inflation of oxide film causing by the diffusion of hydrogen through Fe-rich phases, and (d) a micrograph of porosity associated with Fe-rich phases and oxide films.

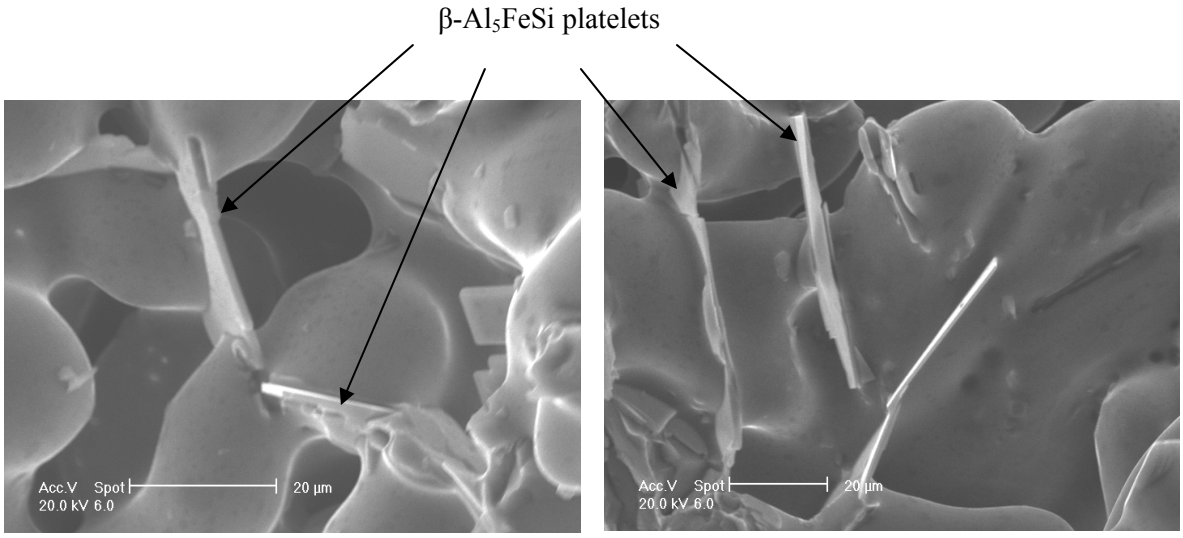
A related explanation is that Fe-rich phase nucleated on the oxide film can channel hydrogen through the oxide into the interior. The point where the β-Al_5FeSi phase grows on the oxide film must be the thinnest region of the film as this is where the oxide is insulated from the aluminium melt. Elsewhere the oxide film in contact with the melt and can continue to grow and thicken. Estimates of the solubility of hydrogen in Fe_3Al show

that it is much greater than the solubility of hydrogen in aluminium [Xu and McLellan 1997] and the β-Al_5FeSi phase may have similar properties. During solidification hydrogen can sink into the β-Al_5FeSi phase nucleated on the oxide film where now the driving force for diffusion through the adjacent film would be greater than elsewhere around the double oxide film defect, where the lower hydrogen content of the melt makes diffusion through the oxide film less likely. In fact, the act of nucleation of the β-Al_5FeSi phase on the oxide film may disrupt its structure, somehow, rendering it permeable to hydrogen. As a consequence, double oxide films upon which β-Al_5FeSi phase particles nucleate may preferentially inflate to form the observed porosity. Pores will stop growing when the local hydrogen content has declined, or they touch the next Fe-rich phase to become microporosity in the castings as shown in Figure 5.10d. This is the reason why the porosity in high Fe content castings tends to form with a smaller size while having a greater pore density.

The second mechanism is that the Fe-rich phase causes physical restrictions to the movement of compensatory feed liquid. The image analysis results obtained from the high oxide film and high shrinkage casting in the second experiment (as shown in Tables 4.18 and 4.27) showed that the number of pores was increased from about 1700 to 2200 pore/cm^2 with an increased Fe content in the castings from 0.1 to 1.1 wt%. The SEM images of the shrinkage porosity observed in this study showed Fe-rich phases associated with oxide film at the edges of pores, for example, Figures 4.59 and 4.61 and 4.91. The explanation of these might be due to the large β-Al_5FeSi platelets acted as a barrier to the flow of feed metal causing a decrease in the permeability of the interdendritic network. During solidification of Al-Si-Mg alloys, the β-Al_5FeSi phase nucleates earlier at the temperatures shown in Table 2.4. When it grows and obstructs the flow of feed metal, solidification contraction could then cause local failure of the liquid, leading to the presence of microporosity in the interdendritic regions or shrinkage porosity as shown in Figure 5.11. As previously mentioned in the section about the interaction between oxide film and porosity (section 5.4), the shrinkage porosity is known to initiate from double oxide film defects, which suggests an interaction between Fe-rich phase, oxide film and shrinkage porosity in that Fe-rich phases, nucleated on the wetted sides of double oxide films, lead to localised shrinkage which may help the double oxide film defects to

become a pore. Hence the presence of large β-Al_5FeSi phase particles was found to reduce the pore size while increasing the pore number density.

Several authors proposed the theory that the long and thick platelets of β-Al_5FeSi phases may restrict feeding [Otte et al. 1999, Taylor et al. 1999, Villenerve et al. 2001]. However they reported that the theory was not capable of explaining all of their experimental results, since they could not remove the difficulty of explaining how the pores nucleated in the first place. However, their theory can be easily explained by the opening or inflation of double oxide films, because a double oxide film is an initiator of either gas porosity or shrinkage porosity in the casting.



(a) (b)

Figure 5.11 The scanning electron micrographs obtained from Al-7Si-0.2Mg-1.1Fe alloy showing the large β-Al_5FeSi platelets blocking feeding channels between solidifying dendrites.

To summarise, the Fe-rich phase (particularly β-Al_5FeSi phase) produced an effect on the presence of porosity in the casting by increasing the number of pores, as shown in the Pareto diagram obtained from the image analysis results (Figure 4.60b). The interrelationship between Fe-rich phase and porosity might be explained with two

possible mechanisms. Firstly, Fe-rich phases nucleate on the wetted side of entrained oxide films and act as channels for hydrogen to diffuse into the oxide film interior, causing gas porosity. Secondly, large β-Al_5FeSi phases that nucleated on oxide films during solidification block feeding channels between solidifying dendrites causing the double oxide film defects to open out into interdendritic shrinkage porosity.

5.7 Summary

The three common defects usually found in Al-Si-Mg alloy castings, (double oxide films, Fe-rich phase and porosity), were investigated in this study. The tensile properties results showed that double oxide films could produce an effect on UTS and elongation of up to 150 MPa and 2% respectively. Oxide film defects also influenced the reliability of the casting by increasing the scatter of tensile property data. The most frequently observed Fe-rich phase observed in this study was β-Al_5FeSi phase. Its brittle characteristic and large platelet morphology affected the tensile properties of castings by acting as a crack initiator. Increasing Fe content from 0.1 wt% to 1.1 wt% in this study resulted in a reduction in UTS and elongation by about 70 MPa and 4% respectively. Porosity defects normally observed in the casting were gas porosity and shrinkage porosity. The results revealed that increasing hydrogen content to 0.5 ml/100g metal caused the presence of gas porosity that decreased the tensile properties by about 20 MPa and 1.5% respectively. Thus, in order of importance on UTS and elongation, the defects can be ranked as Fe-rich phase, oxide film defect and porosity, while for their effect on reproducibility of properties they can be ranked as oxide film defects, Fe-rich phase and porosity.

Apart from direct effects on tensile properties produced by each defect, this study revealed the interactions between these defects that additionally influence the properties of castings. The formation of porosity in the castings was the most important interaction between oxide film and porosity found. The micrographs obtained from the microstructures showed that more than 90% of porosity observed in this study contained oxide films at their internal surface. This explains the formation of porosity in aluminium alloy castings in that it began with a double oxide film which contained some

atmosphere inside. Hydrogen diffused into the double oxide film defects and inflated them into gas porosity. The pressure from shrinkage due to the density difference during solidification also resulted in the growth of double oxide films to become shrinkage porosity in the castings. Fe-rich phase appears to enhance the formation of pores, and the Fe-rich phase nucleated on oxide films may act as a channel for hydrogen to diffuse into the oxide film interior and make this mechanism occur easier and faster. Moreover, the large β-Al_5FeSi platelets act as a barrier to the flow of feed metal causing a decrease in the permeability of the interdendritic network and leading to the presence of microporosity in the interdendritic regions as shrinkage porosity. As shown in the Pareto diagram of tensile property and Weibull modulus results (Figures 4.1 and 4.34), the interaction between these three defects further influenced tensile properties of cast aluminium alloys since they can combine together and result in the presence of more detrimental defect. Consequently, to increase casting properties, it is necessary to pay more attention to the monitoring of the melt quality, in order to minimise all three defects during the casting process, particularly double oxide film defects, which can be a cause of the presence of the other defects in the cast aluminium alloys.

CHAPTER 6

CONCLUSIONS

Based on the tensile property results obtained from the cast Al-Si-Mg alloy used in this study, the Pareto diagrams obtained from the tensile properties, the Weibull distributions of the tensile property data, the observations of the fracture surfaces, microstructural examination and the image analysis of the microstructures, the following conclusions were drawn;

1. Double oxide films defect was the most important defect found in this study since they occurred to an unpredictable extent but were almost unavoidable in the cast aluminium alloys. The doubled nature of this defect meant that it acted as a crack in the castings resulting in a reduction in tensile properties. The Pareto diagrams derived from the tensile results showed that the effects of oxide film defects on UTS and elongation properties at the levels introduced in the experiments, (i.e., using filtered and unfiltered castings), in the Al-Si-Mg alloy were 21 MPa and 0.9% respectively.

2. The effect on tensile properties produced by the oxide film defects varied depending upon their shape and size. The large old oxide film defects, which formed the major part of the area of the fracture surfaces, could decrease the UTS by 150 MPa while the young oxide film had a lesser effect, because of a smaller area. The Pareto diagrams showed that the effects on UTS and elongation produced by oxide films, when the test bars containing large old oxide film defects were taken out, decreased to 9 MPa and 0.7% respectively.

3. Oxide film defects produced the greatest effect on the reliability of the castings (reproducibility of properties) by decreasing the Weibull modulus obtained from the tensile properties. The reduction in the UTS Weibull modulus and elongation Weibull modulus produced by the oxide film defects in this study were 37 and 3 respectively.

4. The Weibull plots obtained from the castings containing the large old oxide film defects were separated by two trend-lines when classified by their cause of failures. The Weibull single defect distribution, that was thought to be the most accurate statistical tool for describing the distribution of tensile properties in aluminium alloys, therefore could not be used for the castings that contained large oxide film defects.

5. Fe-rich phase produced the most detrimental effect on tensile properties in this study compared to oxide film defects and porosity. The characteristic of the Fe-rich phase, particularly β-Al_5FeSi platelet, was its brittleness, and its role as an initiator of cracks in the castings. Increasing Fe content from 0.1 to 0.5 wt% produced a reduction in UTS and elongation of 28 MPa and 1.7 % respectively.

6. Although Fe-rich phase was the most detrimental defect on the tensile properties, its effect on the UTS Weibull modulus and elongation Weibull modulus was only 10 and 0.5. This suggested that the reliability of castings with a high Fe content was much higher than those that contained a high oxide film content.

7. Porosity defects were the least detrimental defects to tensile properties in this study. The tensile properties decreased with the presence of large gas porosity, since they acted as material discontinuities and reducing load bearing area. The Pareto diagrams showed that increasing hydrogen content from 0.1 to 0.45 ml/100g Al in this study had effects on the UTS and elongation of 20 MPa and 0.7% respectively, (similar to the effects of the oxide film defects).

8. The most important interaction between the microstructural defects found in this study was the interaction between oxide films and porosity since more than 90% of the observed pores contained oxide films in their interior. This suggested that the mechanism of porosity formation involved double oxide film defects, which acted as an existing pore in the melt. The expansion of the double oxide film defects therefore resulted in the presence of gas porosity or shrinkage porosity defects in the castings.

9. The main factors for the formation of porosity were therefore hydrogen and shrinkage. Hydrogen played an important role by diffusing into double oxide film defects and inflating them to become gas porosity, while the negative pressure in the melt introduced by shrinkage also controlled the growth of double oxide films and caused the presence of shrinkage porosity in the castings.

10. The solidification time influenced the porosity formation in aluminium alloy castings by allowing more time for dissolved hydrogen to inflate pores. For example, in high purity aluminium, porosity was not observed because the solidification range was narrow and the solidification time was short.

11. SEM observation of oxide films showed that they were suitable substrates for the nucleation and growth of Fe-rich phases, particularly the β-Al_5FeSi phase.

12. The β-Al_5FeSi phase that nucleated on the crumpled double oxide films could straighten them since it was monoclinic and grew in a plate-like morphology. This would cause one surface of the double oxide film defect to be separated from the other surface and appear as crack-like porosity in the casting that resulted in a decrease in tensile properties.

13. The nucleation of Fe-rich phase onto oxide films also revealed the interaction between all three defects since it enhanced the formation of porosity in the castings. It has been suggested that Fe-rich phases that nucleated on the wetted side of entrained oxide films could act as a channel for hydrogen to diffuse into the oxide film interior more easily.

14. The β-Al_5FeSi phases that nucleated and grew during solidification might also influence the flow of liquid metal during solidification. Its platelet morphology and large size could block the feeding channels between solidifying dendrites, resulting in the presence of interdendritic shrinkage porosity originating from the double oxide films.

15. The combination of three defects could further influence the mechanical properties of cast aluminium alloys by decreasing both tensile properties and the reproducibility of properties. The Pareto diagrams showed that an interaction between Fe-rich phase, porosity and oxide film defects produced an effect on UTS and elongation of about 5 MPa and 0.5% respectively. The reduction in the UTS Weibull modulus and elongation Weibull modulus produced by their interaction in this study were 8 and 0.6 respectively.

CHAPTER 7

FUTURE WORKS

Although some progress has been made towards understanding the effects of oxide film, Fe-rich phase, porosity, and their interactions on tensile properties of cast Al-Si-Mg alloys, it is necessary to continue research in the following areas;

1. Although the oxide film defect is the most important defect in the casting, the lack of reliable and accurate techniques to measure and quantify oxide films in cast aluminium alloys has hindered understanding of how the defects may be removed. The development of measurement techniques for oxide films will be a benefit to foundries.

2. A Weibull single defect distribution may not be used for castings that contain double oxide film defects, particularly a large old double oxide films. Further research is required to examine other statistical models to obtain the most accurate tool for describing the distribution of tensile properties in aluminium alloys.

3. It seems that the growth of double oxide films was the most favoured mechanism for porosity formation in the castings. Further experiments are needed to investigate whether porosity can be observed in cast aluminium alloys that have no oxide film.

4. In this study, some pores that apparently did not contain oxide films were observed. This suggested that they might be formed by another mechanism or nucleated in some other way. It is necessary to study whether the nucleation of pore on a rough surface, or in conical cavities of an inclusion is possible.

5. It has been suggested that an amorphous film is impermeable or less permeable to hydrogen. It therefore is important to confirm whether the morphology of oxide film, for example, an amorphous film, a crystalline film or spinel, influences the formation of porosity involving the inflating of double oxide film defects by hydrogen.

6. It is important to confirm whether other Fe-rich phases such as π-$Al_8FeMg_3Si_6$, or other particles, can also nucleate on oxide films and whether they influence the formation of porosity in the casting.

7. Other inclusions in cast Al-Si-Mg alloys might also play a direct or indirect role in the formation of porosity. Further work is required to understand the effect on porosity formation of other particles such as magnesium oxide, silicon oxide, and titanium diboride.

REFERENCES

Agema, K. S., Fray, D. J., “Preliminary Investigation on the Deformation Behaviour of an Oxide Scale on Molten Aluminium”, Department of Material Science and Metallurgy, University of Cambridge, 1989.

Allen, C. M., O’Reilly, K. A. Q., Cantor, B., Evans, P. V., “Intermetallic Phase Selection in 1xxx Al Alloys”, Progress in Materials Science, 1998,43, 89-170.

Anson, J. P., Gruzleski, J. E., “The Quantitative Discrimination between Shrinkage and Gas Microporosity in Cast Aluminium Alloys using Spatial Data Analysis”, Materials Characterization, 1999, 43, 319-335.

Apelian D., Sigworth, G. K., Whaler, K. R., “Assestment of Grain Refinement and Modification of Al-Si Foundry Alloys by Thermal Analysis”, AFS Transactions, 1998, 108, 297-307.

Archer, R. S., Kemp, L. W., “Aluminium-Silicon-Magnesium Casting Alloys”, AIME Transactions, 1931 edited by Ravi et al., Metallurgical and Materials Transactions A, 2002, 391-400.

Armstrong, G. L., “Alloy Selections for Automotive Aluminium Castings”, SAE, 1978 edited by Villeneuve et al. (AFS Transactions), 2001, 287-300.

Atwood, R. C., Sridhar, S., Zhang, W., Lee, P. D., “Diffusion-Controlled growth of Hydrogen Pores in Aluminium-Silicon Casting: In situ Observation and Modelling”, Acta Materialia, 2000, 48, 405-417.

Atwood, R. C., Lee. P. D., “A Three-Phase Model of Hydrogen Pore Formation during the Equiaxed Dendritic Solidication of Aluminium-Silicon Alloys”, Metallurgical and Materials Transactions B, 2002, 33B, 209-221.

Atwood, R. C., Lee, P. D., “Simulation of the Three-Dimensional Morphology of Solidification Porosity in an Aluminium-Silicon Alloy”, Acta Materialia, 2003, 51, 5447-5466.

Backerud, L., Chai, G., Tamminen, J., "Solidification Characteristics of Aluminium Alloys", AFS/Skanaluminium, Stockholm, 1990, 71-84 and 127-150.

Blander, M., Katz, J. L., "Bubble Nucleation in Liquids", AIChE Journal, 1975, 21, 833-848.

Brandes, E. A., Brook, G. B., "Smithells Metals Reference Book", 7th Edition, Butterworth & Co. Ltd., Oxford, 1992.

BSI, Tensile testing of metallic materials, Method of test at ambient temperature (BS EN 10002-1: 2001), British Standards Institution, London, 2001.

Burry, K. V., "Statistical Models inApplied Science", John Wiley & Sons, 1975, 367-404.

Caceres, C. H., "On the effect of Macroporosity on the tensile Properties of the Al-7%Si-0.4%Mg Casting Alloy", Scripta Metallurgical et Materialia, 1995, 32, 1851-1856.

Caceres, C. H., Selling, B. I., "Casting Defects and the Tensile Properties of an Al-Si-Mg Alloy", Materials Science and Engineering A, 1996, 220, 109-116.

Caceres, C. H., Davidson, C. J., Griffiths, J. R., Wang, Q. C., "The Effect of Mg on the Microstructure and Mechanical Behavior of Al-Si-Mg Casting Alloys", Metallurgical and Materials Transactions A, 1999, 30A, 2611-2617.

Campbell, J., "Invisible Macrodefects in Castings", Journal De Physique IV, 1993, 3, 861-872.

Campbell, J., "Castings", Butterworth-Heinemann, Oxford, 2000.

Campbell, J., "Castings", 2nd Edition, Elsevier Ltd., Oxford, 2003.

Campbell, J. "Castings Practice: The 10 Rules of Castings", Elsevier Ltd., Oxford, 2004.

Cao, X., "Heat Treatment of Liquid Metal (Precipitation and Sedimentation Processing of Liquid Al-11.5Si-0.4Mg Alloy)", PhD Thesis, University of Birmingham, 2001.

Cao, X., Campbell, J., "Effect of Precipitation of Primary Intermetallic Compounds on Tensile Properties of Cast Al-11.5Si-0.4Mg Alloy", AFS Transactions, 2000, 108, 391-400.

Cao, X., Campbell, J., “The Solidification Characteristics of Fe-Rich Intermetallics in Al-11.5 Si-0.4 Mg Cast Alloys”, Metallurgical and Materials Transactions A, 2004, 35A, 1425-1435.

Cao, X., Campbell, J., “The Nucleation of Fe-Rich Phases on Oxide films in Al-11.5Si-0.4Mg Cast Alloys”, Metallurgical and Materials Transactions A, 2003, 34A, 1409-1420.

Chen, X. G., Engler, S., “Formation of Gas Porosity in Aluminium Alloys”, AFS Transactions, 1994, 102, 673-682.

Chiesa, F., Regimbal, P., “Distinguishing Microporosity from Macroshrinkage when Modelling Solidificaiton of A356 Castings”, AFS Transactions, 2001, 109, 347-357.

Couture, A., “Iron in Aluminium Casting Alloys- A Literature survey”, AFS International Cast Metals Journal, 1981, 6, 9-17.

Crepeau, P. N., “Effect of Iron in Al-Si Casting Alloys: A Critical Review”, AFS Transactions, 1995, 103, 361-366.

Dai, X., Yang, X., Campbell, J., Wood, J., “Effect of Runner System Design on the Mechanical Strength of Al-7Si-Mg Alloy Casting”, Materials Science and Engineering A, 2003, 354, 315-325.

Dash, M., Makhlouf, M., “Effect of Key Alloying Elements on the Feeding Characteristics of Aluminium-Silicon Casting Alloys”, Journal of Light Metals, 2001, 1, 251-265.

Davis, J. R., “Molten Aluminium Processing and Casting”, ASM Speciality Handbook, 1993, 199-230.

Dignam, M. J., “Oxide Films on Aluminium, I. Ionic Construction and Structure”, Journal of the Electrochemical Society, 1962, 109, 184-192.

Dignam, M. J., “Oxide Films on Aluminium, II. Kinetics of formation in Oxygen”, Journal of the Electrochemical Society, 1962, 109, 192-198.

Dinnis, C. M., Otte, M. O., Dahle, A. K., Taylor, J. A., “The Influence of strontium on Porosity Formation in Al-Si Alloys”, Metallurgical and Materials Transactions A, 2004, 35A, 3531-3541.

Divandari, M., Campbell, J., “Mechanisms of Bubble Trail Formation in Castings”, AFS Transactions, 2001, 109, 433-442.

Divandari, M., Campbell, J., “Bubble Damage in a Zn-Al Alloy Pressure Die Casting”, AFS Transactions, 2003, 111, 107-114.

Doty, H. W., Valtierra, S., Samuel, F. H., Samuel, A. M., “Effect of Superheat, Cooling Rate and Impurities on the Formation of Iron Intermetallics in Al-Si Die Casting Alloys”, AFS Congress paper, 2000.

Drouzy, M., Jacob, S., Richard, M., AFS International Cast Metals Research Journal, 1980, 43-50.

Eady, J. A., Smith, D. M., “The Effect of Porosity on Tensile Properties of Aluminium Alloy Casting”, Materials Forum, 1986, 9, 217-222.

Eckert Jr., C. E., “The Origin and Identification of Inclusions in Foundry Alloys”, Proceeding of 3rd International Conference on Molten Aluminium Processing, AFS, Florida, 1992.

Eichenauer, W., Markopoulos, J. Z., “Messung des Diffusionskoeffizienten von Wasserstoff in flussigem Aluminium”, Metallkde, 1974, edited by Cao, X., “Heat Treatment of Liquid Metal”, University of Birmingham, 2001.

Eustathopoulos, N., Coudurier, L., “Mouillabilite et Adhesion Thermodynamique dans le System Al-Al_2O_3: Influence d’un Recouvrement par TiB_2 ou TiN”, Amm. Chim. Fr, 1985, 10, 1-6.

Fisher, J. C., “The Fracture of liquids”, Apply Physics, 1948, 19, 1062-1066.

Fox, S., Campbell, J., “Visualisation of Oxide Film Defects during Solidification of Aluminium Alloys”, Scripta Meterialia, 2000, 43, 881-886.

Fuoco, R., Correa, E. R., Escudero, L. S., “Characterization of Some Types of Oxide Inclusions in Aluminium Alloy Castings”, AFS Transactions, 1999, 107, 287-294.

Godlewski, L. A., Zindel, J. W., “Capability Study of a Filtration Process to Predict Aluminum Melt Quality”, AFS Transactions, 2001, 109, 555-566.

Grand, L., Fonderie, 1964 edited by Li et al., Materials Science and Engineering A, 2004, 96-110.

Granger, D. A., Sawtell, R. R., Kersker, M. M., “Effect of Beryllium on the Properties of A357.0 Castings” AFS Transactions, 1984, 92, 579-586.

Green, N. R., Campbell, J., “Statistical Distribution of Fracture Strength of Cast Al-7Si-Mg Alloy”, Materials Science and Engineering A, 1993, A137, 261-266.

Green, N. R., Campbell, J., “Influence of Oxide film Filling Defects of Al-7Si-Mg alloy Castings”, AFS Transactions, 1994, 102, 341-347.

Griffin, J. A, Church, J., Weiss, D., “Fatigue, Tensile, and NDE Relationships in Cast A206-T4 Aluminium”, AFS Transactions, 2003, 111, 289-301.

Guttman, I., Wilks, S. S., Hunter, J. S., “Introductory Engineering Statistics”, John Willey&Sons, Inc.,New York, 1982, 498-500.

Haginoya, I., Fukusako, T., “Oxidation of Molten Al-Mg Alloys”, Transactions of the Japan Institute of Metals, 1983, 24, 613-619.

Halvaee, A., Campbell, J., “Critical Mold Entry Velocity for Aluminium Bronze Castings”, AFS Transactions, 1997, 105, 35-46.

Han, Q., Viswanathan, S., “Hydrogen Evolution during Directional Solidification and Its Effect on Porosity Formation in Aluminium Alloys”, Metallurgical and Materials Transactions A, 2002, 33A, 2067-2072.

Herrera, A., Kondic, V., Processing International Conference on Solidification and Cast Metals, The Metals Society, 1977 edited by Caceres, C. H., Scripta Metallurgica et Meteriallia, 1995, 32, 1851-1856.

Horng, J. H., Jiang, D. S., Lui, T. S., Chen, L. H., International Journal of Cast Metal Research, 2000 edited by Yi et al., Materials Science and Engineering A, 386, 396-407.

Impey, S. A. Stephenson, D. J., Nicholls, J. R., “Mechanism of Scale Growth on Liquid Aluminium”, Materials Science and Technology, 1988, 4, 1126-1132.

Impey, S. A. Stephenson, D. J., Nicholls, J. R., “A Study of the Effect of Magnesium Additions on the Oxide Growth Morphologies on Liquid Aluminium Alloys”, Proceedings of the First International Conference, the University of Cambridge, 1991.

Jeurgens, L. P. H., Sloof, W. G., Tichelaar, F. D., Mittemeijer, E. J., "Structure and Morphology of Aluminium-Oxide Films Formed by Thermal Oxidation of Aluminium", Thin Solid Films, 2002, 418, 89-101.

Jones, S. F., Evans, G. M., Galvin, K. P., "Bubble Nucleation from Gas Cavities - a Review", Advance Colloid Interface Science, 1999, 80, 27-50.

Kato, E., "Pore Nucleation in Solidifying High-Purity Copper", Metallurgical and Materials Transactions A, 1999, 30A, 2449-2453.

Kaye, A., Street, A., "Die Casting Metallurgy", Butterworths & Co Ltd., 1982, 71-79.

Khalili, A., Kromp, K., "Statistical Properties of Weibull Estimators", Journal of Materials Science, 1991, 26, 6741-6752.

Laslaz, G., Laty, P., "Gas Porosity and Metal Cleanliness in Aluminium Casting Alloys", AFS Casting Congress, 1991, edited by Lee, P. D., PhD Thesis, University of Oxford, 1994.

Latimer, K. G., Read, P. J., British Foundryman, 1976, 69, 44-52 edited by Campbell, J. "Castings Practice: The 10 Rules of Castings", Elsevier Ltd., Oxford, 2004.

Lawn, B., "Fracture of Brittle Solids", 2nd Edition, Cambridge University, 1993.

Lee, P. D., Hunt, J. D., "Measuring the Nucleation of Hydrogen Porosity during the Solidification of Aluminium-Copper Alloys", Scripta Materialia, 1997, 36, 399-404.

Lee, P. D., Chrirazi, A., See, D., "Modelling Microporosity in Aluminium-Silicon Alloys: a review", Journal of Light Metals, 2001, 1, 15-30.

Leoni, M., Fommei, F., "Causes of Hard Spots in Pressure Diecastings and Technological Remedies", Alumino, 1976, Vol 5, 246-252.

Li, Z., Samuel, A. M., Samuel, F. H., Ravindran, C., Valtierra, S., Doty, H. W., "Parameters Controlling the Performance of AA319-Type Alloys Part I. Tensile Properties", Materials Science and Engineering A, 2004, 367, 96-110.

Liu, L., Kang, S. B., Kim, H. W., "The Complex microstructures in an As-Cast Al-Mg-Si Alloy", Materials Letters, 1999, 41, 267-272.

Liu, L., Samuel, A. M., Samuel, F. H., Doty, H. W., Valtierra, S., "Influence of oxides on Porosity Formation in Sr-Treated Al-Si Casting Alloys", Journal of Materials Science, 2003, 38, 1255-1267.

Makarov, S., Apelian, D., Ludwig, R., "Inclusion Removal and Detection in Molten Aluminium: Mechanical, Electromagnetic and Acoustic Techniques", AFS Transactions, 1999, 107, 727-735.

Mi, J., Harding, R. A., Wickins, M., Campbell, J., "Entrained Oxide Films in TiAl Castings", Intermetallics, 2003, 11, 377-385.

Mi, J., Harding, R. A., Campbell, J., "Effect of the Entrained Surface film on the Reliability of Castings", Metallurgical and Materials Transactions A, 2004, 35A, 2893-2902.

Mondofo, L. F., "Aluminium Alloys: Structure and Properties", Butterworth, London, 1976.

Mohanty, P. S., Samuel, F. H., Gruzleski, J. E., "Experimental Study on Pore Nucleation by Inclusions in Aluminium Casting", AFS Transactions, 1995, 103, 555-564.

Montgomery, D. C., "Design and Analysis of Experiments", John Willey&Sons, Inc., New York, 2000, 340-341.

Murali, S., Raman, K. S., Murthy, K. S. S., "The Formation of β–$FeSiAl_5$ and Be-Fe phases in Al-7Si-0.3Mg Alloy Containing Be", Materials Science and Engineering A, 1995, 190, 165-172.

Nagel, G. E., Mouret, J. P., Dubruelh, J., "A357 Type Alloy with Improved Properties" , AFS Transactions, 1983, 91, 157-160.

Narayanan, L. A., Samuel, F. H., Gruzleski, J. E., "Crystallization Behavior of Iron-Containing Intermetallic Compounds in 319 Aluminium Alloy", Metallurgical and Materials Transactions A, 1994, 25A, 1761-1773.

Nyahumwa, C., Green, N. R., Campbell, J., "Effect of Mold-Filling Turbulence on Fatigue Properties of Cast Aluminium Alloys", AFS Transactions, 1998, 106, 215-223.

Otte, M. O., McDonald, S. D., Taylor, J. A., StJohn, D. H., Schneider, W., “Controlling Porosity-Related Casting Rejects: Understanding the Role of Iron in Al-Si Alloys”, AFS Transactions, 1999, 107, 471-478.

Pehlke, R. D., “Foundry Processes-their Chemistry and Physics”, General Motors Research Laboratories, 1987, edited by Samuel and Samuel, AFS Transactions, 1992, 657-666.

Piwonka, T. S., Flemings, M. C., “Pore Formation in Solidification”, Transactions Metallurgical Society of AIME, 1966, 236, 1157-1165.

Ransley, C. E., Neufeld, H., “The Solubility of Hydrogen in Liquid and Solid Aluminium”, Journal of the Institute of Metals, 1948, 74, 599-620.

Ravi, M., Pillai, U. T. S., Pai, B. C., Damodaran, A. D., Dwarakadasa, E. S., “The Effect of Mishmetal Addition on the Structure and Mechanical Properties of a Cast Al-7Si-0.3Mg Alloy Containing Excess Iron (up to 0.6 Pct)”, Metallurgical and Materials Transactions A, 2002, 32A, 391-400.

Rooy, E. L., “Mechanisms of Porosity Formation in Aluminium”, Modern Casting, 1992, September, 34-36.

Roy, N., Samuel, A. M., Samuel, F. H., “Porosity Formation in Al-9 wt pct Si-3 wt pct Cu Alloy Systems: Metallographic Observations”, Metallurgical and Materials Transactions A, 1996, 27A, 415-429.

Runyoro, J., Campbell, J., “Critical Gate Velocities for Film-forming Casting Alloys: A Basis for Process Specification”, AFS Transactions, 1992, 100, 225-234.

Sabau, A. S., Viswanathan, S., “Microporosity Prediction in Aluminium Alloy Casting”, Metallurgical and Materials Transactions B, 2002, 33B, 243-255.

Samuel, A. M., Samuel, F. H., “Porosity Factor in Quality Aluminium Castings”, AFS Transactions, 1992, 100, 657-666.

Samuel, A. M., Samuel, F. H., Doty, H. W., Valtierra, S., “Effect of Superheat, Cooling Rate and Impurities on the Formation of Iron Intermetallics in Al-Si Die Casting Alloys”, AFS Transactions, 2001, 109, 679-696.

Samuel, F. H., Ouellet, P., Samuel, A. M., Doty, H. W., "Effect of Mg and Sr Additions on the Formation of Intermetallics in Al – 6 Wt Pct Si – 3.5 Wt Pct Cu – (0.45) to (0.8) Wt Pct Fe 319-Type Alloys", Metallurgical and Materials Trancsaction A, 1998, 29A, 2871-2884.

Serratos, M., Poirier, D. R., Lyman, W. D., "Effect of Stirring on Oxide Skins and Porosity in A356 Aluminium Alloy", AFS Transactions, 2000, 108, 719-724.

Shabestari, S. G., Gruzleski, J. E., "Modification of Iron Intermetallic by Strontium in 413 Aluminium Alloys", AFS Transactions, 1995, 103, 285-293.

Shabestari, S. G., Mahmudi, M., Emamy, M., Campbell, J., "Effect of Mn and Sr on Intermetallics in Fe-rich Eutectic Al-Si Alloy", International Journal of Cast Metals Research, 2002, 15, 17-24.

Shahani, H., "Effect of Hydrogen on the Shrinkage Porosity of Aluminium Copper and Aluminium Silicon Alloys", Scandinavian Journal of Metallurgy, 1985, 14, 306-312.

Shivkumar, S., Apelian, D., Zou, J., "Modelling of Microstructure Evolution and Micro-porosity Formation in Cast Aluminium Alloys", AFS Transactions, 1990, 98, 897-904.

Sigworth, G. K., Shivkumar, S., Apelian, D., "The Influence of Molten Metal Processing on Mechanical Properties of Cast Al-Si-Mg Alloys", AFS Transactions, 1989, 97, 811-824.

Silva, M. P., Talbot, D. E. J, "Oxidation of Liquid Aluminium-Magnesium alloys", Light Metals, 1988 edit by P.G. Campbell, The Minerals, Metals and Materials Society, 1998, 1035-1040.

Simensen, C., Rolfsen, T. L., "Production of π-AlMgSiFe crystals", Z. Metallkd., 1997, 88, 142-146.

Sinfield, R., Harris, D. A., Journal of Australian Institute of Metals, 1975 edit by Sigworth et al., AFS Transactions, 1983, 811-824.

Singh, D. P. K., Mitchell, D. J., "Analysis of Metal Quality in a Low Pressure Permanent Mold Foundry", AFS Transactions, 2001, 109, 333-346.

Skjerpe, P., "Intermetallic Phases Formed during DC-Casting of an Al-0.25 wt pct Fe-0.13 wt pct Si Alloy", Metallurgical Transactions A, 1987, 18A, 189-200.

Sleppy, W. C., “Oxidation of Molten High-Purity Aluminium in Dry Oxygen”, Journal of the Electrochemical Society, 1961, 1097-1102.

Surappa, M. K., Blank, E, Jaquet, J. C., “Effect of Macro-porosity on the Strength and Ductility of Cast Al-7Si-0.3Mg Alloy”, Scripta Metallurgica et Meteriallia, 1986, 20, 1281-1286.

Talbot, D. E. J., “Effect of Hydrogen in Aluminium, Magnesium, Copper, and Their Alloys”, International Metallurgical Reviews, 1975, 20, 166-184.

Taylor, J. A., Schaffer, G. B., StJohn, D. H., “The Role of Iron in the Formation of Porosity in Al-Si-Cu-Based Casting Alloys: Part I Initial Experimental Observations”, Metallurgical and Materials Transactions A, 1999, 30A, 1643-1650.

Taylor, J. A., Schaffer, G. B., StJohn, D. H., “The Role of Iron in the Formation of Porosity in Al-Si-Cu-Based Casting Alloys: Part III. A Microstructural Model”, Metallurgical and Materials Transactions A, 1999, 30A, 1657-1661.

Taylor, J. A., Schaffer, G. B., StJohn, D. H., “The Effect of Iron Content on the Formation of Porosity and Shrinkage Defects in Al-Si-Cu-Mg Alloy Castings”, Proceeding of the 4th Decennial International Conference on Solidification Processing, 1997, 238-242.

Thiele, W., Die Oxydation von Aluminium- und Aluminiumlegierungs-Schmelzen, 1962, 38, 708-786.

Tian, C., Law, J., Touw, V. D., Murray, M., Yao, J. Y., Graham, D., StJohn, D., “Effect of Melt Cleanliness on the Formation of Porosity Defects in Automotive Aluminium High Pressure Die Castings”, Journal of Materials Processing Technology, 2002, 122, 82-93.

Traenkner, F. O., Modern Casting, 1982, 36-37.

Turmezey, T., Stefaniay, V., Griger, V., “AlFeSi Phases in Aluminium”, Key Engineering Materials, 1990, 44&45, 57-68.

Tuner, A. N., Bryant, A. N., Journal of the Institute of Metals, 1967, 95, p.355.

Villeneuve, C., Samuel, A. M., Samuel, F. H., Doty, H. W., Valtierra, S., "Role of Trace Elements in Enhancing the Performance of 319 Aluminium Foundry Alloys", AFS Transactions, 2001, 109, 287-300.

Wang, Q. G., Apelian, D., Lados, D. A., "Fatigue Behavior of A356-T6 Aluminium Cast alloys. Part I. Effect of Casting Defects", Journal of Light Metals, 2001, 1, 73-84.

Weibull, W., "A Statistical Distribution Function of Wide Applicability", Journal of Applied Mechanics, 1951, 18, 293-297.

Weigel, J., Fromm, E., "Determination of Hydrogen Absorption and Desorption Processes in Aluminium Melts by Continuous Hydrogen Activity Measurements", Metallurgical and Materials Transactions, 1990, 21B, 855-860.

Werfers K., Misra, C., "Oxides and Hydroxides of Aluminium", Alcoa Technical paper,1987 edited by Cao, X., PhD Thesis, University of Birmingham, 2001.

Wilson, S. J., Connell, J. D. C., "A Kinetic Study of the System β-AlOOH/Al_2O_3", Journal of Solid State Chemistry, 1980, 34, 315-322.

Wilt, P. M., "Nucleation Rates and Bubble Stability in Water-Carbon Dioxide Solutions", Journal of Colloid and Interface Science, 1986, 112, 530-538.

Xu, R. B., McLellan, R. B., "The solubility of Hydrogen in Fe_3Al-Intermetallics", Journal of Physical and Chemical Solids, 1997, 58, 2127-2129.

Zadeh, A. H., Campbell, J., "Metal Flow Through a Filter System", AFS Transactions, 2002, 110, 19-35.

Zalensas, D. L., "Aluminium Casting Technology", 2nd Edition, American Foundrymen's Society, Inc., Illinois, 1993.